

Abstract of “*In-vivo* Microstructural and Anatomical Analysis of Brain White Matter from Diffusion MRI” by Wenjin Zhou, Ph.D., Brown University, May 2013.

This dissertation presents new computational approaches toward the virtual histology of white-matter microstructures and new visualization and interaction techniques for identifying and segmenting white-matter anatomy. Together, our new techniques, which are based on diffusion magnetic resonance imaging (diffusion MRI), enhance the microstructural and anatomical analysis of brain white matter to localize neurological changes resulting from disease and degeneration in two ways. First, clinically feasible acquisition is sufficient for accurate reconstruction of quantitative measurements of microstructural properties in brain tissue of unknown orientation. Second, qualitative visualization using 3D interaction combined with anatomical landmarks can enhance user performance in isolating tracts for pathological analysis.

The first part of the dissertation presents new computational approaches toward the virtual histology of brain tissue that reveal quantitative local measures of their microstructure and attempt to provide reliable and sensitive biomarkers for neurological changes. We develop analytical models of water diffusion and incorporate them into a computational algorithm in order to extract the underlying microstructural properties that are otherwise unattainable *in vivo*. We go beyond current experimental limitations, which require high gradients (not achievable in clinical scanners) and known tissue orientation, by using double-pulsed field gradient (double-PFG) diffusion MRI. We demonstrate that clinically feasible acquisition is sufficient to reconstruct these microstructural properties accurately in brain tissue of unknown orientation. The feasibility and reliability of these computational approaches were first quantitatively validated using simulations, which let us go beyond previous work to provide a complete study that aggregates a set of characteristics not previously combined. To validate our methods further, we then apply our computational approaches to live human subjects using clinical 3T MRI scanners for microstructure quantification and cross-subject comparisons. The results demonstrate the sensitivity of our approach to human microstructural properties, and also verify microstructural variations known from histology along the *corpus callosum* across different subjects.

The second part of the dissertation presents new qualitative visualization and interaction techniques that help neuroscientists isolate neural tracts of interest (TOI) for quantitative local pathological analysis. First, we develop two new visualization techniques and demonstrate their benefits in disentangling complex neural tracts and in helping neuroscientists

identify the underlying neuroanatomy and its connectivity. Second, we study the design principles related to the TOI selection techniques to analyze their utility, usability, accuracy and reliability. We develop taxonomy and design guidelines for these TOI selection tasks as a framework for categorizing the design space of the techniques. Using these design guidelines, we implement two selection techniques to enhance user performance in TOI selection tasks that use two or more of the following features: (1) anatomical landmarks matching experts' training, (2) free-form lasso drawing for flexible selection, (3) a 3D stereo virtual reality environment to avoid visual flattening of brain structures, (4) haptics-assisted 3D lasso drawing for direct 3D interaction, and (5) a higher-input-bandwidth device to reduce navigation time.

In-vivo Microstructural and Anatomical
Analysis of Brain White Matter from
Diffusion MRI

by

Wenjin Zhou

B. S., University of Nebraska-Lincoln, 2005

Sc. M. Brown University, 2009

A dissertation submitted in partial fulfillment of the
requirements for the Degree of Doctor of Philosophy
in the Department of Computer Science at Brown University

Providence, Rhode Island

May 2013

© Copyright 2013 by Wenjin Zhou

This dissertation by Wenjin Zhou is accepted in its present form by
the Department of Computer Science as satisfying the dissertation requirement
for the degree of Doctor of Philosophy.

Date _____
_____ David H. Laidlaw, Director

Recommended to the Graduate Council

Date _____
_____ Odest C. Jenkins, Reader

Date _____
_____ Benjamin J. Raphael, Reader

Approved by the Graduate Council

Date _____
_____ Peter M. Weber
Dean of the Graduate School

Abbreviations

CC	Corpus Callosum
CNS	Central Nervous System
WM	White Matter
GM	Gray Matter
AD	Alzheimer's Disease
MS	Multiple Sclerosis
EM	Electron Microscopy
TEM	Transmission Electron Microscopy
SEM	Scanning Electron Microscopy
HIV	Human Immunodeficiency Virus
TOI	Tracts of Interest
ROI	Region of Interest
VOI	Volume of Interest
d-MRI	Diffusion Magnetic Resonance Imaging
DWI	Diffusion Weighted Imaging
DTI	Diffusion Tensor Imaging
NMR	Nuclear Magnetic Resonance
s-PFG	Single Pulsed Field Gradient
d-PFG	Double Pulsed Field Gradient
EPI	Echo Planar Imaging
FA	Fraction Anisotropy
MD	Mean Diffusivity
SNR	Signal-to-Noise Ratio
T1	Longitudinal Relaxation Time
T2	Transversal Relaxation Time
TE	Echo Time
TR	Repetition Time
MCMC	Markov Chain Monte Carlo
LM	Levenberg-Marquardt

List of Symbols

Experiment Parameters

G	Diffusion gradient	$[G] = \text{T/m}$
Δ	Diffusion time	$[\Delta] = \text{s}$
δ	Pulse duration	$[\delta] = \text{s}$
t_m	Mixing time	$[t_m] = \text{s}$
γ	Gyromagnetic ratio	$\gamma = 2.6751 \times 10^8 \text{s}^{-1} \text{T}^{-1}$ for ^1H
b	$b = \gamma^2 \delta^2 G^2 (\Delta - \delta/3)$	$[b] = \text{s/mm}^2$
q	$q = \frac{1}{2\pi} \gamma \delta \text{ G}$	$[q] = 1/\text{mm}$

Model Parameters

(α, β)	Shape and scale parameter of gamma distribution respectively	
a	Axon radius	$[a] = m, \bar{a} = \alpha\beta$
$\mathbf{u} = (1, \theta, \phi)$	Axon orientation	$[\theta]$ or $[\phi] = \text{radian}$
$f \in (0, 1)$	Volume fraction of the intra-axonal compartment	
D	Diffusivity	$[D] = \text{m}^2/\text{s}$

Acknowledgments

I would like to thank the many people who have contributed their energy and support to the work leading to this dissertation.

First of all, I owe my deepest gratitude to my advisor, David Laidlaw, who once told me that “I care about you to succeed” which deeply moved me and gave me the courage to take on any obstacle in research. He has also provided an excellent environment for my development as an interdisciplinary researcher. I will always be grateful for his support, guidance, and understanding during my Ph.D. journey at Brown. I am extremely grateful to have David as my mentor for life when he told me that “my advising doesn’t stop here” upon finishing my dissertation.

The readers of this dissertation, Chad Jenkins and Ben Raphael, for their feedback and guidance in refining the work.

Edward Walsh for helping me take on the special challenges of clinical MRI scanners and sitting by me during numerous hour-long scans.

Brown MRF for their generosity and understanding in my diffusion sequence testing on the scanner. Lynn Fanella and Erika Nixon for preparing my research participants for MRI scans.

Members of the Brown visualization lab who have been extremely helpful in discussing new research ideas and providing excellent feedbacks during my numerous SciVis lunch talks. My academic siblings Song, Liz, Dan, Danny, and Danfeng for their support and guidance during my first years of adjusting to Brown and their encouragement over time.

My collaborators outside the department, Steve Correia, David Tate, and Matt Hall, for helping me define interdisciplinary research problems and participating in my user studies as domain experts.

Trina, Shiyin, Mike, and Young for proofreading a number of my papers and listening to my practice talks. Lauren, Dawn, Kathy and Genie for helping me keep things in order for department matters. Tstaff for solving all computer problems in the department.

My very close friends in Providence (in no particular order), Radu, Doria, Aparna, Misha, Aggeliki, Justin, Hua, Jean, Carleton, Çağatay, Deqing, Joanne, Yun, and Fufu, for your friendship and encouragements during paper deadlines.

My dear old friends in Shanghai who I have known since high school, Yajune, Yunyun, Yaqin, Sun Hui, and Zhong Jin, for your long lasting friendship and care for my parents while I'm abroad.

Darren, for being a true companion and putting up with late work nights remotely with me. I could not have done this without you. Nutty and Fiona, for being my biggest emotional supporters.

Finally, and most importantly, I would like to thank my parents, for your unconditional love, support, patience, and always believing in me.

Contents

List of Tables	xii
List of Figures	xiii
1 Introduction	1
1.1 Motivation	1
1.2 Thesis Statement	4
1.3 Contributions Overview	4
1.3.1 Part I: <i>In-vivo</i> microstructural analysis of brain white matter	5
1.3.2 Part II: <i>In-vivo</i> anatomical analysis of brain white matter	5
1.4 Overview of Dissertation	6
2 Background	8
2.1 Diffusion Magnetic Resonance Imaging	8
2.1.1 Magnetic Moment	8
2.1.2 Magnetic Moment in a Magnetic Field	9
2.1.3 Principle of Nuclear Magnetic Resonance (NMR)	10
2.1.4 Magnetic field gradients	12
2.1.5 Diffusion Tensor Imaging (DTI)	12
2.2 Mathematical Background	14
2.2.1 Hilbert Space	14
2.2.2 Fourier Expansion and Fourier Transform	16
2.2.3 Partial Differential Equations	18
2.3 Neuroanatomy Background	22
2.3.1 Microstructural Components of the CNS White Matter	23
2.3.2 Neurological Changes in Diseases	27
2.3.3 Histological Methods: Microscopic Examination	28

I	Brain White Matter Microstructural Analysis	30
3	Microstructural Analysis Using Double-Pulsed Field Gradient MR	31
3.1	Introduction and Related Work	32
3.2	Imaging Protocol	34
3.3	Geometric Tissue Model	35
3.4	Analytical Diffusion Model	36
3.4.1	NMR Signal Attenuation in Double-PFG MR	36
3.4.2	Uniform Axon Radius Model	39
3.4.3	Distributed Axon Radii Model	40
3.5	Model Fitting	41
3.5.1	Bayesian Inference using Markov Chain Monte Carlo	41
3.5.2	Levenberg-Marquardt Fitting	42
3.6	Simulation-based Validation	43
3.6.1	Data Synthesis	43
3.6.2	MRI Experiment Design	44
3.6.3	Axons with Uniform Radius	44
3.6.4	Axons with Distributed Radii	45
3.6.5	Discussion	51
3.7	Healthy Human Subject Validation	55
3.7.1	Human Subjects	55
3.7.2	MRI Experiment Design	55
3.7.3	Parameter Estimates	55
3.7.4	Discussion	61
3.8	Conclusion	62
4	Water Exchange Analysis Using Single-Pulsed Field Gradient MR	64
4.1	Introduction and Related Work	64
4.2	Tissue Model	65
4.2.1	Geometric Model	65
4.2.2	Analytical Model	66
4.3	Datasets	72
4.4	Results	72
4.5	Discussion	74
4.6	Conclusion	74

Appendices	75
A Solution of the Torrey-Bloch Equation for double-PFG	76
A.1 Torrey-Bloch Equation with Boundary Condition	76
A.2 Solution of the Torrey-Bloch Equation using Green’s Function	77
B Derivation of Boundary Condition	80
C Derivation of Normalizing Constants	81
II Brain White Matter Anatomical Analysis	83
5 Brain White Matter Visualization: Spatial Relations	84
5.1 Introduction	84
5.2 Related Work	84
5.3 Visualization Approach A: Perceptual Coloring	85
5.3.1 Method	85
5.3.2 Results	85
5.3.3 Conclusion	87
5.4 Visualization Approach B: Texture Patterns	87
5.4.1 Method	88
5.4.2 Results	88
5.4.3 Conclusion	90
6 Brain White Matter Tracts-of-Interest (TOI) Selection Tool	93
6.1 Introduction	93
6.2 Related Work	93
6.3 Taxonomy and Design Guidelines of TOI Selection	94
6.3.1 Introduction	94
6.3.2 Methods for Evaluating TOI Selection Tools	95
6.3.3 Results	97
6.3.4 Conclusion	98
6.4 TOI Selection Approach A: 2D Sketching	98
6.4.1 Method	98
6.4.2 Results	101
6.4.3 Conclusion	101

6.5	TOI Selection Approach B: 3D Haptics-assisted Lasso Drawing	101
6.5.1	Method	103
6.5.2	Results	104
6.5.3	Conclusion	106
7	Conclusion	107
7.1	Summary of Primary Contributions	107
7.2	Recommendations for Future Research and Practical Applications	108
7.3	Summary	110
A	Neuroanatomy Terminology	111
	Bibliography	112

List of Tables

2.1	Axon diameter range for human pyramidal tract in medullary pyramid and the Rhesus monkey in CC.	25
3.1	Summary of estimated mean values of axon parameters from the model with uniform axon radius. Ground truth from simulation is: (a) Axon radii $a = (1, 2, 3, 4, 5) \mu m$; (b) Axon orientation; $\mathbf{u} = (1, 30^\circ, 60^\circ) = (1, \frac{\pi}{6}, \frac{\pi}{3})$; (c) Intra-axonal volume fraction $f = 0.7$; (d) Diffusivity $D = 2e^{-9} m^2/s$	45
3.2	<i>Distribution in human CC</i> : summary of estimated values of axon parameters. Ground truth from simulation is: (a) mean axon radius $\bar{a} = \alpha\beta = (0.82, 0.86, 1.08, 1.21, 0.94) \mu m$; (b) axon orientation; $\mathbf{u} = (1, 30^\circ, 60^\circ)$; (c) intra-axonal volume fraction $f = 0.7$; (d) Intra-axonal diffusivity $D_i = 1.7e^{-9} m^2/s$; data SNR = 30.	50
3.3	<i>Distribution in human brain range</i> : Summary of estimated values of axon parameters. Ground-truth values from simulation are: (a) Mean axon radius $\bar{a} = \alpha\beta = (1, 2, 3, 4, 5) \mu m$; (b) Axon orientation; $\mathbf{u} = (1, 30^\circ, 60^\circ)$; (c) Intra-axonal volume fraction $f = 0.7$; (d) Intra-axonal diffusivity $D_i = 1.7e^{-9} m^2/s$; data SNR = 30.	51

List of Figures

1.1	Traditional histological process in neuroanatomy: 1. Peel away tissue structures to reveal fibrous white-matter structure. 2. Extract anatomically meaningful white-matter structures such as the temporo-parieto-occipital pathway here. 3. Obtain electron microscopy images from slices of white-matter structure. 4. Measure microstructural properties such as axon diameter distribution directly from EM images.	2
1.2	Histology image of a multiple sclerosis (MS) spinal cord. The axon diameter distribution plot shows the large decrease in the number of axons observed in the plaque due to MS on the left, while normal white matter is on the right. Image from [62] (with edits).	3
1.3	Our computational solutions and interactive tools can replace the traditional process of histology for measuring the microstructural changes due to disease with a non-invasive virtual histology using diffusion MRI.	4
2.1	The two energy states of nucleus 1H	10
2.2	Dephase-rephase process in diffusion tensor imaging. Image from [71, 51] with edits.	13
2.3	Axon scheme. The axon is the core fiber extending out of the neuronal cell body that facilitates communication between gray matter and the rest of the body.	23
2.4	The myelin sheath around the nerve fibers (axons) renders the tracts white. In the area in white matter that lacks myelin, as in this dysmyelinated dog brain, white matter may appear semi-translucent (indicated by the arrows at upper left). Image from [51].	24
2.5	g-ratio, the ratio of the axonal diameter to that of the fiber (axon + myelin sheath). Conduction velocity is maximal when the g-ratio is around 0.6. Image from [51].	25

2.6	Five typical subregions of the rhesus monkey CC. A. The relationship among regional variation in axon composition (axon size, density, amount of unmyelinated axons) based on a microstructural-sector analysis by Lamantia et al. [60]. B. Topographic organization of projections through tracts from different cortical areas in the rhesus monkey [78] scaled to the same size as in A. Note that the organization of the CC correlates remarkably well in the two independent studies.	26
2.7	A. Electron micrograph of axons in section 2 of the corpus callosum in an adult rhesus monkey. Notice the small unmyelinated axons (red stars). B. Electron micrograph of axons in section 6 of the corpus callosum shown in A. In the center of this micrograph is an example of the very large axons encountered only in section 6, 7, and 10 of the corpus callosum. Both micrographs are $1 \times 10^{-4} \text{ mm}^2$. Image from [60].	27
2.8	1 μm thick histologic section of rat spinal cord. A. axons from vestibulospinal tract containing largest axons in this section of the spinal cord. B. axons from rubrospinal tract in the spinal cord where axon size appear to be much smaller and axons are more densely packed. (black bar= $50 \mu\text{m}$) Images from [89].	28
2.9	Histology images of a multiple sclerosis spinal cord sample. Completely demyelinated plaque with changes in axon diameter can be observed on the left, while normal white matter is on right (thick bar= 2mm , thin bar= $10 \mu\text{m}$). Image from [62]	29
3.1	(a) double-PFG acquisition sequence with two encoding intervals of gradient G_1 and G_2 . (b) Experimental setup: $\mathbf{u} = (1, \theta, \phi)$ defines the arbitrary axon orientation; G_1 is fixed on the x-axis and the angle of G_2 is varied linearly on the xy-plane; β_1 and β_2 denote the angle between \mathbf{u} and G_1, G_2 respectively.	35
3.2	Geometric tissue model: (a) 2D cross-sectional view of axons in the CC of an adult rhesus monkey from transmission electron micrograph (TEM), image reproduced from [60]. (b) 3D view of axons from scanning electron micrograph (SEM), image reproduced from [22]. (c-d) 2D and 3D schematic views of a non-abutting rectangular arrangement of cylinders representing: (c) axons with uniform radius and (d) axons with distributed radii.	37

3.3	Signal attenuation from experimental simulation data (without noise) vs. angle ψ between gradient pairs G_1 and G_2 that varied linearly by 15 degrees. We illustrate the angular dependency difference and signal separation between different axon size and distribution from two geometric models: (a) axons modeled with uniform radius $1 - 5 \mu m$ and (b) axons modeled with five gamma distributions (narrow and broad) centered at mean radius $1 - 5 \mu m$.	43
3.4	Histograms of 10,000 samples drawn from posterior distributions on (a) axon radius a ; (b-c) axon orientation (θ and ϕ); (d) intra-axonal volume fraction $f = 0.7$; and (e) diffusivity D for each of the various true a values using MCMC. Orange vertical lines show the true values in simulation: $a = (1, 2, 3, 4, 5) \mu m$, $\theta = \frac{\pi}{6} rad = 30^\circ$, $\phi = \frac{\pi}{3} rad = 60^\circ$, $f = 0.7$, $D = 2e^{-9} m^2/s$. The <i>mean</i> and <i>std</i> values of parameter estimates are shown in Table 3.1. Note that some overlapping bars may not be visible in the figure.	46
3.5	Mean axon radius from five regions of the CC: (1) Genu, (2) Anterior body, (3) Midbody, (4) Posterior body, (5) Splenium. The green line shows the ground-truth values computed from histology after a suggested shrinkage correction [2]; the orange line shows our estimated values.	47
3.6	Cross sections of the simulated axonal environment at five regions along the human CC from histology [2].	48
3.7	<i>Gamma distribution of axon radii in human CC:</i> measured at five sites along the CC from histology [2]. The green histogram shows the ground-truth distribution of axon radii with mean radius a -grd. The orange curve shows our fitting results for the estimated gamma distribution of the underlying axon radius distribution with mean radius a -est. The estimated and ground-truth axon radius distributions were highly correlated for all regions along the CC (with correlation coefficients $r > 0.96$). Table 3.2 gives more detailed values of additional estimated axon parameters.	49
3.8	Cross sections of the simulated axonal environment in the human brain range centered at $1 - 5 \mu m$. These axon distributions represent various gamma distributions (narrow and broad) and a broader spectrum of sizes in the human brain, including a narrow distribution with a large population of small-radius axons centered at $1 \mu m$ in (a) and a broader distribution of larger axon radii centered at $5 \mu m$ in (e).	52

3.9	<i>Gamma distribution of axon radii in human brain range.</i> The green histogram shows the ground-truth distribution of axon radii with mean radius a -grd. The orange curve shows our fitting results for estimated gamma distribution of the underlying axon radius distribution with mean radius a -est. The estimated and ground-truth axon radius distributions again correlated well for all five distributions and sizes (correlation coefficients $r > 0.85$). Table 3.3 gives more detailed values of additional estimated axon parameters.	53
3.10	Manually segmented CC area from double-PFG data collected from Subject 1 scan 1 using Osirix [87].	56
3.11	Estimation results in the CC from the midsagittal slice of scan 1 from human subject 1, including axon parameters: mean axon radius $\bar{a} = \alpha\beta$, volume fraction f , axon orientation $\mathbf{u} = (1, \theta, \phi)$, and intra-axonal diffusivity D_i . . .	57
3.12	Six anatomical segments along the CC used in our histology validation study: (1) genu, (2) anterior body (B1), (3) midbody (B2), (4) posterior body (B3), (5) isthmus, and (6) splenium. Image from [2] (with edits).	58
3.13	Comparison of trends in mean axon radius \bar{a} along six anatomical segments of the midsagittal slice of CC for each subject with histological measures from [2]. There are two separate datasets for each subject. We multiply the axon radius from histology by 1.5 to take into account tissue shrinkage during histology.	59
3.14	Comparison of trends in axon-radius distribution along six anatomical segments of the midsagittal slice of CC from subject 1, scan 1. Our axon-radius distributions show good agreement with histological measures [2, 11]: a narrow distribution in the genu, isthmus, and splenium; and a broader distribution in the body.	60
4.1	Modeling of water diffusion in white matter by two processes: restricted water diffusion within the cylindrical intra-axonal space and hindered water diffusion outside the cylinders in the extra-axonal space.	65

4.2	Histogram of 100 samples drawn from posterior distribution on radii $a = [1, 1.9, 3, 5, 7] \mu m$ using MCMC; orange lines indicate the true value of various radii; black lines indicate the mean value of each estimate with error bars showing standard deviation. The model was fitted to six constant-gradient diffusion-MRI experiments based on Monte-Carlo simulation with gradient strength $200 - 700 (mT/m)$. The results demonstrate the feasibility of recovering underlying axon radii using the model.	70
4.3	Histogram of 100 samples drawn from posterior distributions on volume fraction f , free diffusion coefficient D , and exchange rate τ at various radii: $a = [1, 1.9, 3, 5, 7] \mu m$ with color coding as in Figure 4.2. The orange lines indicate the true value of $f = 0.708$, $D = 2e^{-9} m^2/s$ and $\tau = 0.6 (s)$. The black lines indicate the mean value of each estimate with error bars showing standard deviation. Note that overlapping bars may not show on the figure.	73
5.1	White-matter tract processing flow chart.	86
5.2	Visualizing a normal and an HIV-positive brain dataset using perceptually uniform color space.	87
5.3	Textures: (a) horizontal, (b) vertical (c) diagonal; when applied on the tubes, in different positions, give four types of patterns(horizontal, vertical, diagonal and diamond).	88
5.4	Workflow for visualizing white-matter tract using texture pattern.	89
5.5	Four different patterns applied on corpus callosum streamtube model: (a) Diamond Pattern, (b) Diagonal Pattern (c) Vertical Pattern (d) Horizontal Pattern	91
5.6	Applying RGB coloring vs. diamond pattern on whole brain model (a) RGB coloring applied. Notice that the two singular bundles in the middle are colored in red with nearly no noticeable subgroup color distinction. (b) Diamond pattern applied. Notice that smaller subgroups can be visually grouped within the bigger singular bundle	92
6.1	Subjective user evaluation results. Top: action space, bottom two: outside factors	96
6.2	Snapshot of a user's selection for the four assigned white-matter fiber bundles in experiment 2.	99
6.3	User performance evaluation results: time and confidence	100

6.4	Our ROI selection application: sketching selection and interaction with data from the brain of a normal subject. (a) Color differences indicate differences between pathways shown with $4K$ tubes. (b) User selects an axis aligned plane corresponding to the midsagittal slice of the corpus callosum, displayed with a semi-transparent red plane. (c) Selected slice is shown as 2D image in which the user selects a freeform region (yellow curve). (d) All tracts passing through this region are displayed.	102
6.5	Users collaborating on hypotheses about white-matter connectivity using 3D lasso drawing selection interface in 3D stereo VR. (a) Fishtank VR setup. (b) 3D hand tracker. (c) Phantom force feedback device.	104
6.6	Our interface selecting the uncinatus fasciculus (UF) using the 3D lasso: the user places two lassos around the UF and singles out the structure with an AND operation. The final result is shown in purple.	105
6.7	The two logical operations “AND” and “OR”. Two lassos delineate ROIs placed on anatomic landmarks. (1) AND operation: neural tracts that go through both ROIs are selected. (2) OR operation: neural tracts that go through either one of the ROIs are selected. The neural tracts resulting from the corresponding logical operations are shown in blue.	106
7.1	The general application of this dissertation’s three main components.	109

Chapter 1

Introduction

1.1 Motivation

The human brain is the center of the human nervous system, which is a very important structure in our body. Many neurological diseases are associated with changes in brain microstructure and composition. Alzheimer's disease, for example, which causes the irreversible degeneration of the brain, is now the sixth leading killer in the United States. Approximately every 69 seconds, one person in the United States is diagnosed with Alzheimer's disease, and it now affects 5.1 million Americans. However, we still do not know the cause, nor do we have an effective cure. Our best defense at the moment is preventive care and early diagnosis. My dissertation suggests a road towards early diagnosis of neurological diseases such as Alzheimer's.

In order to diagnose the microstructural changes associated with various neurological diseases, neuroscientists have relied on histological examination of the brain tissue. Histology is an invasive and very tedious process (Figure 1.1) that usually involves cutting the brain in half, then peeling away some of the tissue structure in the front so as to reveal the fibrous structure called the white matter. To look more closely at the white-matter structure, we would need carefully to go through the process of extracting certain anatomically meaningful fibrous white-matter structures such as the temporo-parieto-occipital pathway shown in Figure 1.1(1). To go another step further, we can take a slice of the white-matter structure and obtain electron microscopy (EM) images to reveal the axons that make up the white-matter structure like bundles of cables. With these EM images, we can directly measure detailed microstructure information such as axon diameter distribution. These microstructural measurements are crucially correlated with a number of neurological diseases.

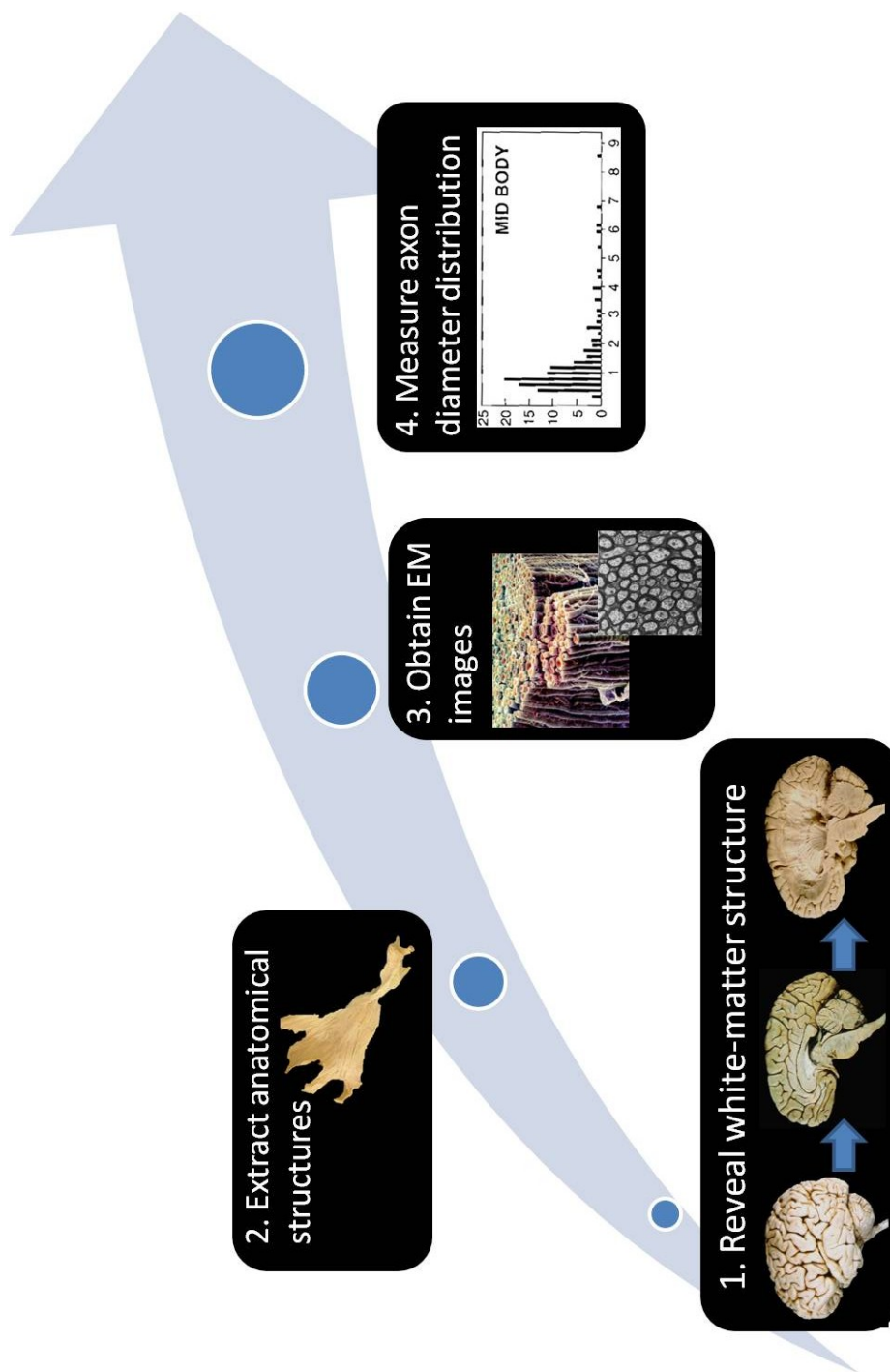


Figure 1.1: Traditional histological process in neuroanatomy: 1. Peel away tissue structures to reveal fibrous white-matter structure. 2. Extract anatomically meaningful white-matter structures such as the temporo-parieto-occipital pathway here. 3. Obtain electron microscopy images from slices of white-matter structure. 4. Measure microstructural properties such as axon diameter distribution directly from EM images.

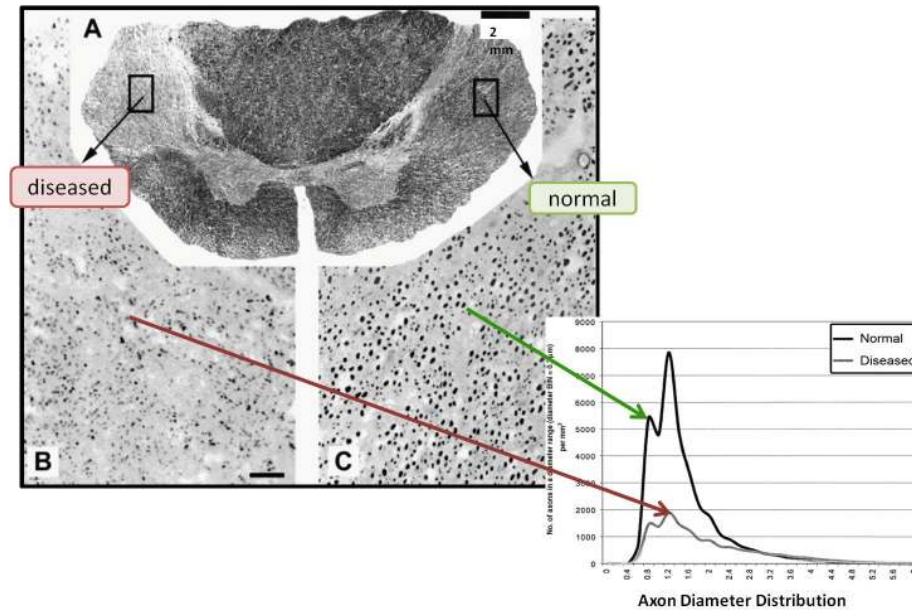


Figure 1.2: Histology image of a multiple sclerosis (MS) spinal cord. The axon diameter distribution plot shows the large decrease in the number of axons observed in the plaque due to MS on the left, while normal white matter is on the right. Image from [62] (with edits).

The questions we want to ask here are: *Where and how do diseases impact the structure of the brain?*

For example, the EM image from a multiple sclerosis (MS) patient in Figure 1.2 shows significant degeneration in axon composition between the diseased and healthy area that can be detected from an axon-diameter distribution plot. Most importantly, this sort of axon degeneration can remain undetected in a MS patient until disabling symptoms appear. Since axons rarely regenerate, early diagnosis of these changes is important for preventive care.

Although extremely useful, all the microstructural analyses described above involve the invasive histology process. There's no way we could do histology to obtain this microstructural analysis while the brain disease is progressing. The big question this dissertation tries to address is, *"How can we do this microstructural analysis noninvasively?"*

We have developed computational solutions and interactive visualization tools to replace the histology process in measuring disease-related microstructural changes with a noninvasive "virtual histology" (Figure 1.3). Our tools use diffusion MRI, to measure the Brownian motion of water molecules, which is influenced by brain-tissue geometry, and thus offer the potential to probe the brain's underlying anatomical and microstructural properties.

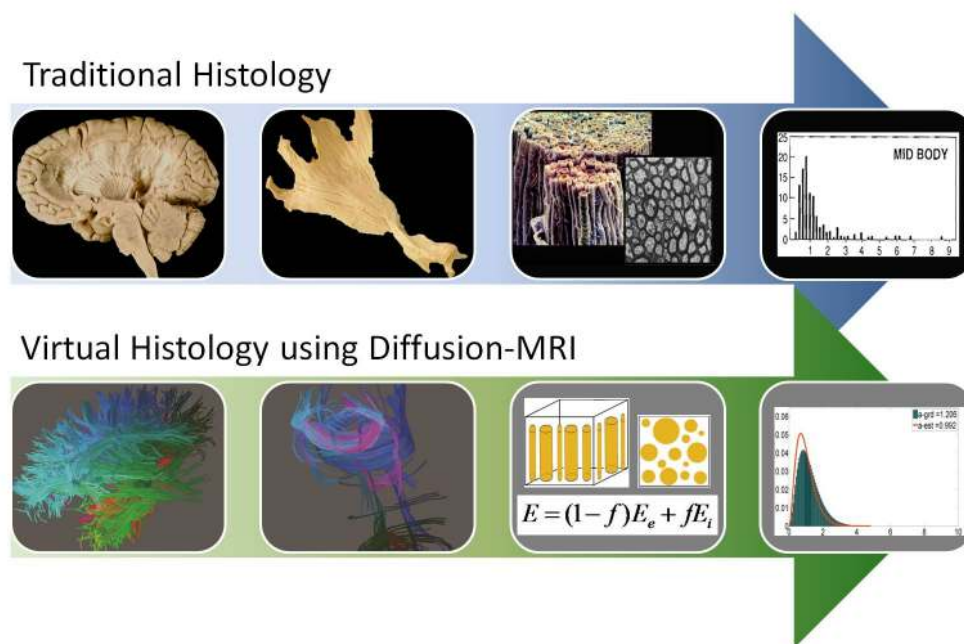


Figure 1.3: Our computational solutions and interactive tools can replace the traditional process of histology for measuring the microstructural changes due to disease with a non-invasive virtual histology using diffusion MRI.

1.2 Thesis Statement

This dissertation explores the following thesis:

Computational techniques based on diffusion MRI can enhance the microstructural and anatomical analysis of brain white matter in two ways. First, clinically feasible acquisition is sufficient for accurate reconstruction of quantitative measurements of microstructural properties in brain tissue of unknown orientation. Second, qualitative visualization using 3D interactions combined with anatomical landmarks can enhance user performance in isolating tracts for pathological analysis.

1.3 Contributions Overview

This dissertation contributes to the field of data modeling, model fitting, visualization, and human-computer interaction. The work is driven by real-world neuroscience problems and

makes significant contributions to the field of neuroscience. It contributes to the scientific understanding of white-matter anatomy and to the virtual histology of brain-tissue structure for microstructural and pathological analysis. The methods presented here have potential for significant long-term impact by providing insights into and making possible earlier detection of various neurological diseases. The contributions listed below are the result of completed and published work.

1.3.1 Part I: *In-vivo* microstructural analysis of brain white matter

Part I presents new computational approaches to the virtual histology of brain tissue and demonstrates that clinically feasible acquisition is sufficient for accurate reconstruction of quantitative measurements of microstructural properties in brain tissue of unknown orientation [112, 113, 111, 114].

The major contributions of Part I may be summarized as:

- A two-compartment analytical model of water diffusion that takes axon orientation into account and models axon-radius variation using gamma distribution
- A water-exchange model to take demyelination due to neurological diseases into account
- Computational algorithms for extracting underlying microstructural properties of white matter in the human brain range and improved sensitivity to distinguish small axon radii less than $3 \mu m$
- A complete simulation study aggregating a set of characteristics not previously combined
- A clinical study demonstrating the sensitivity of our approach to human microstructural properties, and also verifying across different subjects microstructural variations along the *corpus callosum* known from histology

1.3.2 Part II: *In-vivo* anatomical analysis of brain white matter

Part II demonstrates that qualitative visualization using 3D interaction combined with anatomical landmarks can enhance user performance in isolating tracts for pathological analysis [115, 49, 109, 110, 50, 97].

The major contributions of Part II may be summarized as:

- Visualizing white-matter spatial relations to disentangle neural-tract connectivity:
 - Visualizing white-matter pathways with perceptual coloring to provide a smooth coloring scheme that is more compatible with the uncertainty of the tractography
 - Visualizing white-matter pathways with textural patterns to show subtle differences within large structures
- White matter tracts-of-interest (TOI) selection techniques to isolate tracts for pathological analysis:
 - Taxonomy and evaluation of design features in interactive 3D TOI selection tools in DTI
 - A 2D sketching TOI-selection approach combined with anatomical landmarks for segmentation of neural pathways
 - A 3D haptics-assisted lasso-drawing TOI-selection approach in virtual reality environment to enhance user performance and confidence in isolating tracts for pathological analysis

1.4 Overview of Dissertation

Part I of this dissertation presents our new computational approaches toward the virtual histology of brain tissue that reveal quantitative local measures of their microstructure and attempt to provide reliable and sensitive biomarkers for neurological changes (Chapter 4 - Chapter 3). Here, we develop analytical models of water diffusion and incorporate them into a computational algorithm in order to extract the underlying microstructural properties that are otherwise unattainable *in vivo*. We go beyond current experimental limitations, which require high gradients (not achievable in clinical scanners) and known tissue orientation, by using double-pulsed gradient spin-echo (double-PFG) diffusion MRI. We demonstrate that clinically feasible acquisition is sufficient accurately to reconstruct these microstructural properties in brain tissue of unknown orientation. The feasibility and reliability of these computational approaches were first quantitatively validated in simulations. Simulation data lets us go beyond previous work to provide a complete study combining a set of characteristics that other work has used but never unified. For further validation of our methods, we then apply our computational approaches to human subjects using clinical 3T MRI scanners for microstructure quantification and cross-subject comparisons. Our results demonstrate our approach's sensitivity to human microstructural properties and also verify

microstructural variations known from histology across different subjects along the *corpus callosum*.

Part II of the dissertation presents new qualitative visualization and interaction techniques that help brain scientists identify and segment neural tracts of interest (TOI) for quantitative local pathological analysis. First, we develop two new visualization techniques to demonstrate their benefits in disentangling complex neural tracts and in helping neuroscientists identify the underlying neuroanatomy and its connectivity (chapter 5). Second, we study the design principles related to the TOI selection techniques to analyze their utility, usability, accuracy and reliability (Chapter 6). Tracts-of-interest (TOI) analysis is an important interaction technique on which most published clinical research studies using DTI tractography have relied [18, 73, 79]. TOI interaction tools provide the flexibility of clustering in the model and allow brain scientists to apply and verify their knowledge of the various functionalities of different neural tract bundles. We develop a taxonomy and a set of design guidelines for these TOI selection tasks as a framework for exploring and categorizing the design space of the techniques. Using these design guidelines, we implement two selection techniques to enhance user performance in TOI selection tasks. The 2D sketching selection tool gives the user a flexible interface for selecting and grouping TOI into bundles by drawing free-form lassos on 2D anatomical planes of the brain model, rather than rigid boxes as in traditional methods. This approach exploits neurologists' extensive training in identifying anatomical structures from these planes. Our 3D haptics-assisted lasso-drawing TOI-selection approach gives users more confidence in identifying neural tract bundles, and avoids the problem of visual flattening of fiber structures. The navigation time, a key challenge in TOI selection tools, is greatly reduced in the VR environment with this higher-input-bandwidth device. We discuss our conclusions in Chapter 7 with a summary of primary contributions in this dissertation and a discussion of future directions and applications.

Chapter 2

Background

This chapter gives the background for the research in the remainder of the dissertation. Section 2.1 describes the background knowledge related to diffusion imaging techniques used in this dissertation. Section 2.2 provides the mathematical background for this research. Section 2.3 describes the biological origins of diffusion imaging in neuroanatomy and microstructural changes due to neurological diseases.

2.1 Diffusion Magnetic Resonance Imaging

Diffusion magnetic resonance imaging (diffusion MRI) of the brain is based on the random Brownian motion of water molecules within brain tissue [99]. Brownian motion occurs when water molecules in the brain tissue randomly collide with one another. The result of this process, diffusion [13], is comparable to the evolution in the shape of a stain after inkdrop lands on a piece of paper [70].

Diffusion MRI is made up of individual pixels of different intensities that correspond to voxels in the brain-tissue model. The spatial resolution of diffusion MRI is on the order of $1 - 3 \text{ mm}$, and thus can reveal the anatomical properties of brain tissue in great detail. The contrast in diffusion MRI reflects biological differences among different brain tissues.

2.1.1 Magnetic Moment

Any classical charged particle with angular momentum possesses a magnetic moment $\vec{\mu}$:

$$\vec{\mu} = \frac{q}{2m} \vec{L} \quad (2.1)$$

where \vec{L} is angular momentum and q/m is charge-mass ratio.

Magnetic resonance images primarily reflect the signal from water, based on the hydrogen nucleus. The hydrogen nucleus possesses a magnetic dipole, which is also called spin. In quantum mechanics, the component of angular momentum can take on only a few discrete values. The spin angular momentum \vec{M}_I of any physical system is quantized by:

$$M_I = \sqrt{I(I+1)}\hbar \quad (2.2)$$

$$M_{I_z} = m_I\hbar \quad (2.3)$$

where $I = n/2$ is the spin quantum number (n can be any non-negative integer) and m_I is between $-I$ to I and thus has $(2I+1)$ possible values. For the nucleus ^1H , $I = \frac{1}{2}$, $M_I = \frac{\sqrt{3}}{2}\hbar$, $M_{I_z} = \{-\frac{1}{2}, \frac{1}{2}\}\hbar$.

Particles with spin can possess a magnetic moment $\vec{\mu}$ that is proportional to the spin angular momentum \vec{M}_I , just like a rotating electrically-charged body in classical electrodynamics:

$$\vec{\mu} = \gamma\vec{M}_I \quad (2.4)$$

where $\gamma = g_N \frac{e}{2m_p} = g_N \frac{\mu_N}{\hbar}$ is gyromagnetic ratio, g_N is nuclear Landé g-factor, and $\mu_N = \frac{1}{2} \frac{e}{m_p} \hbar = 5.051 \times 10^{-27} \text{J} \cdot \text{T}^{-1}$ is the Bohr magneton. For ^1H , $\gamma = 2.6751 \times 10^8 \text{s}^{-1}\text{T}^{-1}$; for ^{13}C , $\gamma = 6.7262 \times 10^8 \text{s}^{-1}\text{T}^{-1}$; and for ^{15}N , $\gamma = -2.7116 \times 10^7 \text{s}^{-1}\text{T}^{-1}$.

2.1.2 Magnetic Moment in a Magnetic Field

2.1.2.1 Larmor Precession

The magnetic moment in a magnetic field will experience a torque $\vec{\tau}$ and start to precess around the external magnetic field \vec{B} at a Larmor frequency $\vec{\omega}_L$ (this is called Larmor precession):

$$\begin{aligned} \vec{\tau} &= \vec{\mu} \times \vec{B} = \frac{d\vec{L}}{dt} \\ \Rightarrow \left(\frac{q}{2m}\vec{L}\right) \times \vec{B} &= \vec{\omega}_L \times \vec{L} \end{aligned} \quad (2.5)$$

$$\vec{\omega}_L = -\frac{q}{2m}\vec{B} \quad (2.6)$$

In general, the Larmor frequency $\vec{\omega}_L$ of the nucleus is:

$$\vec{\omega}_L = \gamma\vec{B} \quad (2.7)$$

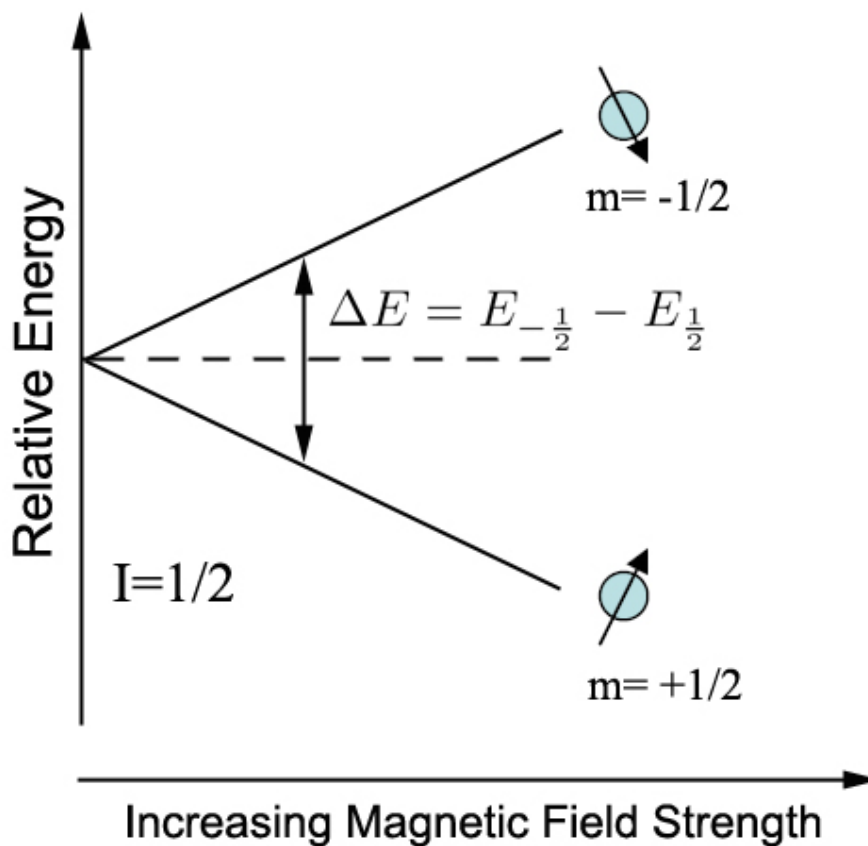


Figure 2.1: The two energy states of nucleus 1H

2.1.2.2 Spin Energy in Magnetic Field

The energy of the spin in the magnetic field is given by:

$$E = -\vec{\mu} \cdot \vec{B} = -\gamma m_I B \hbar \quad (2.8)$$

The energy level of the nucleus 1H , $I = \frac{1}{2}$, $m_I = \{\frac{1}{2}, -\frac{1}{2}\}$ has two states:

$$E = \pm \frac{1}{2} \gamma B \hbar \quad (2.9)$$

The energy difference between these two states is:

$$\Delta E = \gamma B \hbar \quad (2.10)$$

2.1.3 Principle of Nuclear Magnetic Resonance (NMR)

The principle of NMR usually involves two sequential steps:

1. The alignment of the nuclear spins in constant magnetic field \vec{B}_0 , also referred to as the first magnetic field generated in MRI.
2. The perturbation of this alignment of the nuclear spins by employing an electro-magnetic wave called RF pulse, usually oscillating at radio frequencies (RF). We call this RF pulse, which is usually applied very briefly, the second magnetic field generated by an MRI scanner.

Magnetic resonance absorption occurs only when the electro-magnetic wave has energy $E = \gamma B_0 \hbar = \omega \hbar$ matching the energy difference between the nuclear spin levels in the constant magnetic field \vec{B}_0 . This occurs when the frequency is:

$$\nu = \frac{\omega_L}{2\pi} = \frac{1}{2\pi} \frac{\Delta E}{\hbar} = \frac{1}{2\pi} \gamma B_0 \quad (2.11)$$

The two fields are usually chosen to be perpendicular to each other, since this alignment maximizes NMR signal strength. In a 3T MRI scanner, for example $B_0 = 3T$, such a configuration results in an absorption frequency of ^1H : $\nu = \frac{1}{2\pi} (2.6751 \times 10^8 \text{rads}^{-1} T^{-1} \times 3T = 127.7310 \text{MHz}$.

The RF pulses are used in MRI for two main purposes: excitation and refocusing. An MRI experiment typically starts with a $\theta = 90$ degree excitation RF pulse. The pulse frequency is applied at the Larmor frequency of the spins ($\omega_L = \gamma B_0$) to induce resonance so that the magnetization vector is tilted into the plane whose normal is along the main magnetic field. The RF pulse is applied along the X' axis of the rotating frame around \vec{B}_0 . The sequence is then followed by a refocusing of nuclei with $\theta = 180$ degree RF pulse. If the RF pulse duration δ is much smaller than spin relaxation time, the flip angle of the nuclear spin is $\theta = \omega \delta = \gamma B \delta$. We adjust the pulse duration δ to adjust for the flip angle θ . After the 90 degree excitation pulse, the excited spins immediately do three things:

1. Precess about \vec{B}_0 at Larmor frequency $\omega_L = \gamma B_0$
2. Realign themselves exponentially in the direction of \vec{B}_0 , with time constant T_1 , which is also called the *longitudinal relaxation time*.
3. The precessing part of this magnetization (i.e., the part perpendicular to the direction of \vec{B}_0) decays exponentially with a time constant T_2 , also called the *transverse relaxation time*.

2.1.4 Magnetic field gradients

The third set of magnetic fields generated by an MRI scanner is called magnetic field gradients and often referred to as G_x , G_y , and G_z . They create linear magnetic fields that change in three orthogonal directions:

$$B = B_0 + x \frac{\partial B}{\partial x} + y \frac{\partial B}{\partial y} + z \frac{\partial B}{\partial z} \quad (2.12)$$

$$= B_0 + xG_x + yG_y + zG_z \quad (2.13)$$

2.1.4.1 Slice selection: G_z

A slice selection gradient G_z is used with a selective excitation to select a region for imaging. The linear gradient G_z is applied along the z-direction so that the Larmor frequency changes linearly along the direction of the gradient. A RF pulse matching a specific Larmor frequency along the z-axis will excite only spins at that particular slice perpendicular to the applied G_z gradient. We can change the location of slice selection by changing the frequency of the RF pulse, and can adjust the slice thickness by modifying the frequency bandwidth of the RF pulse and the strength of the gradient G_z .

2.1.4.2 Image Encoding: G_x and G_y

Image encoding gradients G_x and G_y are used to encode the location of MR signals received from the object being imaged. In the excited x-y slice, image-encoding gradients G_x and G_y are applied to generate linear changes in precessional frequency. By convention, G_y is called the *phase-encoding* gradient and G_x is called the *frequency-encoding* gradient. Different pulse sequences determine the image-encoding process. The exact image-sampling process is determined by the pulse sequence designs discussed in [51], which are beyond the scope of this thesis.

2.1.5 Diffusion Tensor Imaging (DTI)

Diffusion tensor imaging is a technique in which the diffusion of water is measured in a series of different spatial directions [12]. As water undergoes diffusion, it encounters barriers that reflect underlying tissue properties and environments. The challenge in diffusion MRI is to infer these complex tissue structures from MR displacement measurements. Imagine injecting ink inside brain white matter: its distribution will elongate along axonal fibers by anisotropic diffusion. Inside the gray matter, the diffusion process is more random because

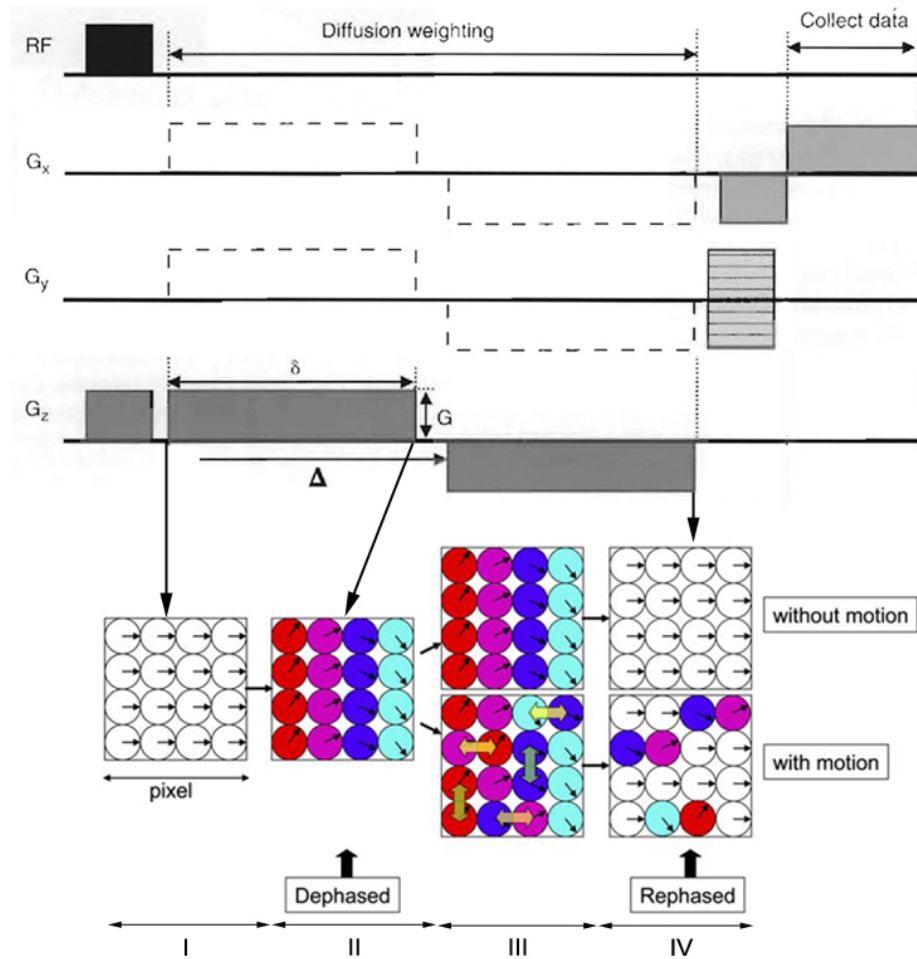


Figure 2.2: Dephase-rephase process in diffusion tensor imaging. Image from [71, 51] with edits.

of the absence of restricted fiber structures, a process called isotropic diffusion. DTI then fits diffusion ellipsoids from each pixel in the image to describe the shape and orientation of the local tissue. Thus, by using DTI, three-dimensional neural tracts representing the axonal fibers in the white matter can be reconstructed.

The diffusion-encoding gradient in DTI is a bipolar gradient typically applied after the 90° excitation pulse and before image signal sampling. Figure 2.2 illustrates the effect on the spins of applying the diffusion gradient. This diffusion gradient can be applied in any direction $G(x, y, z)$. To illustrate this point, we show diffusion weighting in only one direction, along the z-axis G_z . At time I, all spins under the homogeneous \vec{B}_0 field are in-phase. They have the same signal frequency and are in the same phase. At time II, the positive diffusion gradient is applied. Spins start to dephase and will experience different frequencies along the z-axis (protons at higher G_z experience higher frequency). At time III, when the positive gradient is turned off, all spins return to the same frequency but they are now in different phases. At time IV, we apply a 180° RF pulse in order to induce a reversed (negative) linear gradient G_z . Due to the reversed gradient strength along z-axis, protons can be rephased exactly back to their original phase, if they have not moved between the two gradient applications (between times II and IV). If the spins have moved due to diffusion during the diffusion gradient application, the second gradient (at time IV) cannot perfectly refocus the phases leading to signal loss.

2.2 Mathematical Background

This section reviews the mathematical background on which this dissertation builds.

2.2.1 Hilbert Space

Hilbert space is an extension of Euclidean space to spaces with any finite or infinite number of dimensions. A Hilbert space is an abstract vector space possessing the structure of an inner product that allows length and angle to be measured.

2.2.1.1 Abstract linear vector space

A pair of vectors x and y of a Hilbert space H satisfies the following properties:

- $\langle x|x \rangle \geq 0$, where the case of equality holds if and only if $x = 0$.
- $\langle y|x \rangle = \overline{\langle x|y \rangle}$

- $\langle cx|y \rangle = c \langle x|y \rangle$
- $\langle (x_1 + x_2)|y \rangle = \langle x_1|y \rangle + \langle x_2|y \rangle$
- $\langle x|y \rangle = 0$, if and only if x and y are orthogonal vectors

2.2.1.2 Function Space

A sequence of functions $\varphi_n = \varphi_1, \varphi_2, \dots, \varphi_n, \dots$, for example $1, \cos(x), \cos(2x), \dots, \sin(x), \sin(2x), \dots$ or e^{ikx} , forms the basis function of a Hilbert space if they define a scalar product and satisfy the following completeness, orthogonality, and normalization conditions:

$$\langle \varphi_1|\varphi_2 \rangle = \int \varphi_1^* \varphi_2 d\tau \quad (2.14)$$

$$\sum |n \rangle \langle n| = 1 \quad (2.15)$$

$$\langle \varphi_i|\varphi_j \rangle = \delta_{ij} = \begin{cases} 1 & \text{if } i = j \\ 0 & \text{if } i \neq j \end{cases} \quad (2.16)$$

If the eigenvalues are continuous in equation (2.16), we rewrite it as:

$$\langle \varphi(\vec{k})|\varphi(\vec{k}') \rangle = \delta(\vec{k} - \vec{k}') \quad (2.17)$$

where $|n \rangle = \varphi_n$, $\langle n| = \varphi_n^*$, and $\delta(\vec{k} - \vec{k}')$ is the delta function discussed in section 2.2.1.3.

In Hilbert space, we can obtain the following:

- For an eigenequation $\hat{L}\varphi_n = \lambda_n\varphi_n$, the eigenfunction of a hermitian operator is orthogonal and complete, and its eigenvalues are real numbers.
- We can define the Fourier expansion of any function Ψ on the same domain by using a basis eigenfunction φ_n :

$$\Psi = \sum c_n \varphi_n \quad (2.18)$$

$$c_n = \langle \varphi_n|\Psi \rangle = \int \varphi_n^* \Psi d\tau \quad (2.19)$$

- Any eigen-differential equation $\hat{L}\Psi = \lambda\Psi$ can be written as a matrix algebra equation by using the equation (2.15): We perform left multiply $\langle n|$ and insert equation (2.15) $|m\rangle\langle m|$ on both sides of the differential equation:

$$\hat{L}\Psi = \lambda\Psi \quad (2.20)$$

$$\sum_m \langle n|\hat{L}|m\rangle\langle m|\Psi\rangle = \sum_m \lambda \langle n|m\rangle\langle m|\Psi\rangle \quad (2.21)$$

Since we have $\langle m|\Psi\rangle = c_m$, $\langle n|m\rangle = \delta_{mn}$ and we can define a matrix $L_{nm} = \langle n|\hat{L}|m\rangle$ to derive a matrix equation:

$$\sum (L_{nm} - \lambda\delta_{nm})c_m = 0 \quad (2.22)$$

2.2.1.3 Dirac Delta Function

The charge density distribution function in the space of a unit point charge is a δ function. The charge density ρ is infinite at its origin and zero everywhere else. The total charge in the entire space is: $\int \rho d\tau = 1$.

The δ function has the following characteristics:

$$\delta(x - x_0) = \begin{cases} 0 & \text{if } x \neq x_0 \\ \infty & \text{if } x = x_0 \end{cases} \quad (2.23)$$

$$\int_{-\infty}^{\infty} \delta(x - x_0) dx = 1 \quad (2.24)$$

$$\int_{-\infty}^{\infty} f(x)\delta(x - x_0) dx = f(x_0) \quad (2.25)$$

2.2.2 Fourier Expansion and Fourier Transform

When we use $1, \cos(nx), \sin(nx)$ or $\exp(i\omega t), \exp(ikx)$ as basis function, equations (2.14)-(2.15) are the Fourier Expansion and Fourier Transform.

2.2.2.1 Fourier Expansion and Fourier Transformation

Theorem 1: Any periodic function can be superimposed by an infinite sum of sine and cosine functions:

$$f(x) = \frac{a_0}{2} + \sum_{n=1}^{\infty} (a_n \cos(nx) + b_n \sin(nx)) \quad (2.26)$$

When the variable represents time t , the coefficient sequence is called a frequency domain representation and can be written as:

$$f(t) = \frac{a_0}{2} + \sum_{n=1}^{\infty} (a_n \cos(n\omega t) + b_n \sin(n\omega t)) \quad (2.27)$$

The frequencies here are discrete and form a non-continuous spectrum.

Theorem 2: Any non-periodic function can be formed by a series of exponential functions.

$$f(t) = \frac{1}{\sqrt{2\pi}} \int_0^{\infty} F(\omega) \exp(-i\omega t) d\omega \quad (2.28)$$

$$f(t) = \frac{1}{\sqrt{2\pi}} \int F(k) \exp(ikx) dk \quad (2.29)$$

$$f(\vec{r}) = \frac{1}{(2\pi)^{3/2}} \int F(\vec{k}) \exp(i\vec{k}\vec{r}) d\vec{k} \quad (2.30)$$

where ωt and kx are called phases, and the frequencies here are continuous spectrum.

2.2.2.2 Fourier Transform

To solve for the coefficient $F(\omega)$ or $F(k)$ in equations (2.28)-(2.30) involves what is called a Fourier transform, namely finding the spectrum. The Fourier transform is very useful in that it can transform differential equations into algebraic ones.

$$F(\omega) = \frac{1}{\sqrt{2\pi}} \int_{-\infty}^{\infty} f(t) \exp(i\omega t) dt \quad (2.31)$$

$$F(k) = \frac{1}{\sqrt{2\pi}} \int_{-\infty}^{\infty} f(x) \exp(-ikx) dx \quad (2.32)$$

2.2.2.3 X space and K space

A function formed by $f(x)$ above is called x -representation or a function in the x -space. A function formed by $F(k)$ is called k -representation or a function in k -space. The x -space is usually considered the coordinate space and the K space the momentum space.

2.2.3 Partial Differential Equations

The study of a physical problem is often transformed into a pure mathematical model in order to find a solution. These mathematical models usually have three main components:

- Partial differential equations
- Boundary condition
- Initial condition

2.2.3.1 Helmholtz Equation

The Helmholtz equation is the partial differential equation (PDE) that groups the three types of common PDEs using the steady-state solution (i.e. separation of space and time):

$$(\nabla^2 + k^2)\Psi = 0 \quad (2.33)$$

where ∇ is the Laplacian operator and k is the wave vector. This equation results from applying the technique of separation of variables (i.e. space and time) to reduce the complexity of the analysis.

For example, consider the wave equation:

$$\nabla^2\Psi - \frac{1}{c^2} \frac{\partial^2\Psi}{\partial t^2} = 0 \quad (2.34)$$

Letting $\Psi(\vec{r}, t) = e^{i\omega t}\Psi(\vec{r})$, $\frac{\partial}{\partial t} = i\omega$, $\frac{\partial^2}{\partial t^2} = -\omega^2$, we obtain:

$$\nabla^2\Psi(\vec{r}) + \frac{\omega^2}{c^2}\Psi(\vec{r}) = 0 \quad (2.35)$$

$$\xrightarrow{k^2 = \frac{\omega^2}{c^2}} \nabla^2\Psi(\vec{r}) + k^2\Psi(\vec{r}) = 0 \quad (2.36)$$

Also, consider the diffusion equation:

$$\nabla^2\Psi - \frac{1}{D} \frac{\partial\Psi}{\partial t} = 0 \quad (2.37)$$

Letting $\Psi(\vec{r}, t) = e^{-\lambda t}\Psi(\vec{r})$, $\frac{\partial}{\partial t} = -\lambda$, we obtain:

$$\nabla^2\Psi(\vec{r}) - \frac{\lambda}{D}\Psi(\vec{r}) = 0 \quad (2.38)$$

$$\xrightarrow{k^2 = \frac{\lambda}{D}} \nabla^2\Psi(\vec{r}) - k^2\Psi(\vec{r}) = 0 \quad (2.39)$$

2.2.3.2 Boundary Conditions

There are three types of boundary conditions:

1. Dirichlet boundary condition: function value on the boundary $u|_{\sigma}$
2. Neumann boundary condition: first-order derivative value on the boundary $\frac{\partial u}{\partial n}|_{\sigma}$
3. Cauchy boundary condition: function value of the linear combination on the boundary $u + \frac{\partial u}{\partial n}|_{\sigma}$

Theorem: The Helmholtz differential equation has a unique solution if it satisfies any one of the three boundary conditions.

2.2.3.3 Solving the Helmholtz Equation

Separation of Variables

1. The Helmholtz Operator Is a Hermitian Operator

The Helmholtz operator $\nabla^2 + k^2$ in a Helmholtz equation is a Hermitian operator. Hermitian operators have real eigenvalues, orthogonal eigenfunctions, and corresponding eigenfunctions, that form a complete bi-orthogonal system when it is second-order and linear.

The complete solution of a Helmholtz differential equation is a superposition state by all intrinsic states (that is, eigenfunctions):

$$\Psi = \sum c_n \varphi_n \quad (2.40)$$

where coefficient c_n expresses eigenstate φ_n in the superposition state Ψ of size $\frac{|c_n|^2}{\sum_n |c_n|^2}$.

2. Homogeneous Condition

The condition making it possible to use separation of variables for solving a partial differential equation is that the partial differential equation and its boundary condition must be homogeneous. For non-homogeneous equations, we must utilize the Fourier expansion solution of its corresponding homogeneous equation, using the eigenfunction of the boundary conditions. If the boundary condition is also non-homogeneous, the boundary condition must be transform into a homogeneous condition using variable transformation.

3. Selection of Eigenfunctions and Eigenvalues

The key to solving a Helmholtz equation using separation of variables is to determine the eigenfunctions, and eigenvalues and adopt the principle of superposition. Eigenfunctions are determined by the choice of coordinate system. The eigenvalues are determined by the boundary conditions: (1) bounded eigenvalues are discrete and (2) unbounded eigenvalues are continuous.

- General Solution in the Cartesian Coordinate System

$$\Psi(x, y, z) = \sum_k C_k \exp(i\vec{k} \cdot \vec{r}) \quad (2.41)$$

$$k^2 = k_x^2 + k_y^2 + k_z^2 \quad (2.42)$$

- General Solution in the Cylindrical Coordinate System

$$\Psi(\rho, \varphi, z) = \sum_n C_n Z_n(k_\rho \rho) \exp(i(n\varphi + k_z z)) \quad (2.43)$$

$$k^2 = k_\rho^2 + k_z^2, n = 0, 1, 2, \dots \quad (2.44)$$

where the cylindrical function $Z_n(k_\rho \rho)$ is:

$$Z_n = \begin{cases} I_n & K_n & \text{if } k < 0 \\ J_n & N_n & \text{if } k > 0 \\ \rho^n & \rho^{-n} & \text{if } k = 0 \end{cases} \quad (2.45)$$

1. If $\frac{\partial}{\partial \varphi} = 0$, then $n = 0$:

$$\Psi(\rho, z) = Z_0(k_\rho \rho) \exp(ik_z z) \quad (2.46)$$

2. If $\frac{\partial}{\partial z} = 0$, then $k_z = 0$:

$$\Psi(\rho, \varphi) = a + b \ln(\rho) + \sum_{n=1}^{\infty} (A_n \cos(n\varphi) + B_n \sin(n\varphi)) \rho^n + \sum_{n=1}^{\infty} (C_n \cos(n\varphi) + D_n \sin(n\varphi)) \rho^{-n} \quad (2.47)$$

- General Solution in the Spherical Coordinate System

$$\Psi(r, \theta, \phi) = \sum_{nlm} C_{nlm} R_n(r) Y_{lm}(\theta, \phi) \quad (2.48)$$

$$k^2 = k_r^2 + k_\theta^2 + k_\phi^2 \quad (2.49)$$

where,

$$\frac{1}{r^2} \frac{d}{dr} \left(r^2 \frac{dR_l}{dr} \right) + \left(k^2 - \frac{l(l+1)}{r^2} \right) R_l = 0 \quad (2.50)$$

$$R(r)r|_{r=0} = 0 \quad (2.51)$$

4. Fourier Transform for Differential Equation

The differential equation after the Fourier transform is a dispersion relation $F(k, \omega)$, i.e. the equation in K space. We can obtain a generalized transformation of the differential equation by using orthogonal normalized bases and Dirac notation in Heisenberg's matrix equation (Equation (2.22)).

5. Power Series Solution

The separation of variables reduces the second-order partial differential equation to a few second-order ordinary differential equations. Any second-order ordinary differential equation can be transformed into a SL equation (Sturm - Liouville equation). The majority of such equations start with a power series solution that can later be defined as a special function.

Integral Transform

There are two ways to solve the Helmholtz Equation using the integral transform method:

1. **Narrow Fourier transform:** Transform a differential equation into an algebraic dispersion equation $F(\omega, \vec{k}) = 0$, by $\frac{\partial}{\partial t} = -j\omega$ and $\nabla = j\vec{k}$, which is called K space or momentum space.
2. **Generalized Hilbert space expansion:** Transform a differential equation into a Heisenberg's matrix equation.

The integral transform method of solving equations has three main steps:

1. Fourier transform on both sides of the equation for some variable x
2. Solve the equation of the image function
3. Inverse Fourier transform

The integral transform method is particularly suitable for the solution of unbounded equations.

Green's Function

Considering any field $E(\vec{r}, t)$ generated by a source $\rho(\vec{r}, t)$, we can solve for the complete field by superimposing the field generated by a point source of δ type, according to the principle of superposition. The field generated by the point source of δ type is called Green's function. Therefore, the Green's function method is an integral kernel that can be used to solve an inhomogeneous differential equations subject to specific initial conditions or boundary conditions.

Suppose we have the following differential equation, for any arbitrary linear differential operator \hat{L} :

$$\hat{L}y = f(x) \tag{2.52}$$

Define the Green's function $G(x, x')$ by:

$$\hat{L}G(x, x') = \delta(x - x') \tag{2.53}$$

Then the solution to Equation 2.52 is:

$$y = \int G(x, x')f(x')dx' \tag{2.54}$$

Approximation Method

Physical problems are often too complicated to obtain an analytical solution, so that we must then use an approximation method. The most common approximation methods are: (1) variation method and (2) perturbation method. Details on this approximation method are beyond the scope of this thesis and readers are encouraged to refer to [37].

2.3 Neuroanatomy Background

One of the crucial goals of diffusion MRI-based neurological investigations is to identify biomarkers that are reliable identifiers and predictors of neurological disorders. An ideal

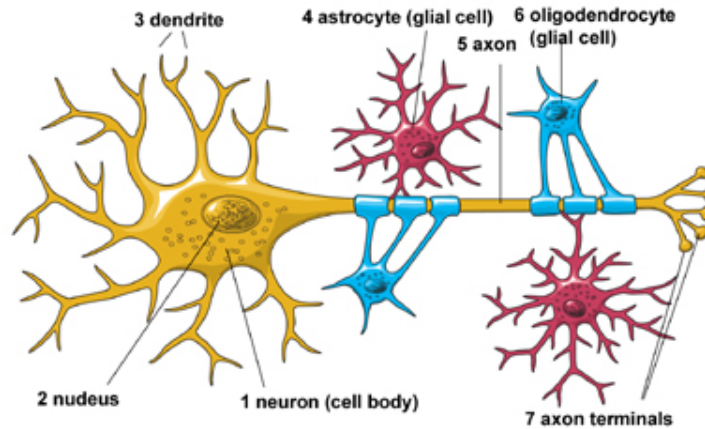


Figure 2.3: Axon scheme. The axon is the core fiber extending out of the neuronal cell body that facilitates communication between gray matter and the rest of the body.

biomarker should (1) evaluate the severity of the disorder, (2) predict future clinical disease progression; in addition, (3) changes in the biomarker should correlate with clinical changes.

2.3.1 Microstructural Components of the CNS White Matter

The white matter of the central nervous system (CNS) consists mainly of axons and their surrounding fatty tissue, myelin sheaths. The myelin sheath is a layer around the axon that keep it insulated in order to increase the speed at which impulses propagate along the myelinated fiber. Myelinated axons are white in appearance, hence the term "white matter" of the brain (Figure 2.4). Not all axons are myelinated, some axons of smaller diameters ($< 1\mu m$) have a thin myelin membrane or none at all (non-myelinated axons).

The axon is the core fiber extending from the neuronal cell body that facilitates communication between gray matter and the rest of the body. Most axons lie parallel to one another within a white-matter tract [51]. A schematic representation of the axon is shown in Figure 2.3 and a detailed description of the axonal cytoskeleton is given in Nixon [72]. The axon has a small diameter, ranging from less than $0.3\mu m$ up to $10\mu m$ in humans. Examples of the diameter ranges in humans and rhesus monkeys are given in Table 2.1. Since a single voxel in diffusion MRI is on the order of $1 - 3mm$, it contains hundreds of thousands of individual axons. Axons can extend over long distances: the longest axon in human (corticospinal tract) extends all the way from the cerebral cortex in the brain to the base of the spinal cord (with a length of almost $2/3$ of a body's height, about a meter or more). The diameter of the axon remains relatively constant throughout its length [40]. The axon diameter directly affects nerve function in the brain. The conduction velocity

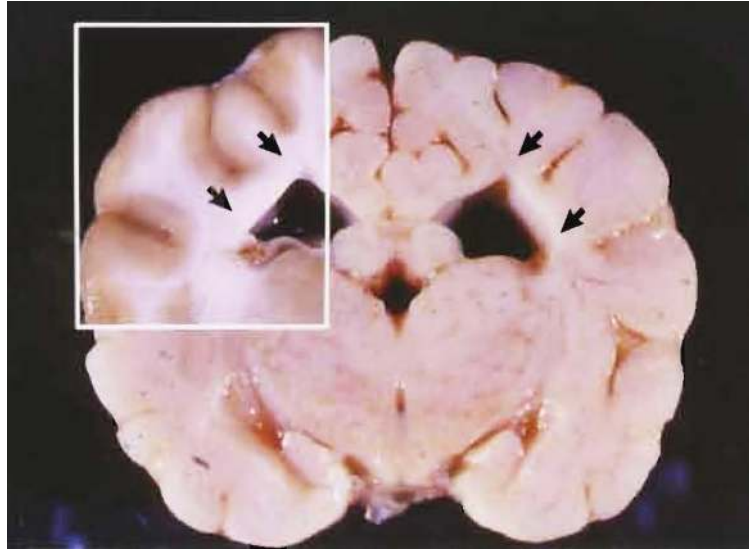


Figure 2.4: The myelin sheath around the nerve fibers (axons) renders the tracts white. In the area in white matter that lacks myelin, as in this dysmyelinated dog brain, white matter may appear semi-translucent (indicated by the arrows at upper left). Image from [51].

of the axon increases linearly with increasing diameters in myelinated axons [86, 104] and is maximal when the ratio of axonal diameter to that of the fiber (axon + myelin sheath) is around 0.6 [51] (this ratio is also called the *g-ratio*), as illustrated in Figure 2.5. For example, the corticospinal tracts predominantly contain axons with larger diameters, which enable fast communication and reaction times. Smaller-radius axons generally arise in neuronal pathways that permit slower communication and favor duality of information, as in the optic nerve and pain control pathways.

Although the *corpus callosum* (CC) is considered one of the most highly ordered white-matter structures, its microstructural heterogeneity is evident. Different fiber tracts project through the CC to reach and communicate with different cortical areas. Due to the different functions of these tracts, the microstructures of these segments shows obvious differences in axon density, axon size and unmyelinated axon quantities. Based on axon properties and the fiber tracts' projection areas, the CC consists of characteristic subregions of axons and contains different proportions of myelinated and unmyelinated fibers [60, 2].

Figure 2.6 is a summary diagram of five brain subregions. Figure 2.6.A shows the different axon compositions as based on microstructural-sector analysis of the CC from electron microscopic study of eight adult rhesus monkeys [60]. The anterior portions (prefrontal) of the CC contained the greatest proportion of unmyelinated axons and myelinated axons with the smallest diameters ($< 0.5 \mu m$). The middle and posterior portions contained the

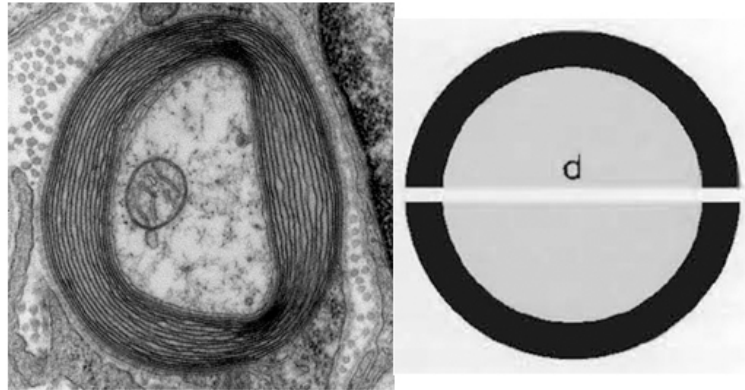


Figure 2.5: g-ratio, the ratio of the axonal diameter to that of the fiber (axon + myelin sheath). Conduction velocity is maximal when the g-ratio is around 0.6. Image from [51].

fewest unmyelinated axons, which also consisted mostly of myelinated axons $> 2.5\mu m$ in diameter.

Both axon diameters and the proportion of axons that are myelinated influence axonal packing densities. The axonal packing density can vary greatly from one fiber tract to another. The microstructural differences found in [60] (Figure 2.6), correlate with the differences in axonal packing densities across the tract. The highest densities are found in the anterior portion, where the smallest axons are found, and the lowest densities are found in the middle and posterior portions, where large axons are observed. The overall average was 76.62 axons per $100\mu m^2$ and the total number of axons in the CC was calculated to be 56 million. A similar variation in axonal packing densities is found in human corpus callosum [60] and the rat spinal cord [89] (Figure 2.8).

Figure 2.6.B shows the topographic organization of projections through the tract from different cortical area in the rhesus monkey [78] scaled to the same size as in A. Note that the correspondence of these two independently established maps is remarkable. As mentioned

Species	White-matter tract	Range of diameters of myelinated axons	Range of diameters of unmyelinated axons	Reference
Human (adult)	pyramidal tract in medullary pyramid	< 0.3 to $10\mu m$	Not quantified	[43]
Rhesus monkey	corpus callosum (CC)	0.08 to $2.5\mu m$	0.08 to $0.5\mu m$	[59, 60, 96]

Table 2.1: Axon diameter range for human pyramidal tract in medullary pyramid and the Rhesus monkey in CC.

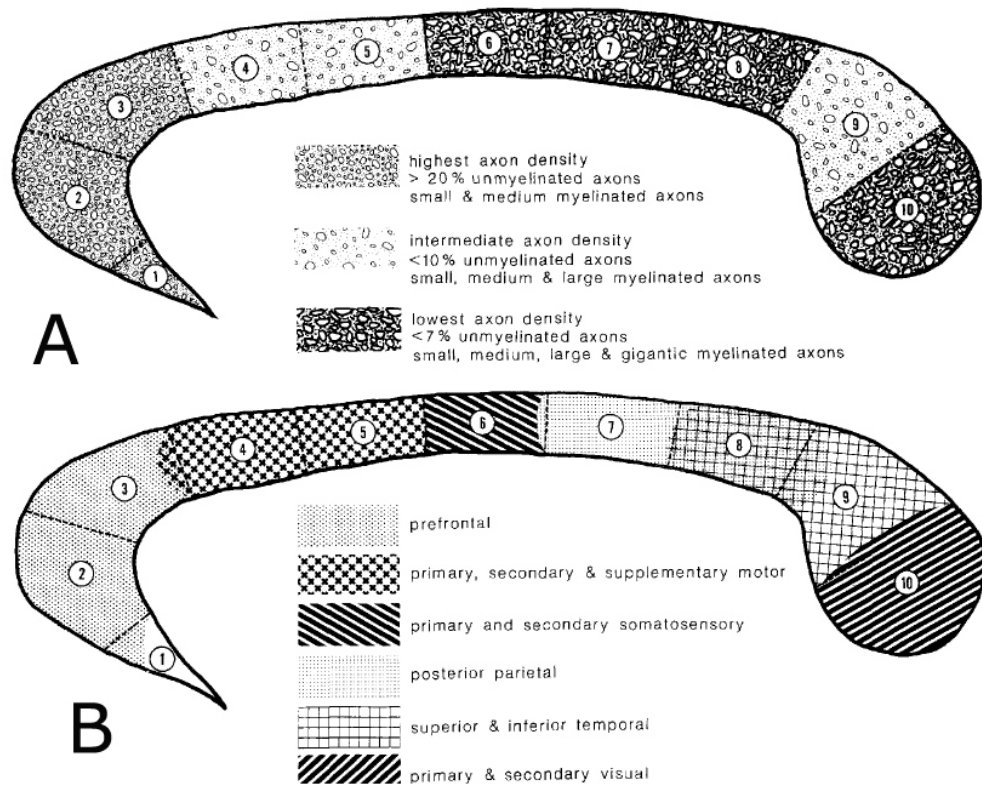


Figure 2.6: Five typical subregions of the rhesus monkey CC. A. The relationship among regional variation in axon composition (axon size, density, amount of unmyelinated axons) based on a microstructural-sector analysis by Lamantia et al. [60]. B. Topographic organization of projections through tracts from different cortical areas in the rhesus monkey [78] scaled to the same size as in A. Note that the organization of the CC correlates remarkably well in the two independent studies.

earlier, the axon diameter directly affects nerve function in the brain. This correlation explains the correspondence between the higher-order association regions of the frontal lobes and the high concentration of small, medium myelinated, and unmyelinated axons, as well as the coincidence of the giant axons, lowest axon density, and lowest percentage of unmyelinated axons within the primary somatosensory and primary visual regions of the corpus callosum.

Figure 2.7 shows an electron micrograph of axons in two different sections of the corpus callosum in an adult rhesus monkey [60]. Figure 2.7.A shows the axons from section 2 (see Figure 2.6 for definitions). This region mostly contains small and medium axons with the highest density. Figure 2.7.B shows the axons from section 6 of the same corpus callosum shown in A. This region consists of large axons with the lowest axon density. In the center

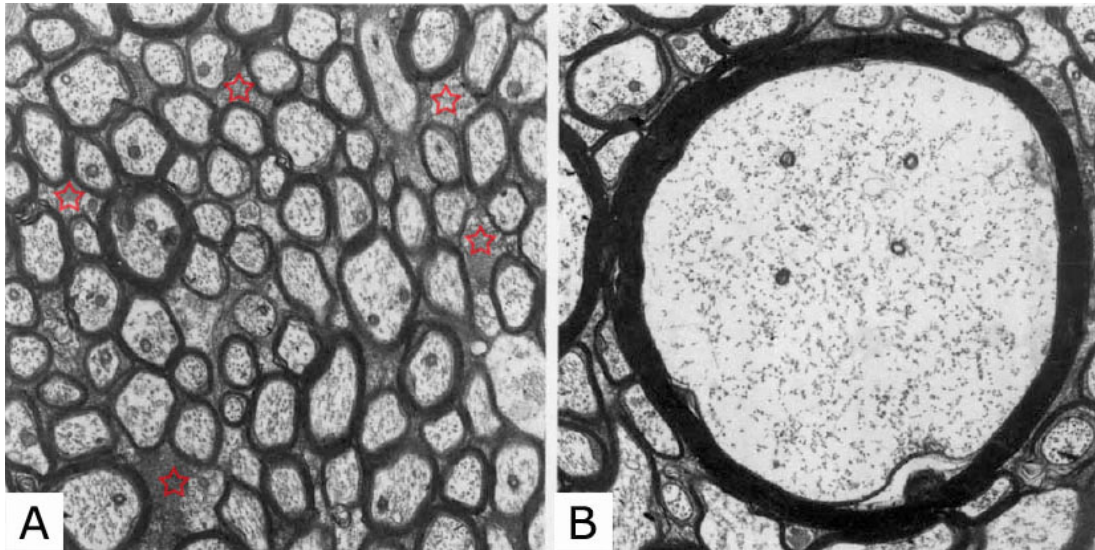


Figure 2.7: A. Electron micrograph of axons in section 2 of the corpus callosum in an adult rhesus monkey. Notice the small unmyelinated axons (red stars). B. Electron micrograph of axons in section 6 of the corpus callosum shown in A. In the center of this micrograph is an example of the very large axons encountered only in section 6, 7, and 10 of the corpus callosum. Both micrographs are $1 \times 10^{-4} \text{ mm}^2$. Image from [60].

of the micrograph is an example of a gigantic axon encountered only in sections 6, 7, and 10 of the corpus callosum.

2.3.2 Neurological Changes in Diseases

Various neurological changes, including axon diameter and densities, have been observed in a number of invasive histological studies of disease-affected tissue [16, 20, 57]. Loss of myelin results in a reduction in tissue viscosity and elasticity, and an increase in permeability [58]. The increased water content of a tissue causes changes in tissue density and viscosity [67]. These studies indicate that axon properties (such as axon radius and density) are important quantities to measure as direct biomarkers for neurological diseases.

Two of the most common effects of disease on white-matter structure are demyelination and axonal degeneration. Demyelination and axonal degeneration in white matter are critical since both myelinated and unmyelinated axons of the mammalian central nervous system do not regenerate. For instance, axonal degeneration has been identified as the dominant cause of the irreversible neurological disability seen in MS [15]. Studies suggest that axonal degeneration in MS is location specific, axon size selective, and correlates with gender [41, 62, 34, 100]. The average axon loss in the cortical spinal tract ranged from 15

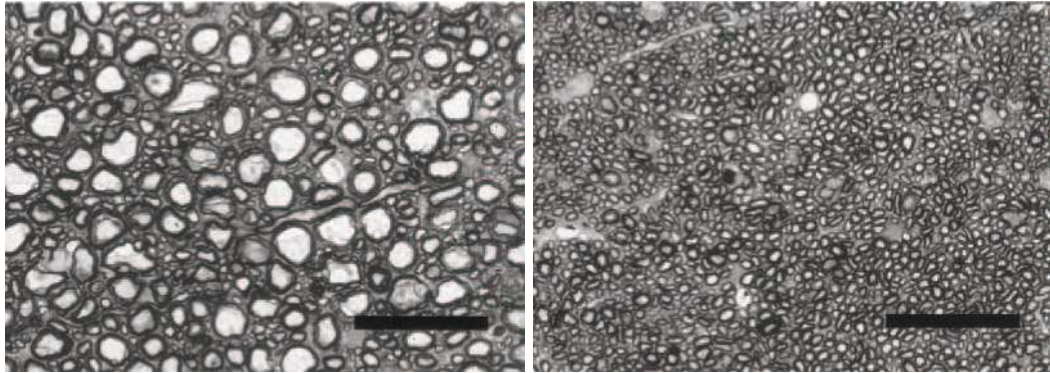


Figure 2.8: 1 μm thick histologic section of rat spinal cord. A. axons from vestibulospinal tract containing largest axons in this section of the spinal cord. B. axons from rubrospinal tract in the spinal cord where axon size appear to be much smaller and axons are more densely packed. (black bar= $50 \mu\text{m}$) Images from [89].

to 33% in a *post mortem* MS tissue analysis from adult humans [33]. Axonal loss ranged from 45 to 84% in demyelinated lesions of the spinal cord in a separate study [14]. It has been shown that small-axon fibers ($\leq 3 \mu\text{m}$ in diameter) are particularly affected and tend to be more vulnerable to axonal loss in MS. Large-axon fibers remain relatively preserved [41, 34]. Significant differences between healthy and diseases regions of the spinal cord may be localized and can be clearly identified in histology images (Figure 2.9)

In addition, various microstructural changes have been observed in a number of diseases. Changes in axon diameter distribution have been observed in autism [81, 47], amyotrophic lateral sclerosis (ALS) [30, 46], and schizophrenia [83, 85]. A water exchange mechanism between different compartments of white matter has been observed in stroke patients [61].

2.3.3 Histological Methods: Microscopic Examination

Despite the importance of the axonal properties discussed in the previous section, they have not been reliably measurable *in vivo*. Microscopic histology examination is considered fundamental in the investigation of central nervous system structure. However, the two primary microscopic methods, light microscopy and electron microscopy, are both invasive procedures and the implications for the quantification of cell size and densities of the tissue elements must be considered.

First, tissue preparation procedure is difficult and tedious. It entails chemical fixation, dehydration, and embedding the tissue in a chemical medium for fixation. The results of the procedure are subject to many artifacts, including tissue shrinkage and cracking (shrinkage values between 0.71 and 0.65 have been estimated [2, 33])). Therefore, the cellular and axon

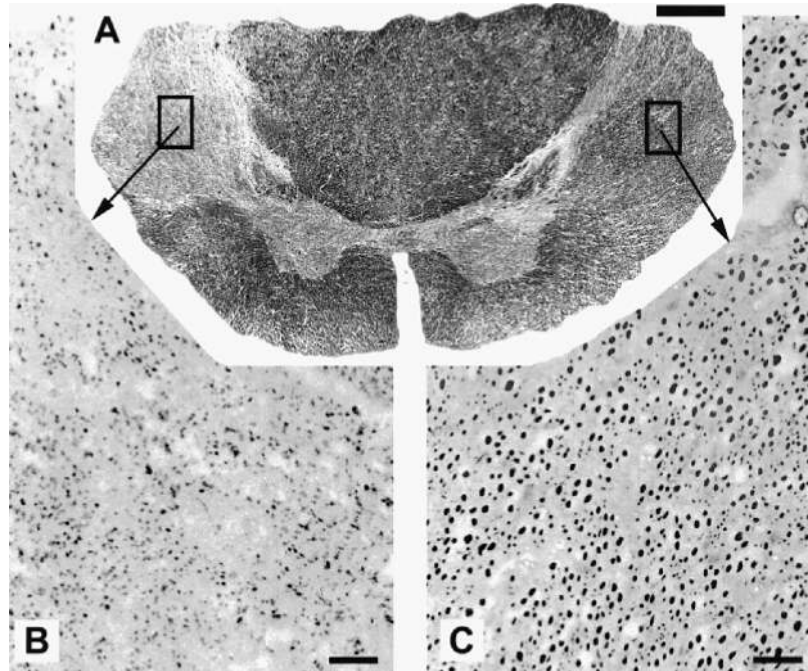


Figure 2.9: Histology images of a multiple sclerosis spinal cord sample. Completely demyelinated plaque with changes in axon diameter can be observed on the left, while normal white matter is on right (thick bar=2mm, thin bar=10 μm). Image from [62]

densities obtained from these histology procedures are probably higher than those existing in fresh tissue. Also, cell density values vary depending on the thickness of the section in which they are contained. It has also been observed that light microscopic methods may not be sensitive enough to detect all small white-matter elements. In addition, about 20% of axons observed in electron microscopy cannot be discerned by light microscopy [2]. These factors should be considered when (1) comparing histology results obtained using different microscopic techniques and (2) comparing *ex-vivo* histology results with in-vivo live tissue axonal property estimations.

Part I

**Brain White Matter
Microstructural Analysis**

Chapter 3

Microstructural Analysis Using Double-Pulsed Field Gradient MR

Here we present a computational technique (DoubleAx) for inferring axonal properties using angular double-pulsed field gradient (double-PFG) MRI. Our method uses a two-compartment analytical diffusion model taking into account finite gradient pulses. We demonstrate the feasibility of estimating axonal properties from three sets of Monte Carlo simulation data and four sets of live human data. The Monte Carlo data is simulated in the human brain range: one set with uniform axon radius and two sets with distributed axon radii.

Our simulation results are the first to use clinically feasible low- q angular double-PFG experiments without prior knowledge of axon orientation to demonstrate the feasibility of estimating specific axonal properties including axon radii, distribution, orientation and volume fraction. This makes it possible to estimate axonal properties for the whole brain. Simulation data lets us go beyond previous work to provide a complete study combining a set of characteristics that other work has used but never unified. We (1) study the full range of axon sizes in the human brain including small axons ($< 3 \mu m$) that are particularly challenging with improved sensitivity, (2) model both intra- and extra-axonal space with a two-compartment model, (3) account for variation in axon radii with a gamma distribution, and (4) restrict our experimental parameters to clinically feasible gradients utilizing the angular dependency of the signal decay in double-PFG. These estimation results agree well with the simulation ground truth and demonstrate that double-PFG MRI can accurately reveal these underlying axonal properties.

The computational approaches were then applied to four datasets from two live human

subjects to validate their feasibility in extracting microstructural properties accurately in brain tissue using a clinical 3T MRI scanner. Our results demonstrate sensitivity to human microstructural properties and verify microstructural variation along the *corpus callosum* (CC) known from histology.

3.1 Introduction and Related Work

Diffusion MRI, which measures the diffusion of spins in tissues, is a popular technique for assessing a number of neurological disorders because of its sensitivity to the micro-geometry of the underlying tissue. Current diffusion MRI brain studies rely on indirect diffusivity-based measures such as fractional anisotropy (FA) as biomarkers of major axonal changes [80, 105]. The fact that FA is a nonspecific summation index of the observed diffusion signal over the entire voxel means that it is unable to distinguish among different changes in axon radius, orientation, packing density, and myelin permeability [8]. Studies have shown that neuronal changes in these axonal properties occur in early stages of brain diseases [62] and have been observed to be location specific and axon-size selective [39, 41]. Measuring and analyzing these specific pathological axonal changes *in vivo* may provide early indications of such brain diseases as multiple sclerosis (MS); indeed, recent experiments have found that axonal degeneration is the dominant cause of irreversible neurological disability in MS [15, 95].

Axonal properties can be inferred by constructing a geometric model of the underlying tissue in which water molecules are diffusing and analyzing the diffusion MRI signals [4]. Various models of diffusion MR signal in white matter of the brain have been proposed; the details are beyond the scope of this chapter, but an extensive comparison is given in [77]. More specific axonal properties can be identified using the geometric model, including axon sizes, packing density, and orientation. Assaf *et al.*[9] constructed a two-compartment CHARMED model for single-pulsed gradient field (single-PGF) experiments. Later, they extended the CHARMED approach to design AxCaliber [7] to measure the axon diameter distribution of excised nerve tissues [7] and *in vivo* rat CC [11]. In AxCaliber, the gradient direction is fixed to be perpendicular to axon orientation and a multi-diffusion protocol is applied to allow multiple combinations of diffusion time and gradient strength for axon diameter estimation. Using AxCaliber, however, requires prior knowledge of axon orientation, lengthy data acquisition and high q -values (11 hr and $q_{max} = 511.08 \text{ cm}^{-1}$ in [7]), which can be difficult to achieve with current clinical scanners. Barazany [10] extended AxCaliber to allow arbitrary axon orientation by projecting data perpendicular to the predicted axon orientation from the CHARMED model. The high q -values required in

the single-PFG experiments, however, are not feasible on clinical scanners. In contrast, our low- q double-PFG sequence utilizes the angular dependency of signal decay instead of q -value dependency and restricts our experimental parameters to clinically feasible gradients.

It has recently become possible to estimate orientationally invariant fibers with clinically achievable parameters [4, 28, 29, 5]. These approaches optimize imaging protocols on a combination of HARDI shells in order to maximize sensitivity to axon parameters. Optimization requires good approximation of the axon size, which can be a problem in disease studies where the underlying axonal change is hard to predict. A simulation study [4] has shown that, when a single protocol is optimized for the typical constraints of a human scanner, axon radius is recovered with low variance for larger axons ($3 - 10 \mu m$ radius) but small axons ($1 - 2 \mu m$) became indistinguishable. This could be a problem for whole-brain mapping since the human brain axon radius is typically less than $5 \mu m$ [38]. Studies have shown that small-axon fibers ($< 3 \mu m$) tend to be vulnerable to axonal loss in MS while large-axon fibers remain relatively preserved [41, 62]. Later work [5] recovered a low-high-low trend in axon size along the human and macaque CC, consistent with recorded histology, but overestimation (in comparison to histology) of about $3 - 4 \mu m$ in axon diameter was reported there. Zhang [106] later improved the estimation results using a new tissue model to take into account the dispersion in tissue orientation that may have led to this axon size overestimation. Both studies [5, 106], however, provided only a single summary statistic as the axon size measure. Although this index is weighted by volume, it is still difficult to take into the distribution of axon radii in brain tissue. Unlike earlier work, our approach (1) accounts for the variation in axon radii and estimate this variation with a gamma distribution, (2) does not require optimization of the acquisition protocol, and (3) estimates axon orientation as part of the model and does not require prior knowledge of the axonal properties.

The double-PFG MR sequence (Fig. 3.1a) is the simplest form of multi-PFG MR first proposed by Cory [32]. It contains two pairs of diffusion gradients, G_1 and G_2 , separated by an angle ψ . Özarslan [74] showed that when two diffusion gradient pulse pairs are used (as in double-PFG), the wavenumber q -value necessary for non-monotonicity is exactly half that in single-PFG experiments [25]. This sensitivity of double-PFG makes it possible to probe small compartments using relatively low q -values. Mitra [68] predicted theoretically the angular dependence of signal intensity on the angle ψ in limiting cases of double-PFG experiments, not taking into account the finite duration of the diffusion time or mixing time. Violating these conditions generally leads to underestimation of pore size and eccentricity [54, 55]. Later, Özarslan [75] provided a theoretical solution for the angular dependence

of signal intensity in restricted geometries for arbitrary timing parameters. Shemesh [90] verified this angular dependence of the signal decay [75] in well-controlled experiments using water-filled microcapillaries of known diameters ($5 - 20 \mu m$). Kosh [56] applied both Mitra and Özarslan’s theory to human brain tissue. The compartment size estimates from the two theories, although reasonable, did not agree and were not validated. Özarslan’s theory has also been applied to yeast cells of about $5 \mu m$ [91] and glass capillary phantoms around $5 \mu m$, with results agreeing well with optical microscopy. The common brain tissue range of less than $5 \mu m$, however, is hard to achieve in these phantoms. Furthermore, most of these studies considered only a single axon radius per voxel, ignored extra-cellular space in the model, and used a high gradient range that is hard to achieve on clinical scanners (up to $G = 800 mT/m$ in [91], for instance). Simulation data lets us go beyond previous work to provide a complete study combining a set of characteristics that other work has used but never unified. Our work differs from previous double-PFG work in five ways: we (1) study the full axon radius range of the human brain, from 1 to $5 \mu m$, (2) take into account the variation in axon radii and estimate this variation with a gamma distribution, (3) model both intra- and extra-axonal space of the microstructure, (4) estimate axon orientation as part of the model, and (5) restrict our experimental parameters to clinically feasible gradients.

Here, we propose a computational technique (DoubleAx) for inferring specific axonal properties with low- q angular double-PFG MRI using an analytical diffusion model based on Özarslan’s theory [75]. Our model uses a two-compartment geometric assumption for the underlying microstructure and takes into account finite pulses in the double-PFG experiments. We demonstrate the feasibility of estimating axon radii and their distributions in the typical human brain tissue range (1 to $5 \mu m$), along with axon orientation and intra-axonal volume fraction using both Monte Carlo simulation data and live human data. Our preliminary work studied axon models under higher gradients [113, 111, 114]. In this chapter, we extend this work to provide a complete study of uniform and distributed axon models unifying a set of modeling and experimental characteristics at lower clinically feasible gradients tested on live human datasets.

3.2 Imaging Protocol

The double-PFG sequence (Figure 3.1a) first proposed by Cory [32] is the simplest form of multi-PFG and has been shown to reduce eddy current distortions [84]. Double-PFG offers many degrees of freedom; details are beyond our scope here but are reviewed in [92]. For our modeling, we focus on the angular double-PFG experiment illustrated in Figure 3.1.

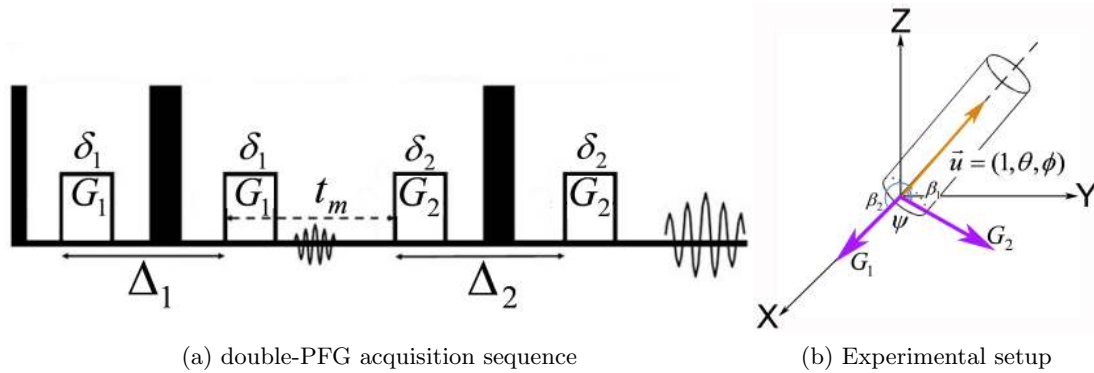


Figure 3.1: (a) double-PFG acquisition sequence with two encoding intervals of gradient G_1 and G_2 . (b) Experimental setup: $\mathbf{u} = (1, \theta, \phi)$ defines the arbitrary axon orientation; G_1 is fixed on the x-axis and the angle of G_2 is varied linearly on the xy-plane; β_1 and β_2 denote the angle between \mathbf{u} and G_1, G_2 respectively.

In angular double-PFG experiments, two pairs of diffusion gradients, G_1 and G_2 , are applied at any angle. The two encoding intervals are separated by a mixing time t_m with diffusion time Δ_1 and Δ_2 and pulse duration δ_1 and δ_2 . During each acquisition sequence, the diffusion time, pulse duration, and mixing time are fixed and the angle ψ between G_1 and G_2 is varied (Figure 3.1b). This sequence can be repeated for different diffusion times, pulse durations, and mixing times.

Double-PFG experimental parameters must satisfy two conditions: first, the long-diffusion wavelength condition: $\Lambda^2 \gg a^2$ (where diffusion wavelength $\Lambda = \frac{1}{\gamma\delta G}$), and second, the diffusion-time condition: $\Delta > \frac{a^2}{2D_i}$: diffusion periods must be long enough for spins to probe the boundary and experience restricted diffusion.

3.3 Geometric Tissue Model

We first construct a geometric model of axons within which water molecules are diffusing in order to analyze the MR signal attenuation in double-PFG experiments. Each voxel (1 – 3 mm) in the MRI contains signal from hundreds of thousands of individual axons (1 – 5 μm). Since axons size remain relatively constant throughout their length [40] and appear circular in electron microscopy images (Figure 3.2a- 3.2b), we model axons as cylinders to best capture the geometric properties of the structure.

We include two classes of axon models: (1) axons with uniform radius within a voxel (Figure 3.2c) and (2) axons with gamma distributed radii within a voxel (Figure 3.2d). For both classes, the geometric model has two compartments, similarly to CHARMED [9]: (1)

the *intra-axonal compartment* i - the space inside axons of radius a represented by parallel non-abutting cylinders; here water molecules trapped inside the cylinders exhibit restricted diffusion, and (2) the *extra-axonal compartment* e - the homogeneous substrate space outside axons; here water molecules exhibit hindered diffusion. Axon boundaries are assumed to be impermeable and there is no exchange between the two compartments.

3.4 Analytical Diffusion Model

We present an analytical water-diffusion model aimed at estimating axonal properties without prior knowledge of axon orientation using angular double-PFG experiments based on [75]. The model analyzes the MR signal obtained in double-PFG experiments given the two-compartment geometric model described in Sec. 3.3. We aim to extract the following axon parameters from the diffusion model:

- Axon radius:
 - Uniform model: axon radius a
 - Distributed model: mean axon radius $\bar{a} = \alpha\beta$, where α and β are shape and scale parameter of the gamma distribution respectively.
- $\mathbf{u} = (1, \theta, \phi)$, the axon orientation
- $f \in (0, 1)$, the volume fraction of the intra-axonal compartment
- D , the diffusivities of the axonal compartments

3.4.1 NMR Signal Attenuation in Double-PFG MR

The gradient profile of a general NMR gradient waveform can be approximated by a train of impulses [26]. We divide the time axis into M intervals of duration τ as suggested in [74]. The magnitude of the wavenumber q in the i th interval ($1 \leq i \leq M$) is:

$$\vec{q}_i = \frac{\gamma}{2\pi} \int_{t_i - \tau/2}^{t_i + \tau/2} G(\vec{t}) dt \quad (3.1)$$

The motion of molecules undergoing diffusion can be described by the conditional propagator, $P_s(\mathbf{r}_0|\mathbf{r}, t)$, an ensemble-averaged probability density for spin displacement from \mathbf{r}_0 to \mathbf{r} over time t . $P_s(\mathbf{r}_0|\mathbf{r}, t)$ obeys the Fick's Law differential equation governing $P_s(\mathbf{r}_0|\mathbf{r}, t)$:

$$\frac{\partial P_s^{(1)}}{\partial t} = D_1 \nabla^2 P_s^{(1)} \quad (3.2)$$

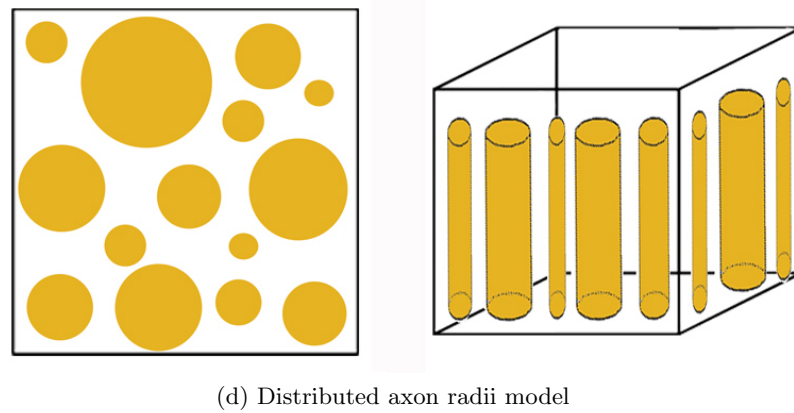
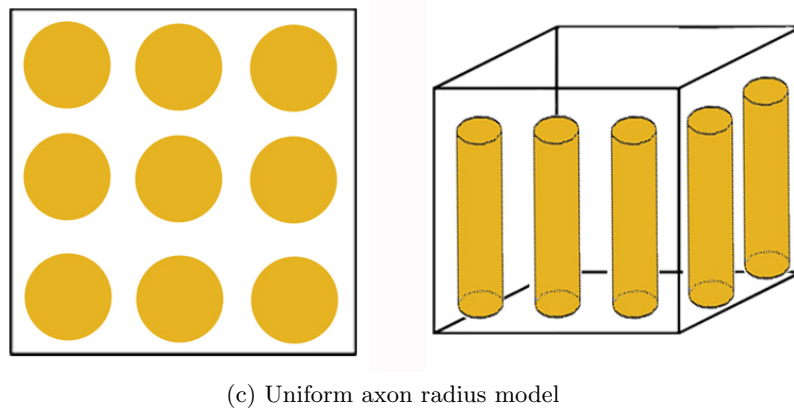
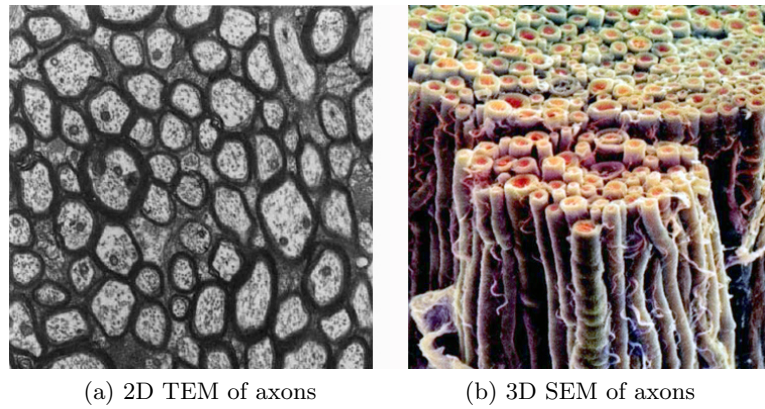


Figure 3.2: Geometric tissue model: (a) 2D cross-sectional view of axons in the CC of an adult rhesus monkey from transmission electron micrograph (TEM), image reproduced from [60]. (b) 3D view of axons from scanning electron micrograph (SEM), image reproduced from [22]. (c-d) 2D and 3D schematic views of a non-abutting rectangular arrangement of cylinders representing: (c) axons with uniform radius and (d) axons with distributed radii.

The diffusion problem posed in Eq. (3.2) above may be solved using the standard eigenmode expansion [23]:

$$P_s^{(1)}(\mathbf{r}_0|\mathbf{r}, t) = \sum_{n=0}^{\infty} C_n e^{-\lambda_n t} u_n(\mathbf{r}_0) u_n^*(\mathbf{r}) \quad (3.3)$$

where the $u_n(\mathbf{r})$ are orthonormal sets of solutions to the Helmholtz equation parameterized by the eigenvalue λ_n . Using the discretization scheme in Eq. (3.1), we can then approximate the NMR signal attenuation by a train of impulses using a series of propagators as a matrix product [24]:

$$E(\vec{q}) = S^T(\vec{q}_1) R(\tau) A(\vec{q}_2) \dots A(\vec{q}_{n-1}) R(\tau) S^*(-\vec{q}_n) \quad (3.4)$$

where:

- S is an M -dimensional vector whose k th component is given by the following integral over the pore volume V :

$$S_k(q) = \frac{1}{\sqrt{V}} \int u_k(\vec{r}) \exp(i2\pi\vec{q} \cdot \vec{r}) d\tau \quad (3.5)$$

- R is an $M \times M$ diagonal matrix:

$$R(\tau) = \exp(-\lambda_k \tau) \quad (3.6)$$

- A is an $M \times M$ matrix with components:

$$A_{km}(\vec{q}) = \langle k | \exp(i2\pi\vec{q} \cdot \vec{r}) | m \rangle = \int u_k^*(\vec{r}) u_m(\vec{r}) \exp(i2\pi\vec{q} \cdot \vec{r}) d\tau \quad (3.7)$$

Based on Eq. (3.4), we can model free and restricted diffusion as:

$$E_{free} = \exp\left(-\gamma^2 D_e \int_0^T dt \left| \int_0^t G(t') dt' \right| \right) \quad (3.8)$$

$$E_{rst} = 1 - 2\gamma^2 a^2 \sum_{n=1}^{\infty} S_{D_n} \int_0^T dt e^{\omega_{D_n} t} G(\vec{t}) F_{D_n}(\vec{t}) \quad (3.9)$$

where,

- $F_{D_n} = \int_0^T G(\vec{t}') \exp(-\omega_{D_n} t') dt'$
- $S_{D_n} = \frac{1}{\alpha_{D_n}^2 (\alpha_{D_n}^2 - D + 1)}$
- $\omega_{D_n} = \frac{\alpha_{D_n}^2 D}{a^2}$
- α_{D_n} are the roots of the derivatives of the first-order Bessel functions satisfying the boundary condition.

3.4.2 Uniform Axon Radius Model

Here, we model the diffusion signal for a single fiber population with uniform axon radius based on Eq. (3.4). We model the combined normalized MR signal attenuation E from these two compartments as a linear combination of each since we assumed no water exchange between them:

$$E = (1 - f)E_e + fE_i \quad (3.10)$$

where E_e and E_i are the normalized MR signal attenuation from the extra- and intra-axonal compartments respectively and f is the volume fraction of the intra-axonal compartment, reflecting axon packing density. Axon packing density varies in different tissues and in different locations of the same tissue structure.

We model the normalized MR signal attenuation in the extra-axonal compartment e as free diffusion derived based on Eq. (3.8):

$$E_e = \exp(-\gamma^2 \delta^2 D_e (\Delta - \frac{\delta}{3})(G_1^2 + G_2^2)) \quad (3.11)$$

In our experiment, the two encoding intervals of gradients G_1 and G_2 have the same pulse duration ($\delta_1 = \delta_2 = \delta$) and diffusion time ($\Delta_1 = \Delta_2 = \Delta$).

We further decompose the normalized MR signal attenuation in the intra-axonal compartment i inside axons into two components that are parallel ($E_{i//}$) and perpendicular ($E_{i\perp}$) to the axon orientation. Thus the combined MR signal attenuation in the intra-axonal compartment E_i is:

$$E_i = E_{i//} \times E_{i\perp} \quad (3.12)$$

We model $E_{i//}$ again as free diffusion:

$$E_{i//} = \exp\left(-\gamma^2 \delta^2 D_i (G_1^2 \cos^2 \beta_1 + G_2^2 \cos^2 \beta_2) (\Delta - \frac{\delta}{3})\right) \quad (3.13)$$

The signal component perpendicular to the axon orientation $E_{i\perp}$ is modeled by restricted diffusion in cylinders derived from Eq. (3.9):

$$E_{i\perp} = C + A(G_1^2 \cos^2 \beta_1 + G_2^2 \cos^2 \beta_2) + B(G_1 G_2 \cos \beta_1 \cos \beta_2) \quad (3.14)$$

where,

$$C = 1 - A(G_1^2 + G_2^2) - B(G_1 G_2 \cos \psi) \quad (3.15)$$

$$A = 2\gamma^2 a^2 \sum_{n=1}^{\infty} S_n \left[\frac{2\delta}{\omega_n} - \frac{1}{\omega_n^2} (2 - 2e^{-\omega_n \delta} + e^{-\omega_n(\Delta-\delta)} - 2e^{-\omega_n \Delta} + e^{-\omega_n(\Delta+\delta)}) \right] \quad (3.16)$$

$$B = 2\gamma^2 a^2 \sum_{n=1}^{\infty} \frac{S_n}{\omega_n^2} \left[e^{-\omega_n(t_m-\delta)} - 2e^{-\omega_n t_m} + e^{-\omega_n(t_m+\delta)} - 2e^{-\omega_n(\Delta+t_m-\delta)} + 4e^{-\omega_n(\Delta+t_m)} \right. \\ \left. - 2e^{-\omega_n(\Delta+t_m+\delta)} + e^{-\omega_n(2\Delta+t_m-\delta)} - 2e^{-\omega_n(2\Delta+t_m)} + e^{-\omega_n(2\Delta+t_m+\delta)} \right] \quad (3.17)$$

We define $D_n = 2$ in Eq. (3.9) for cylinder compartments in axon model and derive:

- $s_n = \frac{1}{\alpha_n^4 - \alpha_n^2}$; $w_n = \frac{\alpha_n^2 D_i}{a^2}$; α_n are the roots of the derivatives of the first-order Bessel functions satisfying the boundary condition: $J_1'(\alpha_n) = 0$
- $\cos \beta_1 = \mathbf{u} \cdot \mathbf{G}_1 = \sin \theta \cos \phi$ and $\cos \beta_2 = \mathbf{u} \cdot \mathbf{G}_2 = \sin \theta \cos(\phi - \psi)$, where the unit vector $\mathbf{u} = (1, \theta, \phi)$ denotes the arbitrary orientation of the axon in polar coordinates and β_1 and β_2 denote the angles between \mathbf{u} and \mathbf{G}_1 , \mathbf{G}_2 respectively, as illustrated in Figure 3.1b.

3.4.3 Distributed Axon Radii Model

We expand our model to incorporate axon-radius variation including contributions from a distribution of fiber sizes. We adopt a two-parameter gamma distribution, fitted to electron microscopy sections of optic and sciatic nerves [8], to model our axon radius distribution. Equation 3.10 is expanded to:

$$E = (1 - f)E_e + f \sum_n w_n(\alpha, \beta) E_i(a_n) \quad (3.18)$$

where the weights w_n of different axon radii are defined by a normalized two-parameter gamma distribution:

$$w_n(\alpha, \beta) = \frac{P(a_n; \alpha, \beta)}{\sum_n P(a_n; \alpha, \beta)} \quad (3.19)$$

$$P(a_n; \alpha, \beta) = \frac{1}{\beta^\alpha \Gamma(\alpha)} a_n^{\alpha-1} e^{-a_n/\beta} \quad (3.20)$$

where, α is the shape parameter, β is the scale parameter, and the mean axon radius $\bar{a} = \alpha\beta$.

3.5 Model Fitting

In the model fitting procedure, the goal is to extract the microstructural parameters: axon radius a , intra-axonal compartment volume fraction f , axon orientation ($u = (1, \theta, \phi)$) and diffusivity (D_i and D_e) of the intra- and extra-axonal compartments. We based our parameter estimation on the analytical model in Section 3.4. We used two modeling fitting algorithms for the two classes of axon geometric models described in Section 3.3: (1) Bayesian inference using Markov Chain Monte Carlo for axons with uniform distribution, and (2) the Levenberg Marquardt fitting algorithm for axons with gamma distribution.

3.5.1 Bayesian Inference using Markov Chain Monte Carlo

We performed Bayesian inference to estimate the microstructural parameters from our analytical model of axons with uniform radius (Section 3.4). Based on Bayes' theorem, we can derive the posterior distribution $P(\theta|D)$ as follows:

$$P(\theta|D) = \frac{P(\theta)P(D|\theta)}{\int P(\theta)P(D|\theta)d\theta} \quad (3.21)$$

where,

- D is our observed experimental data, which is the measured diffusion signal attenuation E from double-PFG experiments.
- θ are our model parameters, which are the unknown microstructural parameters ($a, f, \theta, \phi, D_i, D_e$) we wish to extract.
- $P(\theta)$ is the prior for the model parameters.
- $P(D|\theta)$ is the likelihood of the model.

Since the denominator of equation 3.21 is not a function of θ , we can write the posterior distribution as:

$$P(\theta|D) \propto P(\theta)P(D|\theta) \quad (3.22)$$

Therefore, the posterior expectation of the model parameters θ is:

$$E[f(\theta)] = \int f(\theta)P(\theta|D)d(\theta) \quad (3.23)$$

We used a Markov Chain Monte Carlo (MCMC) procedure [42] to generate samples from this posterior distribution of the microstructural parameters given the experimental data and parameters. Monte Carlo integration estimates the integral $E[f(\theta)]$ in equation 3.23 by obtaining samples $\theta_t, t = 1, \dots, n$ from the posterior distribution $P(\theta|D)$:

$$E[f(\theta)] \approx \frac{1}{n} \sum_{t=1}^n f(\theta_t) \quad (3.24)$$

We run the Markov chain for n iterations, and discard the samples from the first m iterations (called *burn-in*) to use the remaining samples along with equation 3.24 to estimate of the model parameter expectation as follows:

$$E[f(\theta)] \approx \frac{1}{n-m} \sum_{t=m+1}^n f(\theta_t) \quad (3.25)$$

We used a Gaussian distribution $N(\theta|\mu, \sigma)$ based on [103] with standard deviations σ chosen with respect to the difference between our predicted signal E_{model} from the analytical model (Section 3.4) and observed experimental data (diffusion signal attenuation E_{exp} from double-PFG experiments) as our likelihood $P(D|\theta)$. We used a uninformative gamma prior for axon radius a , a beta prior for volume fraction f , and broad uniform priors for axon orientation parameters (θ and ϕ) and diffusivity (D_i and D_e). We ran MCMC with 10 sets of initial values for various parameters to ensure convergence. The burn-in period is 10,000 iterations. We gathered 1,000 independent samples from the marginal posterior distribution of the model parameters as our estimates for the microstructural parameters ($a, f, \theta, \phi, D_i, D_e$). The estimation procedure was implemented in MATLAB $\text{\textcircled{R}}$ (R2009a, MathWorks, Natick, MA) and openBUGS [63] on a Linux operating system. The procedure takes about 4-6 hours for each diffusion image voxel.

3.5.2 Levenberg-Marquardt Fitting

To improve the running time of our method on axon models of distributed radii, we used a Levenberg-Marquardt fitting algorithm [64] to estimate the microstructural parameters. The Levenberg-Marquardt algorithm is a standard method for determining the parameters of nonlinear functions in least-squares problems. The analytical model to be fitted from double-PFG experiments for diffusion signal attenuation is $Y = Y(x|\theta)$, where x is the known experimental parameters in MRI experiments and θ is the unknown axon

parameters we wish to estimate. Therefore, we can compute a χ^2 merit function as: $\chi^2(\theta) = \sum_{i=0}^{N-1} \left[\frac{Y_i - Y(x_i|\theta)}{\sigma_i} \right]^2$, where Y_i denotes the diffusion signal attenuation from double-PFG experiments with experimental parameter set x_i and σ_i denoting the standard deviation. The Levenberg-Marquardt estimation procedure was implemented in MATLAB[®] (R2009a, MathWorks, Natick, MA) on the Linux and Windows operating systems.

3.6 Simulation-based Validation

3.6.1 Data Synthesis

We performed several simulation experiments in order to estimate the underlying axonal properties and validate our analytical model. The benefit of using simulation data is that the ground truth about the axonal properties is known and controllable. Our simulation data for double-PFG experiments was derived from the Monte Carlo simulation for 160,000 spins in the restrictive geometric model described above using Camino [31, 44]. The double-PFG sequence is simulated directly over the diffusive dynamics using the generalized gradient waveform simulation method with a variety of scan parameters [36]. The geometric environment in the simulation was the same as in the tissue geometric model discussed in Section 3.3.

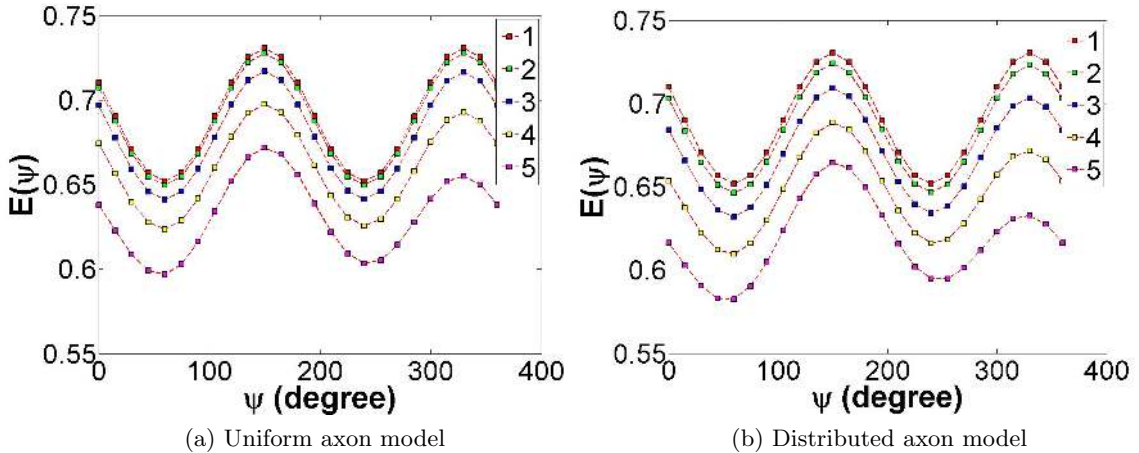


Figure 3.3: Signal attenuation from experimental simulation data (without noise) vs. angle ψ between gradient pairs G_1 and G_2 that varied linearly by 15 degrees. We illustrate the angular dependency difference and signal separation between different axon size and distribution from two geometric models: (a) axons modeled with uniform radius 1 – 5 μm and (b) axons modeled with five gamma distributions (narrow and broad) centered at mean radius 1 – 5 μm .

3.6.2 MRI Experiment Design

We define an unknown arbitrarily oriented unit vector in polar coordinates $\mathbf{u} = (1, \theta, \phi)$ for the coherent axon orientation. We keep the first gradient pair, G_1 , aligned on the x-axis and vary the second gradient pair, G_2 , in the xy-plane by changing the angle ψ between G_1 and G_2 while keeping their magnitude constant. β_1 and β_2 denote the angles between the axon orientation \mathbf{u} and G_1 , G_2 respectively. Experiments were performed with the following parameters: $q = 178.88 \text{ cm}^{-1}$, diffusion gradients $G_{1max} = G_{2max} = 0.07 \text{ T/m}$, pulse duration $\delta_1 = \delta_2 = 6 \text{ ms}$, diffusion time $\Delta_1 = \Delta_2 = 25 \text{ ms}$, mixing time $t_m = 8 \text{ ms}$; ψ was varied in 15° increments.

These experiments were repeated for three sets of data, (1) uniform axon radius in the human brain range $a = (1, 2, 3, 4, 5) \mu\text{m}$ [38], (2) distributed axon radii matching histograms from five regions along the CC [2], and (3) distributed axon radii centered at the human brain range $\bar{a} = (1 - 5) \mu\text{m}$, in order to demonstrate the estimation of various axon distribution (narrow and broad) populations.

The signal attenuation from simulation data (without noise) vs. ψ angle between G_1 and G_2 gradient pairs demonstrates the separate angular dependency of signal attenuation between various axon size and distributions. Figure 3.3a shows the signal from axons modeled with uniform radii ranging from 1 to 5 μm . The smaller signal difference (t-test p-value = 0.440) between axons of 1 and 2 μm versus larger axons (p-value = 0.012 for signal between axons of 3 and 4 μm) demonstrates the challenge in estimating small axons as discussed earlier. Figure 3.3b shows the signal from axons modeled with five gamma distribution (narrow and broad) centered at mean radius of 1 – 5 μm . We again observe a consistent difference in the signal attenuation. This confirms that the signals from angular double-PFG experiments set apart the different distributions and sizes of axon radii.

3.6.3 Axons with Uniform Radius

Table 3.1 and Figure 3.4 show our main results from simulation data for axons with uniform radius in the human brain range $a = (1, 2, 3, 4, 5) \mu\text{m}$ [38]. The data was simulated using the following axon parameters (which we later try to recover): axon orientation $\mathbf{u} = (1, 30^\circ, 60^\circ)$; intra-axonal volume fraction $f = 0.7$; the diffusivity of the intra- and extra-axonal compartments is $D = 2e^{-9} \text{ m}^2/\text{s}$; Rician noise was added to reach a signal-to-noise (SNR) ratio of 30 with no diffusion weighting.

Table 3.1 summarizes our estimated *mean* and standard deviation (*std*) values for axon radius a , orientation θ and ϕ , intra-axonal volume fraction f , and diffusivity D . The *mean*

Axon Radius (μm)		Axon Orientation (rad)		Volume Fraction	Diffusivity $1e^{-9}(m^2/s)$
Ground truth	Estimate	$\theta = 0.5236 = 30^\circ$	$\phi = 1.0472 = 60^\circ$	$f = 0.7$	$D = 2$
1	0.754±0.084	0.507±0.005	1.068±0.005	0.716±0.004	2.170±0.013
2	1.757±0.082	0.512±0.005	1.037±0.013	0.724±0.007	2.074±0.027
3	2.943±0.107	0.519±0.004	1.087±0.013	0.705±0.002	2.115±0.037
4	3.983±0.067	0.493±0.003	1.039±0.005	0.838±0.007	2.071±0.049
5	5.004±0.049	0.490±0.002	1.013±0.003	0.741±0.008	1.945±0.019

Table 3.1: Summary of estimated mean values of axon parameters from the model with uniform axon radius. Ground truth from simulation is: (a) Axon radii $a = (1, 2, 3, 4, 5) \mu m$; (b) Axon orientation; $\mathbf{u} = (1, 30^\circ, 60^\circ) = (1, \frac{\pi}{6}, \frac{\pi}{3})$; (c) Intra-axonal volume fraction $f = 0.7$; (d) Diffusivity $D = 2e^{-9} m^2/s$.

and std were calculated by averaging 100,000 samples drawn from the marginal posterior distribution of the MCMC (Section 3.5.1). Figure 3.4 shows the histogram of axon parameter estimate packing density: a, θ, ϕ, f, D for each of the various true $a = (1, 2, 3, 4, 5) \mu m$ using MCMC. For comparison, the orange vertical lines in Figure 3.4b-3.4e show the true values of the corresponding axon parameters from simulation data.

We observed a slight underestimation for axons with radius less than $3 \mu m$, $a = (1, 2) \mu m$; this was also observed in [54, 55] when the SGP limits were not met using Mitra’s theory [68]. It is important, however, to note that these two small axon radii recovered could still be distinguished regardless of the underestimation. We were able to recover axon radii $a = (3, 4, 5) \mu m$ with high accuracy and averaged $std = 0.0747$. As shown in Table 3.1, the estimated values for θ, ϕ, f and D were in close agreement with their true values with $std = (0.0039, 0.0081, 0.0059, 0.0293)$ respectively. Overall, our estimation results demonstrated the feasibility of recovering axon radii in the range of typical human brain tissue without prior knowledge of axon orientation.

3.6.4 Axons with Distributed Radii

The microstructural parameters of our analytical axon model with distributed radii were recovered using the Levenberg-Marquardt fitting algorithm discussed in Section 3.5.2. Our method was tested with two different datasets: (1) axon distribution matching human CC from histology; and (2) axon distribution representing more complete variation over the entire human brain range ($1 - 5 \mu m$). The two sets of data were simulated using the following axon parameters: axon orientation $\mathbf{u} = (1, 30^\circ, 60^\circ)$; intra-axonal volume fraction $f = 0.7$; diffusivities of the intra- and extra-axonal compartments are $D_i = 1.7e^{-9} m^2/s$ and $D_e = 3e^{-9} m^2/s$ respectively; Rician noise was added to reach a signal-to-noise (SNR) ratio of 30 with no diffusion weighting. Throughout the fitting process, we kept the extra-axonal

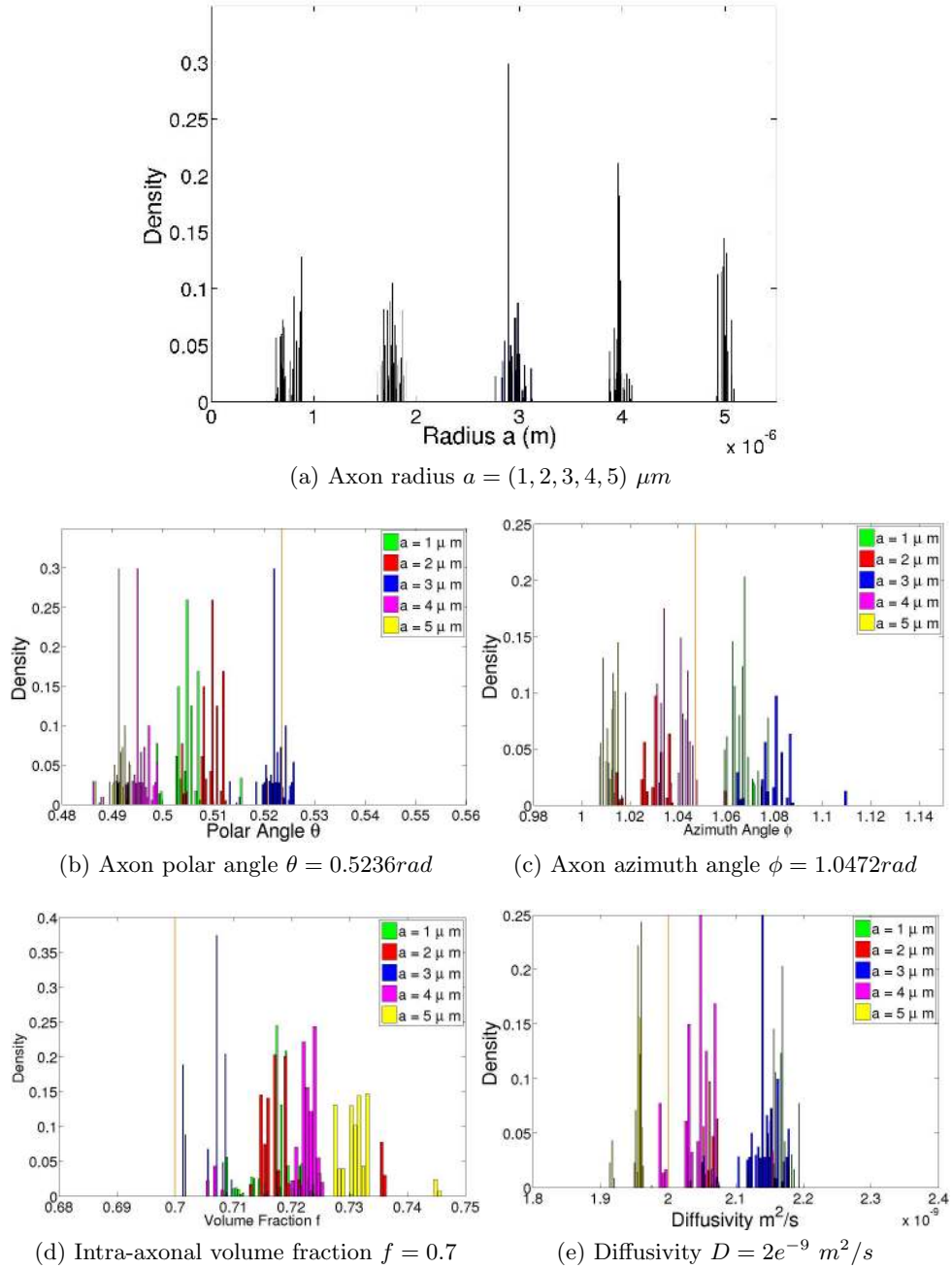


Figure 3.4: Histograms of 10,000 samples drawn from posterior distributions on (a) axon radius a ; (b-c) axon orientation (θ and ϕ); (d) intra-axonal volume fraction $f = 0.7$; and (e) diffusivity D for each of the various true a values using MCMC. Orange vertical lines show the true values in simulation: $a = (1, 2, 3, 4, 5) \mu m$, $\theta = \frac{\pi}{6} rad = 30^\circ$, $\phi = \frac{\pi}{3} rad = 60^\circ$, $f = 0.7$, $D = 2e^{-9} m^2/s$. The *mean* and *std* values of parameter estimates are shown in Table 3.1. Note that some overlapping bars may not be visible in the figure.

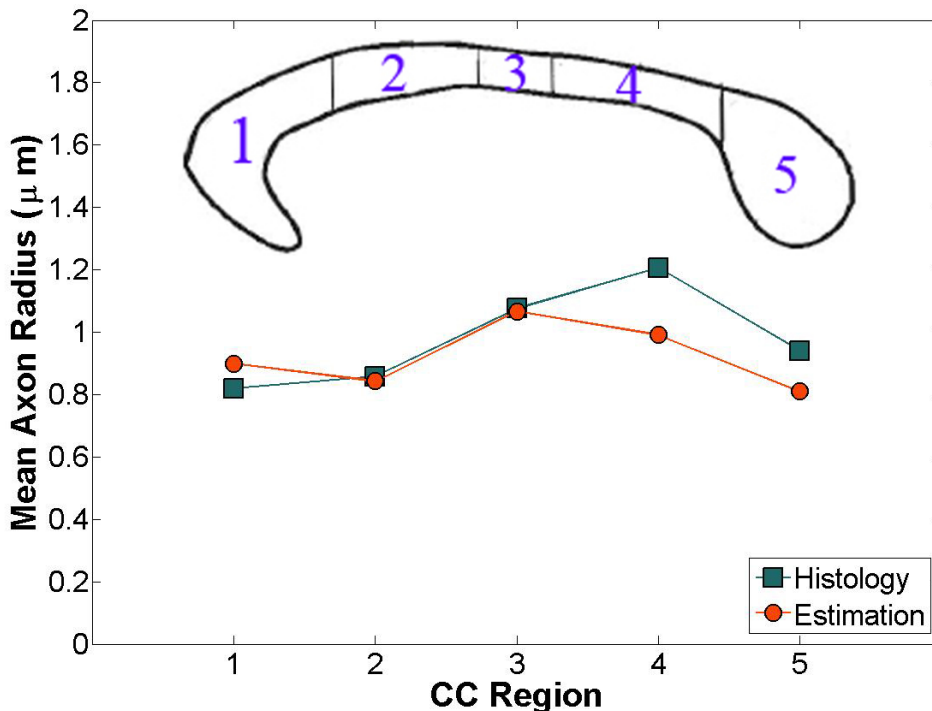


Figure 3.5: Mean axon radius from five regions of the CC: (1) Genu, (2) Anterior body, (3) Midbody, (4) Posterior body, (5) Splenium. The green line shows the ground-truth values computed from histology after a suggested shrinkage correction [2]; the orange line shows our estimated values.

diffusivity constant at $D_e = 3e^{-9} \text{ m}^2/s$.

3.6.4.1 Distribution in Human CC

Figures 3.5-3.7 and Table 3.2 show the main results from simulation data for distributed axons based on the histograms measured in five regions along the human CC from histology [2] and fitted to gamma distribution [5]. We multiply each radius in the histology data by a 1.5 shrinkage factor [2] to correct for the substantial tissue shrinkage produced by fixing and embedding in paraffin. The five regions along the human CC used in the this dataset are (1) Genu, (2) Anterior body, (3) Midbody, (4) Posterior body, and (5) Splenium. Figure 3.6 illustrates the cross sections of the simulated axonal environment at these five regions.

Figure 3.7 shows the axon radius distribution estimation results for each simulation experiment. The green histogram shows the ground-truth distribution of axon radii for each

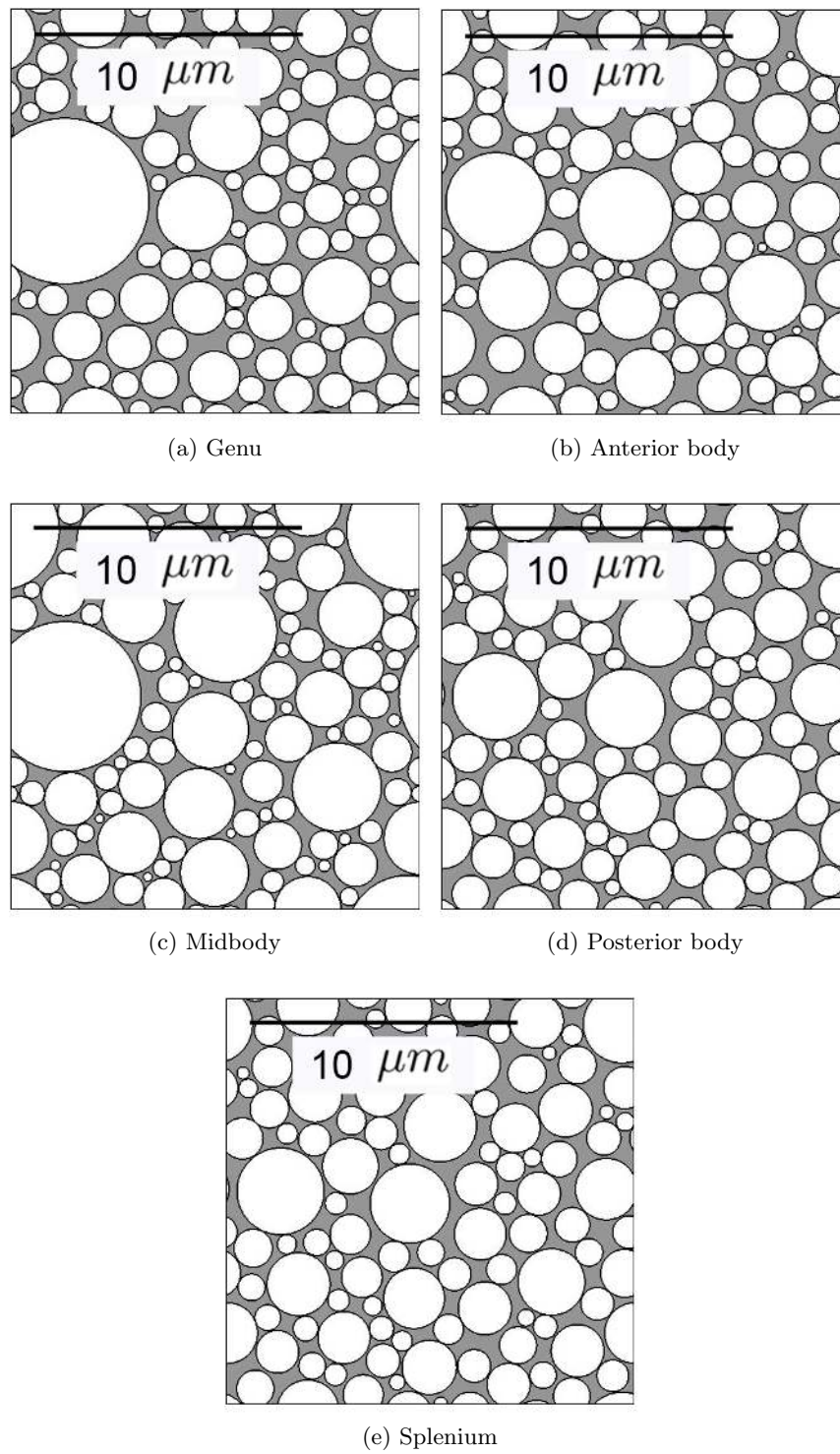


Figure 3.6: Cross sections of the simulated axonal environment at five regions along the human CC from histology [2].

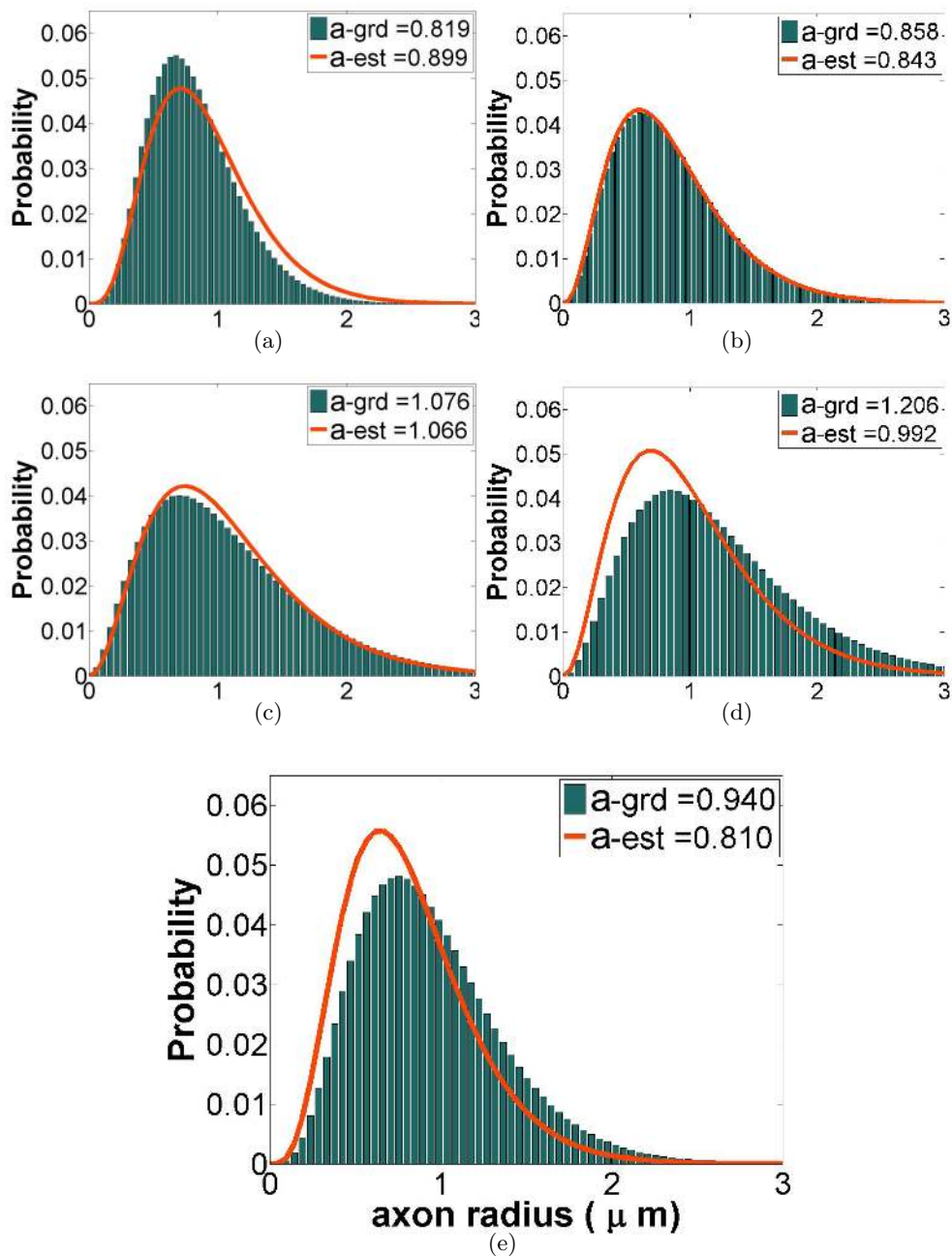


Figure 3.7: *Gamma distribution of axon radii in human CC*: measured at five sites along the CC from histology [2]. The green histogram shows the ground-truth distribution of axon radii with mean radius $a\text{-grd}$. The orange curve shows our fitting results for the estimated gamma distribution of the underlying axon radius distribution with mean radius $a\text{-est}$. The estimated and ground-truth axon radius distributions were highly correlated for all regions along the CC (with correlation coefficients $r > 0.96$). Table 3.2 gives more detailed values of additional estimated axon parameters.

Mean axon radius (μm)		Axon orientation (degree)		Volume fraction	Diffusivity
Ground truth	Estimate	$(\theta, \phi) = (30^\circ, 60^\circ)$	Error	$f = 0.7$	$D_i = 1.7e^{-9}m^2/s$
0.82	0.90	$(24.69^\circ, 59.30^\circ)$	5.33°	0.68	1.67
0.86	0.84	$(18.45^\circ, 60.85^\circ)$	11.57°	0.66	1.65
1.08	1.07	$(19.26^\circ, 68.69^\circ)$	13.31°	0.65	1.55
1.21	0.99	$(21.79^\circ, 67.92^\circ)$	10.86°	0.67	1.60
0.94	0.81	$(22.94^\circ, 62.77^\circ)$	7.48°	0.69	1.67

Table 3.2: **Distribution in human CC**: summary of estimated values of axon parameters. Ground truth from simulation is: (a) mean axon radius $\bar{a} = \alpha\beta = (0.82, 0.86, 1.08, 1.21, 0.94) \mu m$; (b) axon orientation; $\mathbf{u} = (1, 30^\circ, 60^\circ)$; (c) intra-axonal volume fraction $f = 0.7$; (d) Intra-axonal diffusivity $D_i = 1.7e^{-9}m^2/s$; data SNR = 30.

site, and the orange curve shows our fitting results using DoubleAx for estimated gamma-distribution parameters (α and β) describing the underlying axon radius distribution. Each distribution is centered at the estimated mean axon radius $\bar{a} = \alpha\beta$, noted at the upper right corner. As the graph shows, the estimated and ground-truth axon radius distributions were highly correlated for all regions along the CC (correlation coefficients $r > 0.96$) and provide a compelling prediction of the underlying axon radius distribution. Although small axons are dominant in the CC (all mean radii $< 1.1 \mu m$), our method gives an accurate estimate of the mean axon radius that differs from the ground truth by no more than $0.22 \mu m$. We plot and compare these axon mean radii in Figure 3.5 along the five regions of the CC. Note that axon size is smaller in the genu (region 1 and 2) and the splenium (region 5) than in the midbody (region 3 and 4), also known as a low-high-low trend [5]. As Figure 3.5 shows, this low-high-low trend is well preserved in our estimation results.

Table 3.2 summarizes and provides details of the estimated axon parameters including mean axon radius $\bar{a} = \alpha\beta$ from gamma distribution, axon orientation (θ, ϕ) and intra-axonal volume fraction f . Here we also observe a consistent small deviation in estimated axon orientation ($< 14^\circ$) and a slight underestimation of intra-axonal volume fraction ($< 5\%$), similar to observations in the uniform radius model datasets.

3.6.4.2 Distribution in Human Brain Range

Figure 3.9 shows our estimation results from gamma distributions centered at mean radius $1 - 5 \mu m$ in the human brain range with DoubleAx. Since the distributions and the size of the axons ($0.8 - 1.2 \mu m$) along the entire CC do not vary greatly, we use this set of data to demonstrate our accuracy in estimating axons from various gamma distributions (narrow and broad) and a broader spectrum of sizes, including a narrow distribution with a large

Mean axon radius (μm)		Axon orientation (degree)		Volume fraction	Diffusivity
Ground truth	Estimate	$(\theta, \phi) = (30^\circ, 60^\circ)$	Error	$f = 0.7$	$D_i = 1.7e^{-9}m^2/s$
1	0.77	(22.86°, 63.25°)	7.70°	0.67	1.63
2	2.02	(22.14°, 59.09°)	7.89°	0.67	1.65
3	3.01	(23.48°, 57.38°)	6.91°	0.68	1.68
4	3.75	(21.72°, 57.25°)	8.63°	0.67	1.68
5	4.66	(21.98°, 60.68°)	8.04°	0.66	1.60

Table 3.3: ***Distribution in human brain range***: Summary of estimated values of axon parameters. Ground-truth values from simulation are: (a) Mean axon radius $\bar{a} = \alpha\beta = (1, 2, 3, 4, 5) \mu m$; (b) Axon orientation; $\mathbf{u} = (1, 30^\circ, 60^\circ)$; (c) Intra-axonal volume fraction $f = 0.7$; (d) Intra-axonal diffusivity $D_i = 1.7e^{-9}m^2/s$; data SNR = 30.

population of small-radius axons centered at $1 \mu m$ (Figure 3.9a) and a broader distribution of larger axon radii centered at $5 \mu m$ (Figure 3.9e). These axon distributions represent very different axon populations, i.e. small axons in the sensory fibers and large axons in the motor fibers. Figure 3.8 illustrates the cross sections of the simulated axonal environment in the human brain range centered at $1 - 5 \mu m$.

The distribution estimation plot in Figure 3.9 is similar to Figure 3.7 for axons in the CC. The estimated and ground-truth axon radius distributions were again well correlated for all five distributions and sizes (correlation coefficients $r > 0.85$). Our estimated mean axon radius differed from the ground truth by no more than $0.34 \mu m$. As Table 3.3 shows, the axon orientation and intra-axonal volume fraction were also recovered close to the true values: the estimated axon orientation differed from the ground truth by no more than 9° and the volume fraction was under-estimated by less than 4%. It is worth noting that a very similar bias in axon orientation estimation was observed in all three datasets studied. This could have caused the consistent underestimation in intra-axonal volume fraction.

3.6.5 Discussion

Our results show improved accuracy for small axons (radius $< 3 \mu m$), which tend to be more vulnerable to axonal loss in disease, while large-axon fibers remain relatively preserved [41, 62]. Small axons less than $3 \mu m$ are typically more challenging to recover. In previous work using single-PFG sequences, axon radii of 1 and $2 \mu m$ were indistinguishable [4]: that is, while these estimation techniques could say that the axon radii are in the small range ($< 3 \mu m$), they could not differentiate axons of radius about $1 \mu m$ from those of radius about $2 \mu m$. Previous work in double-PFG has not attempted to recover and validate any structure of radius $< 5 \mu m$. The present work clearly distinguishes axons with radius 1 and

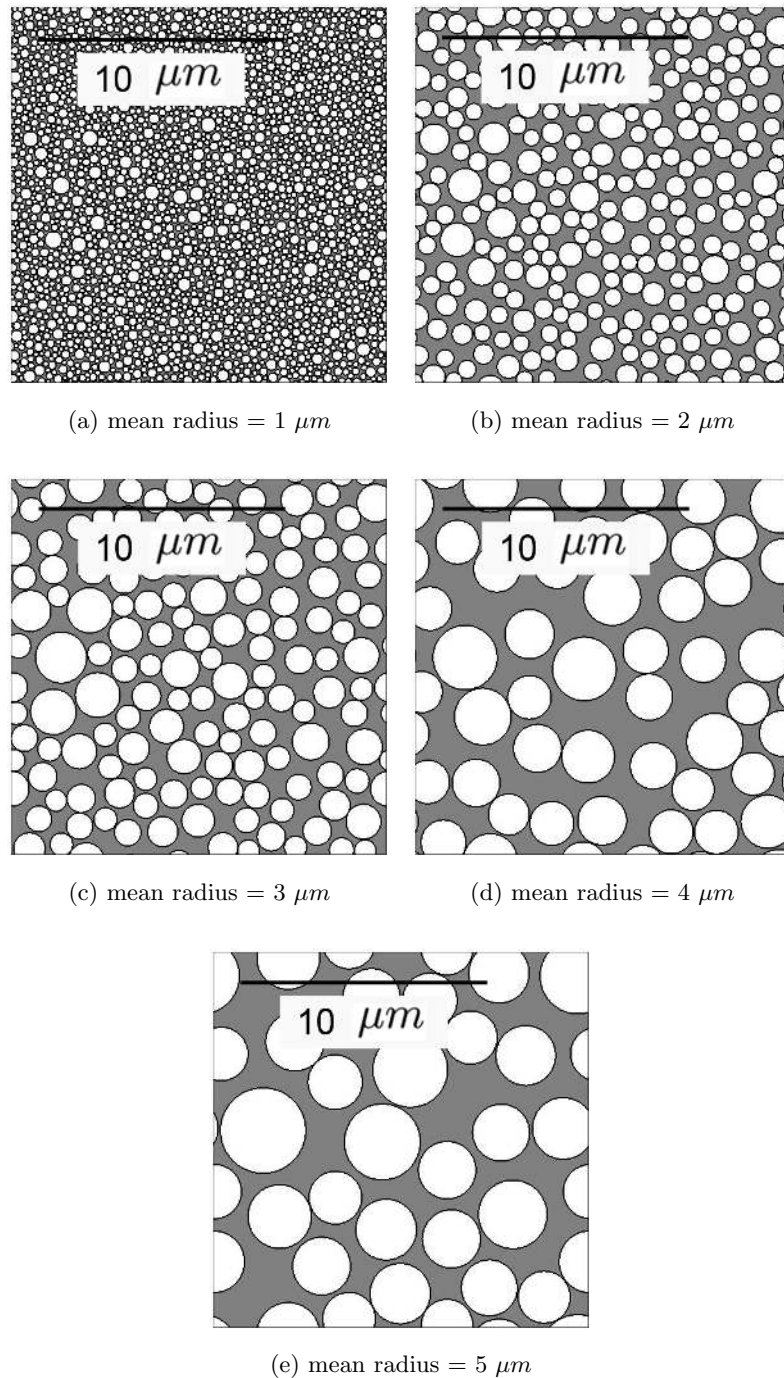


Figure 3.8: Cross sections of the simulated axonal environment in the human brain range centered at $1 - 5 \mu m$. These axon distributions represent various gamma distributions (narrow and broad) and a broader spectrum of sizes in the human brain, including a narrow distribution with a large population of small-radius axons centered at $1 \mu m$ in (a) and a broader distribution of larger axon radii centered at $5 \mu m$ in (e).

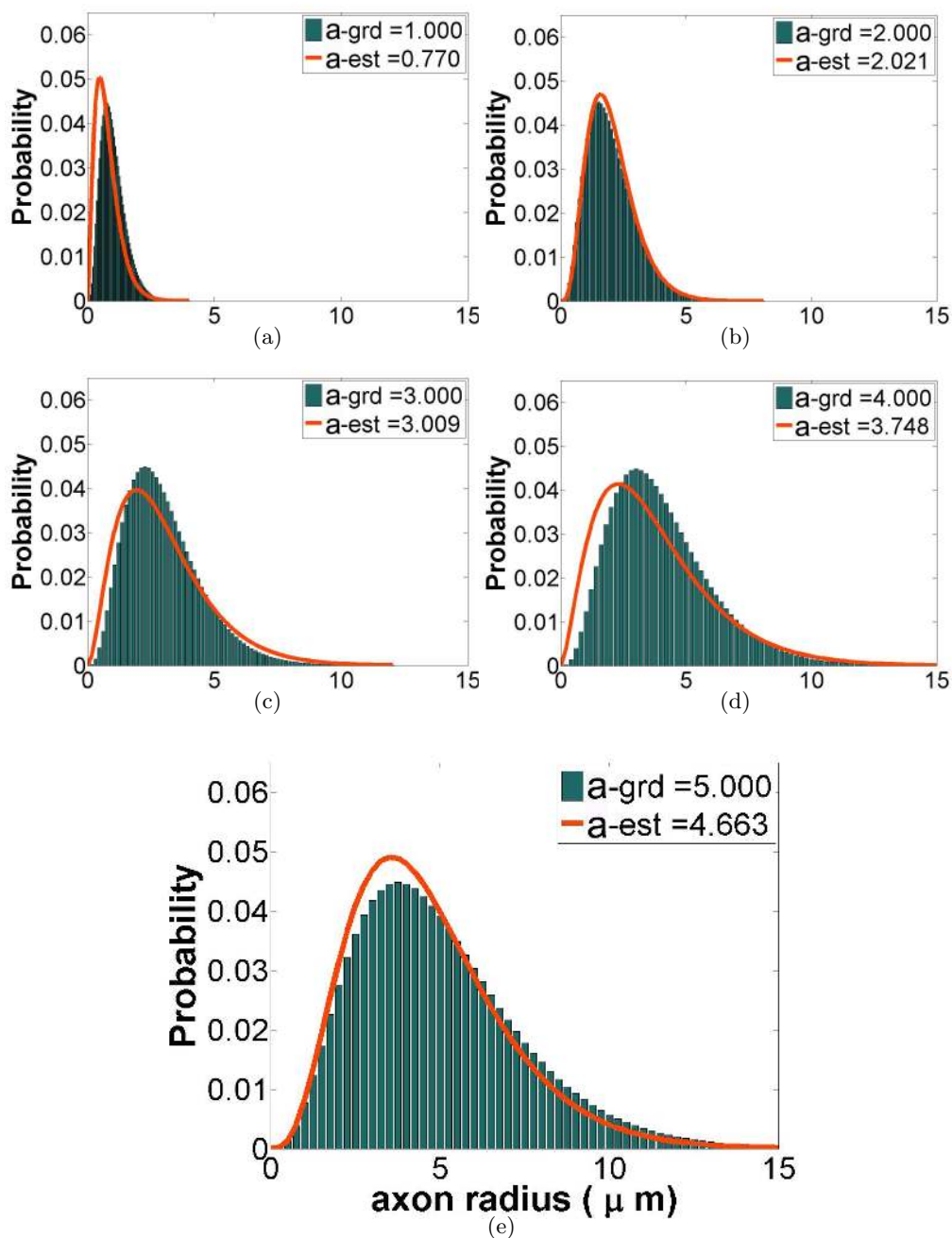


Figure 3.9: *Gamma distribution of axon radii in human brain range.* The green histogram shows the ground-truth distribution of axon radii with mean radius $a\text{-grd}$. The orange curve shows our fitting results for estimated gamma distribution of the underlying axon radius distribution with mean radius $a\text{-est}$. The estimated and ground-truth axon radius distributions again correlated well for all five distributions and sizes (correlation coefficients $r > 0.85$). Table 3.3 gives more detailed values of additional estimated axon parameters.

2 μm using a clinically feasible low gradient.

The experimental parameters used here are all feasible for clinical human scanners with live subjects. These parameters also satisfy the two conditions of double-PFG experiments: the long-diffusion wavelength condition and the diffusion-time condition discussed in Section 3.2. In this chapter, we added synthetic Rician noise to obtain simulation data with SNR of 30 without diffusion weighting in this chapter. We have also tested simulation data with SNR of 40 and 20, obtaining similar results (data not shown). Overall, higher SNR provided greater accuracy in our estimation, similarly to observations in [29].

The intra-axonal volume fraction we estimate from the model is an important parameter relative to axon packing density. It may not, however, directly reflect the density of axons since only relative fractions of the axon compartment are weighted by MRI T1 and T2 relaxation [11]. The volume fraction was the most stable parameter estimated in the model; it was slightly underestimated (by less than 5% in all cases).

The estimation approach presented here requires no prior knowledge of axon orientation. This offers possibilities for mapping of axonal properties in whole-brain tissue. The axon orientation in our model is assumed to be arbitrarily unknown but uniform within a MRI voxel, on the basis of the parallel fibers observed in the midsection of the CC. Our estimated axon orientation deviated from the ground-truth by no more than 14° in all simulated cases. An extension to double-PFG protocol, bipolar double-PFG has been shown to reveal signatures of pore size in randomly oriented cylindrical compartments and provides the potential to overcome this limitation of uniform orientation. It would also be interesting to look into cases of fiber crossing and kissing using a spherical harmonics decomposition of the complex fiber architecture in some regions of the brain. Although simple models like the diffusion tensor can describe the general axon orientation, they cannot be used to estimate important axonal properties such as axon radius and intra-axonal volume fraction because they do not encode restricted diffusion information. In future work, we plan to utilize the general orientation information obtained from the diffusion tensor model as initial condition and bounding constraints in fitting for more accurate parameter estimation in DoubleAx.

Here we adopted a two-parameter gamma distribution to model our axon radius distribution. A gamma distribution has been observed in measurements in electron microscopy sections of optic and sciatic nerves [8]. A non-parametric approach [6], however, might be more appropriate to take into account white matter whose axons are affected by disease such as trauma and ALS.

3.7 Healthy Human Subject Validation

3.7.1 Human Subjects

Two healthy female subjects with no major disease history participated in this study. Subject 1 is age 29 and weighs 118 lb. Subject 2 is age 23 and weighs 110 lb. Both subjects were scanned with informed consent and approval. Two scan sessions were acquired for each subject on two separate days.

3.7.2 MRI Experiment Design

The double-PFG sequence for live human brain imaging was implemented on a Siemens 3T clinical scanner. For each scan session, we acquired 11 sagittal slices covering the entire CC, centered at the midsagittal slice. The slice thickness was 1.8 mm with no gap between slices. The in-plane resolution was 128×128 with $1.8 \times 1.8\text{ mm}^2$ voxels. For each sagittal scan, the first gradient pair G_1 was kept constant in the head-to-toe direction, and the second gradient pair G_2 varied in the sagittal plane in $N = 25$ evenly distributed gradient directions by changing the angle ψ between G_1 and G_2 while keeping their magnitude constant. The protocol includes two $b = 0$ images with each dataset. Together with the 25 diffusion encoded images, we obtained 27 images per slice. Since the sequence was implemented with the basic spin echo sequence rather than the echo-planar sequence, we expect imaging acquisition to take longer than standard MRI scans. It took about 2 minutes to scan each gradient direction and the entire dataset for each scan session took about 55 minutes to acquire. Experiments were performed with the following parameters: diffusion gradients $G_1 = G_2 = 0.035\text{ T/m}$, pulse duration $\delta_1 = \delta_2 = 4\text{ ms}$, diffusion time $\Delta_1 = \Delta_2 = 19\text{ ms}$, mixing time $t_m = 18\text{ ms}$. White matter signal-to-noise ratio (SNR) at $b = 0$ is about 20. The repetition time $TR = 950\text{ ms}$ and echo time $TE = 95\text{ ms}$.

3.7.3 Parameter Estimates

The voxels in the CC were first manually segmented using Osirix [87] as illustrated in Figure 3.10. The CC spans approximately 250 to 300 voxels ($1.8 \times 1.8\text{ mm}^2$) in each dataset depending on the subject. For each voxel, we perform our computational analysis using the Levenberg-Marquardt fitting algorithm described in Section 3.5.2 to estimate the microstructural properties, including: mean axon radius $\bar{a} = \alpha\beta$, volume fraction f , axon orientation $\mathbf{u} = (1, \theta, \phi)$, and intra-axonal diffusivity D_i . Throughout, we kept the extra-axonal diffusivity D_e constant at $1.7 \times 10^{-9}\text{ m}^2/\text{s}$, its expected value for *in-vivo* human

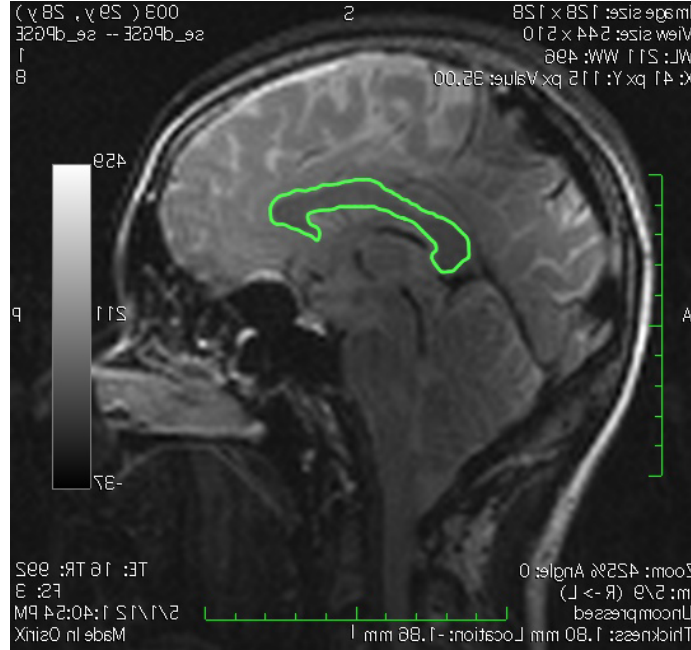


Figure 3.10: Manually segmented CC area from double-PFG data collected from Subject 1 scan 1 using Osirix [87].

data [106].

Estimation Results

Figure 3.11 shows the estimation results in the CC over the midsagittal slice of scan 1 from human subject 1. In the axon radius estimation plot (Figure 3.11a), we can easily observe the bigger axons recovered in the middle (body) versus the smaller axons at the two ends (genu and splenium) of the CC. This matches the expected “low-high-low” anterior-posterior trend in axon radius observed in histology [2] along the CC. Also notice that the extracted axon radius is within the recorded human range 1 to 5 μm [51]. The volume fraction f is in the reasonable range 0.6–0.8 observed in humans [5] (Figure 3.11b). Higher volume fractions, i.e. axons taking up more space within a certain voxel, are mostly found at the two ends of the CC where axon radius is small and axons are densely packed, matching observations in histology [2], as discussed in Section 2.3.1. Since axon fibers are expected to run perpendicularly through the midsagittal slice of the CC, the axon orientation parameter θ is expected to be around 0–10 degrees. The extracted θ is well within the 0–20 degree range. Also, we recover a reasonable estimate of intra-axonal diffusivity in the approximate range $1 \times 10^{-9} \text{ m}^2/\text{s}$ – $2 \times 10^{-9} \text{ m}^2/\text{s}$, as expected in human *in-vivo* data [5].

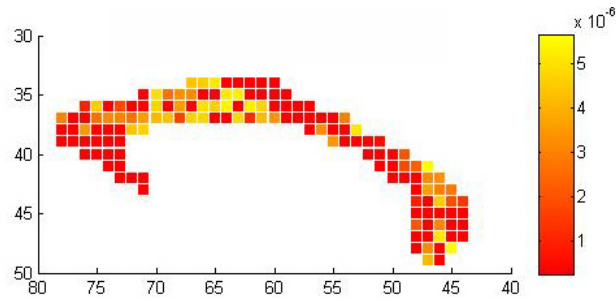
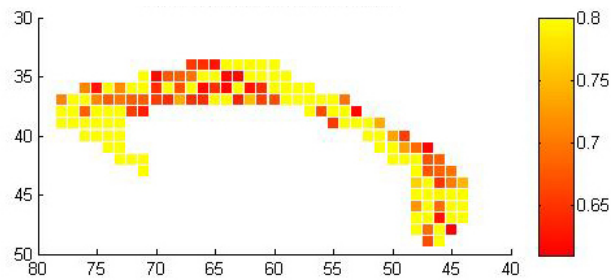
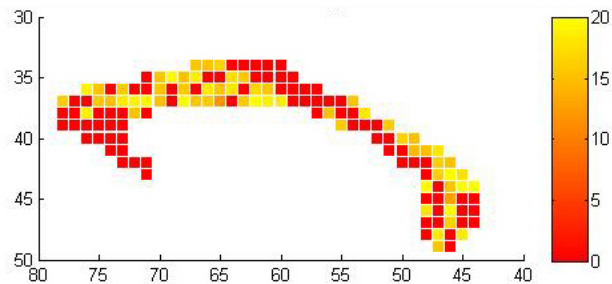
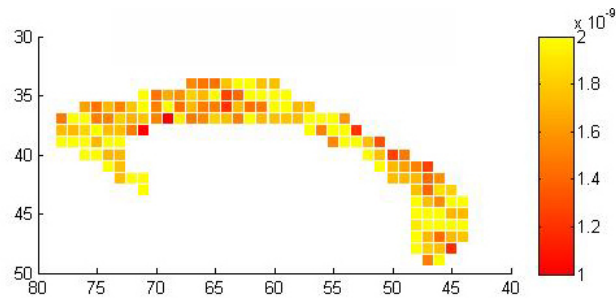
(a) Estimation map of axon radius a (b) Estimation map of volume fraction f (c) Estimation map of axon orientation θ (d) Estimation map of intra-axonal diffusivity D_i

Figure 3.11: Estimation results in the CC from the midsagittal slice of scan 1 from human subject 1, including axon parameters: mean axon radius $\bar{a} = \alpha\beta$, volume fraction f , axon orientation $\mathbf{u} = (1, \theta, \phi)$, and intra-axonal diffusivity D_i .

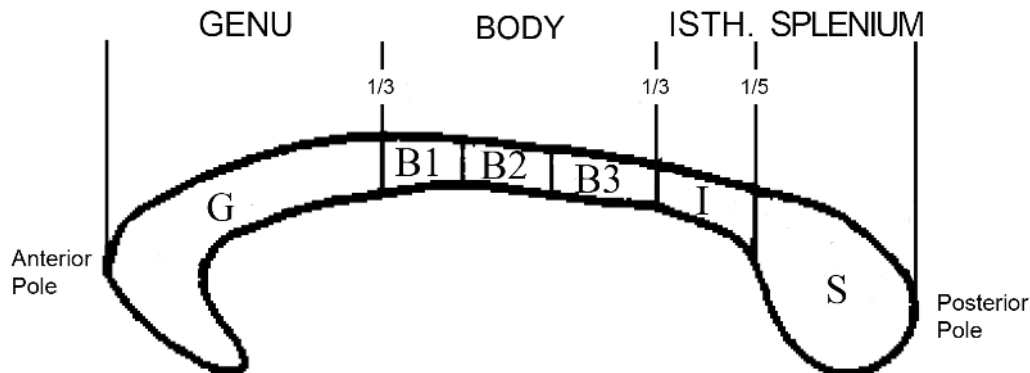
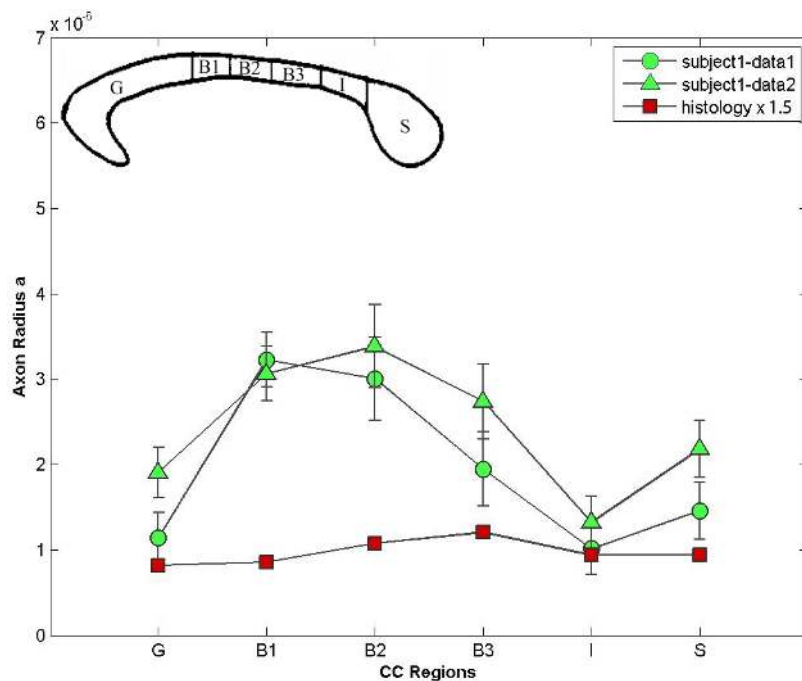


Figure 3.12: Six anatomical segments along the CC used in our histology validation study: (1) genu, (2) anterior body (B1), (3) midbody (B2), (4) posterior body (B3), (5) isthmus, and (6) splenium. Image from [2] (with edits).

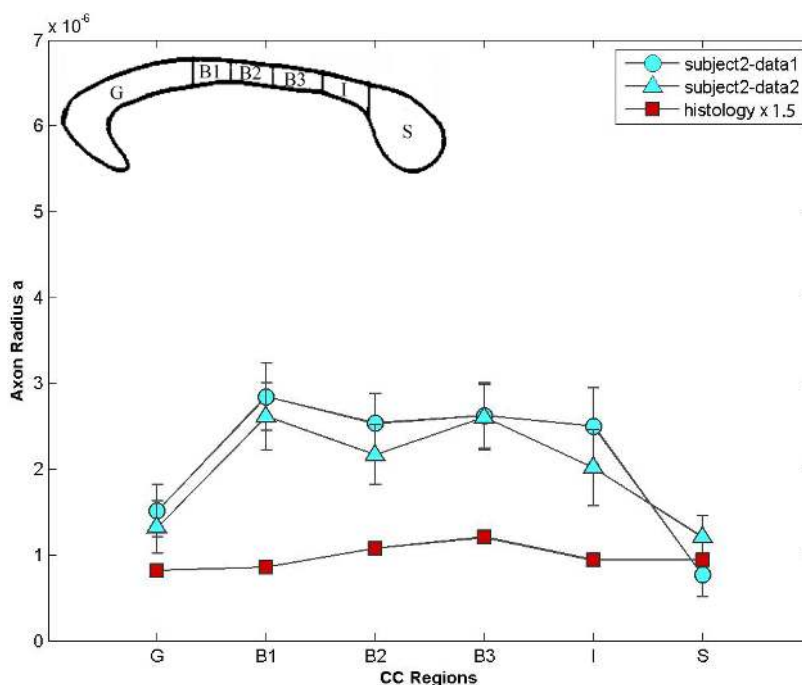
Validation with Histology

For further validation, we compare our estimation results with known axon-radius variation and trends along the CC from histology. First, we divide the CC for each subject into six segments based on anatomical geometry: (1) genu, (2-4) body, (5) isthmus, and (6) splenium. The body section is generally segmented further into three regions, anterior body (B1), midbody (B2), and posterior body (B3). Figure 3.12 illustrates the segmentation scheme we used, matching the six segments along the CC defined in histology [2].

Second, we calculate the average axon radius for each segment along the CC. We plot these average values per segment for the midsagittal slice in Figure 3.13 to illustrate axon-radius variation along the CC for each subject. Figure 3.13a shows results from two scans of Subject 1 and Figure 3.13b shows the results from two scans of Subject 2. We compare these trends with the recorded axon-radius of the same segments from histology [2]. We multiply the axon radius from histology by 1.5 to account for tissue shrinkage during the histology process, as suggested in [2]. Our results demonstrate the consistent “low-high-low” axon-radius trend from anterior to posterior observed in histology data of 20 subjects in the normal population [2]. This pattern is also observed in slices surrounding the midsagittal slice. The estimates from each subject show great consistency across two separate scans and demonstrate the robustness and sensitivity of our method in recovering the axon radius. This consistency within subject is promising for longitudinal study following the same subject for predicting disease progression. Our estimates recovered small axons $\approx 1 \mu m$ mostly in the genu and splenium, and large axons $\approx 3 - 5 \mu m$ in the body of the corpus callosum matching histological measures [1] from 10 female subjects.



(a) Axon radius estimates from Subject 1



(b) Axon radius estimates from Subject 2

Figure 3.13: Comparison of trends in mean axon radius \bar{a} along six anatomical segments of the midsagittal slice of CC for each subject with histological measures from [2]. There are two separate datasets for each subject. We multiply the axon radius from histology by 1.5 to take into account tissue shrinkage during histology.

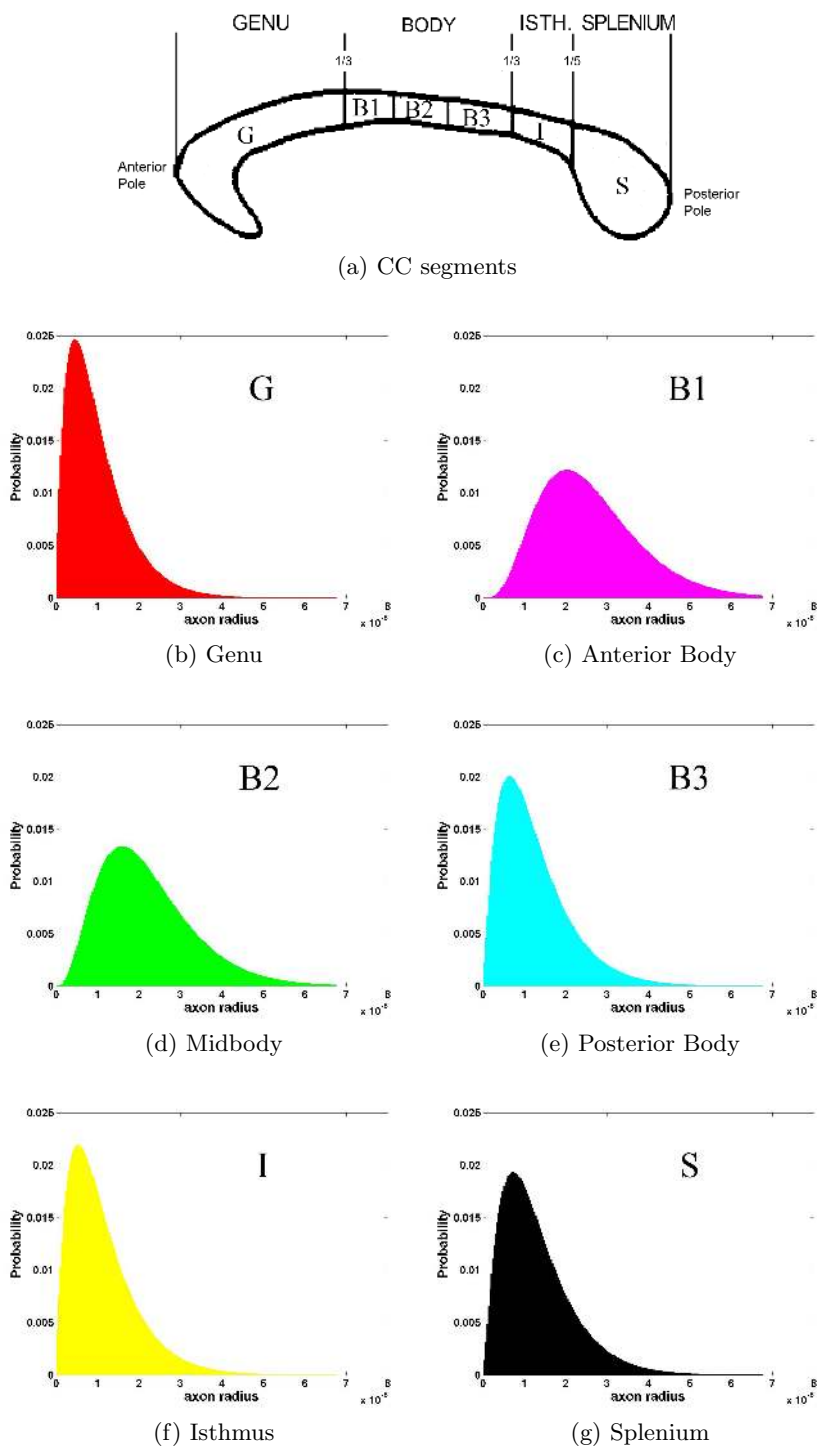


Figure 3.14: Comparison of trends in axon-radius distribution along six anatomical segments of the midsagittal slice of CC from subject 1, scan 1. Our axon-radius distributions show good agreement with histological measures [2, 11]: a narrow distribution in the genu, isthmus, and splenium; and a broader distribution in the body.

As shown in Figure 3.13, the axon radius is consistently larger than histological measures [2] shown by the red line. However, this over-estimation of the axon radius in the body of the corpus callosum was not observed in simulation study discussed in Section 3.6.4.1. The histological measures in Figure 3.13 come from one male individual of age 41 and require caution in interpretation as a gold standard. This single-subject study was chosen for comparison because it provides the most complete histological axon size and distribution information in the literature to date. From the statistics from 20 normal subjects studied in [2], our observed “low-high-low” axon-radius trend is consistently observed in all 20 subjects. Also, our overestimate is consistent with an earlier *in-vivo* human study [5] and with a rat study [11]. Therefore, we hypothesize four main factors in this difference: (1) significant tissue shrinkage resulting from the histology process, (2) difference in ages (our two subjects are age 23 and 29), (3) sex difference (our two subjects are female), and (4) inter-subject variation in axon radius [2]. It is important to note that, although the axon radii were overestimated compared to histology, we show smaller axon radius estimates and better agreement with histology than previous methods, which estimated axon radius well above the largest size observed in humans ($5 \mu m$) [5]. We also observe better consistency in recovered axon radius between scans for each subject (Figure 3.13) than in previous work [5].

Third, we visualize the difference in computed axon-radius distribution for each segment in Figure 3.14. Our axon-radius distribution demonstrates good agreement with histological measures [2, 11]: a narrow distribution in the genu, isthmus, and splenium, and a broader distribution in the body. Earlier *in-vivo* human studies [5, 107] use only a single summary statistic for axon radius which limits the microstructural variation reflected within each brain region. This study provides a more complete model of the whole distribution.

3.7.4 Discussion

The gradient strength used in the experiments $G_1 = G_2 = 0.035 T/m$ was chosen to conform to the clinical limitations for gradient strength used in live human scans. All other experimental parameters (pulse duration δ , diffusion time Δ , mixing time t_m) were chosen to satisfy the two double-PFG experimental parameter conditions discussed in Section 3.2: (1) the long-diffusion-wavelength condition and (2) the diffusion-time condition.

One limitation in the current clinical application is scan time. Due to our current scanner’s software constraints, only the spin-echo sequence was implemented for the double-PFG experiments. The spin-echo sequence significantly prolongs scan time over the more

commonly used echo-planar sequence. However, this timing issue is not intrinsically related to the double-PFG method itself. The imaging time per dataset should be dramatically reduced to about 10 – 15 minutes if the double-PFG is implemented as an echo-planar sequence.

The parameter estimation procedure fixes the extra-axonal diffusivity D_e to the expected value for *in-vivo* human data, which stabilizes the fitting procedure and reduces the number of combinations physically plausible. Our simulations show that fixing the extra-axonal diffusivity does not affect the rest of the parameters recovered. Previous studies fixed intra-axonal diffusivity as well as extra-axonal diffusivity [5, 11]. However, our simulations suggest that fixing intra-axonal diffusivity D_i will affect the accuracy of axon radius estimates.

Last, our validations depend heavily on existing histology information in the literature, which may suffer from differences between subjects. A full same-subject validation would be ideal in order to collect gold-standard measurements of the microstructural properties in real tissue samples. Such a validation study would include the following steps performed on the same subject: (1) live brain scan, (2) postmortem brain scan, and (3) histology on the brain tissue sample (EM images). The computationally obtained microstructural parameters in step (1) and (2) would be validated with the histological measurements obtained in step (3) to achieve a study that is as reliable and complete as possible.

Brain-tissue structure is extremely complex and a geometric model is usually only an approximation of that structure. Panagiotaki [77] provided an extended study identifying the minimum requirements for an accurate model of diffusion MR signal in white matter. Here we used a simple two-compartment impermeable model, one compartment representing the intra-axonal compartment (space within axons) and the other extra-axonal compartment (space outside axons). The current assumption of impermeable axon walls is reasonable for well myelinated axons over the time scale of our measurements [94]. Demyelination and unmyelinated axons, however, do exist in brain diseases like MS and some smaller sensory fiber tracts. We have made some progress in modeling the water exchange at permeable axon walls between compartments in single-PFG [112] (Chapter 4).

3.8 Conclusion

We have demonstrated for the first time that clinically feasible angular double-PFG experiments is sufficient for accurate reconstruction of quantitative measurements of microstructural properties in brain tissue of unknown orientation using DoubleAx. Simulation data lets

us go beyond previous work to provide a reliable approach that aggregates a set of characteristics not previously combined. Our results show improved accuracy for small axons (radius $< 3 \mu m$), which tend to be more vulnerable to axonal loss in disease. Although many angles are required to achieve high-angular double-PFG resolution, these can be collected in considerably less time than multiple high- q single-PFG experiments using current hardware. Our further validation on live human subjects using clinical MRI scanners demonstrates the sensitivity of our approach to human microstructural properties, and also verifies microstructural variations known from histology along the CC across different subjects. Our human study uses a more complete model of the axon-radius distribution than the single summary statistic for axon radius in previous work, which limits the microstructural variation reflected within each brain region. We conclude that inferring axonal properties using double-PFG acquisition may be advantageous in extracting underlying axonal properties to provide reliable and sensitive biomarkers for neurological changes, especially in small axons, as it requires lower q -values.

Chapter 4

Water Exchange Analysis Using Single-Pulsed Field Gradient MR

4.1 Introduction and Related Work

Various brain microstructural changes due to neurological diseases, including axon diameter and myelination, have been observed in a number of invasive histological studies [16, 20, 57]. Loss of myelin reduces reduction in tissue viscosity and elasticity, and increases in permeability [58]. These studies indicate an increased rate of water exchange in disease-affected brain tissue that may occur over the timescale of diffusion MRI experiments [61]. Therefore, in these demyelinated cases (i.e. lesions), microstructure permeability is an important quantity to take into account in a diffusion model for neurological diseases.

Stanisz et al. [94] modeled bovine optic nerve tissue as a three-compartment system with partially permeable membranes including ellipsoidal axons, spherical glial cells, and extracellular space. Fitting such a complex model required very high quality measurements, using 800 nuclear magnetic resonance (NMR) spectroscopy measurements rather than MRI. In this chapter, we present a new analytical model of water diffusion and exchange in white matter for estimating axon radii using diffusion MRI. Estimates of direct microstructural features such as axon radii, density, and permeability are important for early disease detection. Our model for white matter has two compartments between which there is an exchange of water molecules. Our analytical formulas examine the derivation of microstructural parameters that affect signal attenuation in diffusion-weighted MR experiments in white matter. The model is fitted to six constant-gradient diffusion-MRI experiments based on Monte-Carlo simulation with gradient strength 200 – 700 (mT/m).

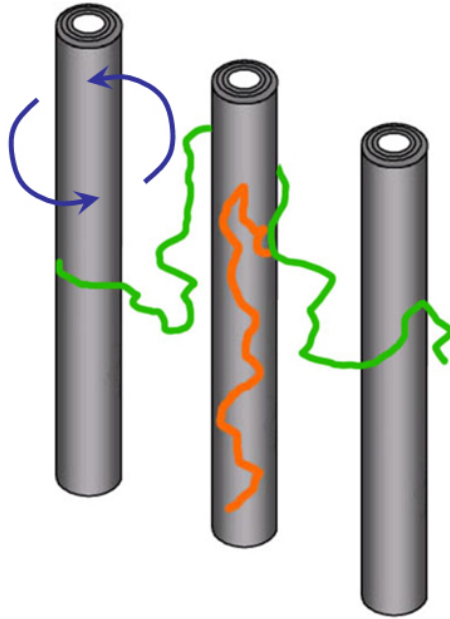


Figure 4.1: Modeling of water diffusion in white matter by two processes: restricted water diffusion within the cylindrical intra-axonal space and hindered water diffusion outside the cylinders in the extra-axonal space.

Our results, based on Monte-Carlo simulation data, demonstrate the feasibility of recovering underlying axon radii of $[1, 1.9, 3, 5, 7] \mu m$ using the model. Axon radii are typically in the range $[0.25 - 10] \mu m$ in brain tissue. Our work is a first attempt at noninvasively recovering microstructural features using a geometric model that incorporates water exchange.

4.2 Tissue Model

4.2.1 Geometric Model

Our model for white matter has two compartments between which there is an exchange of water molecules. The model assumes parallel non-abutting cylindrical axon cells with equal radii and partially permeable membranes embedded in an extra-cellular medium. MR signal attenuation reflects water diffusion in white matter by two processes: restricted water diffusion within the cylindrical intra-axonal space and hindered water diffusion outside the cylinders, in the extra-axonal space (Figure 4.1). We use subscript and superscript 1 and 2 to denote the intra-axonal and extra-axonal compartments, respectively.

4.2.2 Analytical Model

Our model for white matter has two compartments between which there is an exchange of water molecules. The model assumes parallel non-abutting cylindrical axon cells with equal radii and partially permeable membranes embedded in an extra-cellular medium. MR signal attenuation reflects water diffusion in white matter by two processes: restricted water diffusion within the cylindrical intra-axonal space and hindered water diffusion outside the cylinders, in the extra-axonal space (Figure 4.1). We use subscript and superscript 1 and 2 to denote the intra-axonal and extra-axonal compartments, respectively.

The normalized MRI signal is then

$$E(\mathbf{q}, \Delta) = fE_1(\mathbf{q}, \Delta) + (1 - f)E_2(\mathbf{q}, \Delta) \quad (4.1)$$

where

- $E(\mathbf{q}, \Delta)$ is the total observed diffusion signal decay
 - wavenumber $\mathbf{q} = \gamma\delta\mathbf{G}$, γ is the gyromagnetic ratio, δ is the pulse duration, and \mathbf{G} is the applied gradient
 - Δ is the diffusion time between pulses in MRI experiments
- E_1 and E_2 represent the signal decay of water molecules in the intra- and extra-axonal compartments, respectively
- $f \in [0, 1]$ is the volume fraction of the intra-axonal compartments

Sections 4.2.2.1 and 4.2.2.2 below demonstrate how we derive the signal decay of water molecules in the intra- and extra-axonal compartments (E_1 and E_2 respectively). Section 4.2.2.3 summarizes our composite model.

4.2.2.1 Water Diffusion in the Intra-axonal Space

In order to determine how water diffusion affects signal attenuation in diffusion-weighted MR experiments in white matter, we examine the conditional propagator and the conditions in the intra-axonal space that govern the motion of the water molecules.

Propagator for water diffusion

The motion of molecules undergoing diffusion can be described by the conditional propagator, $P_s(\mathbf{r}_0|\mathbf{r}, t)$, an ensemble-averaged probability density for spin displacement from \mathbf{r}_0 to \mathbf{r} over time t . $P_s(\mathbf{r}_0|\mathbf{r}, t)$ obeys:

- The Fick's Law differential equation governing $P_s(\mathbf{r}_0|\mathbf{r}, t)$:

$$\frac{\partial P_s^{(1)}}{\partial t} = D_1 \nabla^2 P_s^{(1)} \quad (4.2)$$

- The initial condition $P_s(\mathbf{r}_0|\mathbf{r}, t)$ for spin displacement from \mathbf{r}_0 to \mathbf{r} over time t :

$$P_s^{(1)}(\mathbf{r}_0|\mathbf{r}, 0) = \delta(\mathbf{r} - \mathbf{r}_0) \quad (4.3)$$

- The boundary condition for partially permeable membranes:

$$D_1 \frac{\partial P_s^{(1)}}{\partial \rho} \Big|_{\rho=a} + M P_s^{(1)} \Big|_{\rho=a} = 0 \quad (4.4)$$

- The boundary relationship of the intra- and extra-cellular compartments:

$$D_1 \frac{\partial P_s^{(1)}}{\partial \rho} \Big|_{\rho=a} = D_2 \frac{\partial P_s^{(2)}}{\partial \rho} \Big|_{\rho=a} \quad (4.5)$$

where D_1 and D_2 are free diffusion coefficients and a is axon radius.

Boundary condition for partially permeable membranes (Equation (4.4))

The boundary condition describes the displacement probability at the membrane. In the partially permeable membrane condition [19], we may confine our consideration to the molecules that do not leave the cylinder [82]. Once they have left, their contribution to the echo signal with increasing field gradient intensities drops to zero as a function of q . Thus, we derive the corresponding boundary condition Equation (4.4), where $M(m/s)$ is the permeability coefficient. Below we shall see that it is convenient to relate the microscopic reduced permeability h of an axon of radius a to the permeability coefficient as:

$$h = \frac{aM}{D_1} \quad (4.6)$$

Boundary relationship of the intra and extra-cellular compartments (Equation (4.5))

The boundary relationship describes the diffusion flux density at two sides of the membrane. The diffusion equation must satisfy both the above boundary condition and the boundary relationship. The Fick's Law diffusion equation (4.2) can be rewritten as:

$$\frac{\partial P_s}{\partial t} = \nabla \cdot (D \cdot \nabla P_s) \quad (4.7)$$

If we define diffusion flux density as

$$\mathbf{j} = -D \cdot \nabla P_s \quad (4.8)$$

Equation (4.7) is then:

$$\frac{\partial P_s}{\partial t} + \nabla \cdot \vec{j} = 0 \quad (4.9)$$

Equation (4.9) is equivalent to the continuity equation in electrodynamics, which implies that the normal component of \mathbf{j} on the boundary should be continuous:

$$\mathbf{n} \cdot (\mathbf{j}_1 - \mathbf{j}_2) = j_{1n} - j_{2n} = 0 \quad (4.10)$$

where \mathbf{j}_1 and \mathbf{j}_2 indicate \mathbf{j} on two sides of the boundary, respectively.

We denote the normal component of \mathbf{j} , j_n . By definition of \mathbf{j} ,

$$j_n = -D \frac{\partial P_s}{\partial n} \Big|_s \quad (4.11)$$

In the cylindrical coordinate system, the outward surface normal \mathbf{n} direction is in the direction along the polar axis direction (i.e. across a diameter). Therefore, we derive our boundary relationship Equation (4.5) from Equations (4.10) and (4.11):

$$D_1 \frac{\partial P_s^{(1)}}{\partial \rho} \Big|_{\rho=a} = D_2 \frac{\partial P_s^{(2)}}{\partial \rho} \Big|_{\rho=a}$$

MRI signal attenuation in the intra-axonal compartment

The diffusion problem posed in Equations (4.2)-(4.5) above may be solved using the standard eigenmode expansion [23]:

$$P_s^{(1)}(\mathbf{r}_0|\mathbf{r}, t) = \sum_{n=0}^{\infty} C_n e^{-\lambda_n t} u_n(\mathbf{r}_0) u_n^*(\mathbf{r}) \quad (4.12)$$

where the $u_n(\mathbf{r})$ are orthonormal sets of solutions to the Helmholtz equation parameterized by the eigenvalue λ_n . Based on our Cauchy boundary condition in Equation (4.4), which specifies a linear combination of the values that a solution of a differential equation can take on the boundary of the domain and the normal derivative at the boundary, the problem is well posed. Given the input and the cylindrical boundary limits to the problem, there exists a unique discrete eigenvalue solution.

We solve the problem in a cylindrical coordinate system in which the longitudinal z axis is a symmetry axis for the system. The relevant coordinates are (ρ, φ) and the gradient is

applied along the polar axis direction (i.e. across a diameter). Equation (4.12) becomes:

$$P_s^{(1)}(\mathbf{r}_0|\mathbf{r}, t) = \sum_{n=0}^{\infty} C_n e^{-\lambda_n t} J_n(k_\rho \rho_0) J_n(k_\rho \rho) e^{in(\varphi - \varphi_0)} \quad (4.13)$$

The permeable membrane boundary is at a radial distance $r = a$ from the cylinder center. For notational convenience, we define the roots k_ρ of the Bessel function J_n as $k_\rho = \frac{\alpha_{nm}}{a}$. Considering our boundary condition Equation (4.4), the eigenfunction expansion for the propagator is then given by:

$$P_s^{(1)}(\mathbf{r}_0|\mathbf{r}, t) = \sum_{n=0}^{\infty} \sum_{m=1}^{\infty} A_{nm}^2 e^{-\frac{\alpha_{nm}^2 D_1 \Delta}{a^2}} J_n\left(\frac{\alpha_{nm}}{a} \rho_0\right) J_n\left(\frac{\alpha_{nm}}{a} \rho\right) \times \cos(n\varphi_0) \cos(n\varphi) \quad (4.14)$$

where J_n are the standard (cylindrical) Bessel functions, while the eigenvalues α_{nm} are determined by the boundary condition Equation (4.4), which is:

$$\frac{\alpha_{nm} J_n'(\alpha_{nm})}{J_n(\alpha_{nm})} = -h \quad (4.15)$$

A_{nm} are normalizing constants:

$$A_{0m}^2 = \frac{1}{\pi a^2} \frac{\alpha_{0m}^2}{J_0^2(\alpha_{0m})(h^2 + \alpha_{0m}^2)} \quad (4.16)$$

$$A_{nm}^2 = \frac{2}{\pi a^2} \frac{\alpha_{nm}^2}{J_n^2(\alpha_{nm})(h^2 + \alpha_{nm}^2 - n^2)}, n \neq 0 \quad (4.17)$$

The derivation of Equation (4.15)-(17) is developed in detail in Appendices A and B.

Finally, we can derive the echo attenuation in Q -space by applying Fourier transformation on the propagator function in X -space Equation (4.14):

$$\begin{aligned} E_1(\mathbf{q}, \Delta) &= \int \int \rho(r, 0) P_s^{(1)}(\mathbf{r}_0|\mathbf{r}, \Delta) e^{i2\pi\vec{q}\cdot(\mathbf{r}-\mathbf{r}_0)} d\vec{r}_0 d\vec{r} \\ &= \sum_{m=1}^{\infty} 4e^{-\frac{\alpha_{0m}^2 D_1 \Delta}{a^2}} \frac{\alpha_{0m}^2}{h^2 + \alpha_{0m}^2} \frac{[2\pi qa J_0'(2\pi qa) + h J_0(2\pi qa)]^2}{[(2\pi qa)^2 - \alpha_{0m}^2]^2} \\ &\quad + \sum_{n=1}^{\infty} \sum_{m=1}^{\infty} 8e^{-\frac{\alpha_{nm}^2 D_1 \Delta}{a^2}} \frac{\alpha_{nm}^2}{h^2 + \alpha_{nm}^2 - n^2} \\ &\quad \times \frac{[2\pi qa J_n'(2\pi qa) + h J_n(2\pi qa)]^2}{[(2\pi qa)^2 - \alpha_{nm}^2]^2} \end{aligned} \quad (4.18)$$

In a typical experiment, only the lowest eigenvalue $\alpha = \alpha_{01}$ is important [82]. Thus, for the purpose of measuring the axon radii, we can simplify the echo attenuation equation, (4.18), and Equation (4.15) becomes:

$$\frac{\alpha_{01} J_0'(\alpha_{01})}{J_0(\alpha_{01})} = -h \quad (4.19)$$

According to the Bessel function, $J'_n(x) = (\frac{n}{x})J_n(x) - J_{n+1}(x)$, we can derive $J'_0(x) = -J_1(x)$. Therefore, our final derivation of the boundary condition is:

$$\frac{\alpha_{01} J_1(\alpha_{01})}{J_0(\alpha_{01})} = h \quad (4.20)$$

We can approximate $\frac{\alpha_{01}^2}{h^2 + \alpha_{01}^2} = 1$ similarly. Our final simplified MRI signal attenuation in the intra-axonal compartment is:

$$E_1(\mathbf{q}, \Delta) = 4e^{-\frac{\alpha_{01}^2 D_1 \Delta}{a^2}} \frac{[h J_0(2\pi qa) - 2\pi qa J_1(2\pi qa)]^2}{[(2\pi qa)^2 - \alpha_{01}^2]^2} \quad (4.21)$$

where a is axon radius and all other parameters have the meanings above.

4.2.2.2 Water Diffusion in the Extra-axonal Space

By applying a Fourier transformation on the Fick's Law differential equation (4.2) governing $P_s(\mathbf{r}_0|\mathbf{r}, t)$ in X -space, we can derive differential equations describing echo signal intensities in Q -space:

$$\frac{\partial E(\mathbf{q}, t)}{\partial t} = -q^2 D E(\mathbf{q}, t) \quad (4.22)$$

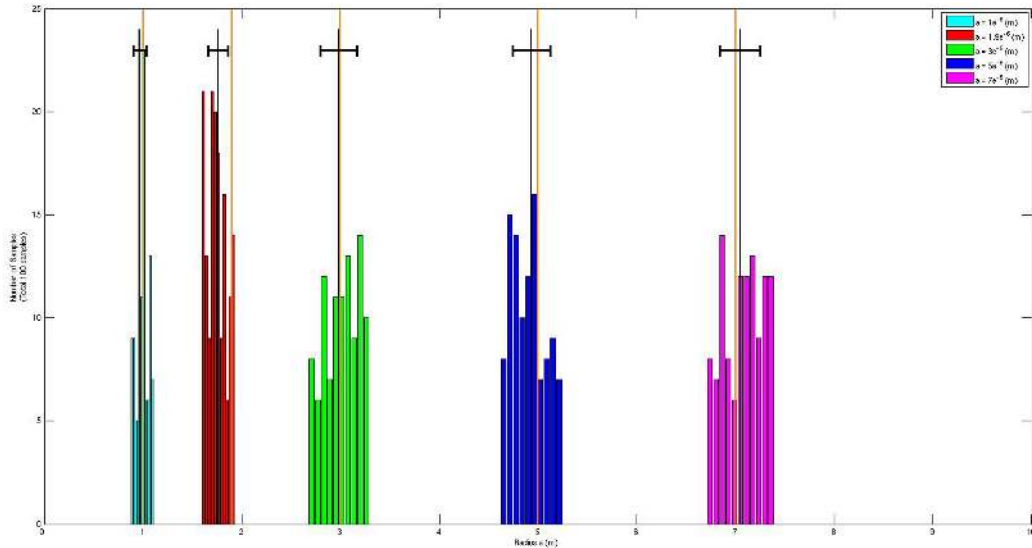


Figure 4.2: Histogram of 100 samples drawn from posterior distribution on radii $a = [1, 1.9, 3, 5, 7] \mu m$ using MCMC; orange lines indicate the true value of various radii; black lines indicate the mean value of each estimate with error bars showing standard deviation. The model was fitted to six constant-gradient diffusion-MRI experiments based on Monte-Carlo simulation with gradient strength 200 – 700 (mT/m). The results demonstrate the feasibility of recovering underlying axon radii using the model.

The solution to the equation has the form $E(\mathbf{q}, t) = E_0 e^{-q^2 D t}$. Therefore, we model the hindered diffusion surrounding the axons with a Gaussian distribution. By assuming a large exchange time τ , $q^2 \tau D_2 \gg 1$, the apparent diffusion coefficient of the extra-axonal compartment can be approximated as $D_{2app} = D_2 + \frac{1}{q^2 \tau}$ [66]. The MRI signal attenuation in the extra-axonal compartment is then:

$$E_2(\mathbf{q}, \Delta) = e^{-q^2 D_2 \Delta + \frac{\Delta}{\tau}} \quad (4.23)$$

4.2.2.3 Composite Model for Water Diffusion in Axonal Space

In summary, referring to Equations (4.1), (4.21), and (4.23), our composite model for normalized MRI signals from water diffusion in axonal space is:

$$\begin{aligned} E(\mathbf{q}, \Delta) &= f E_1(\mathbf{q}, \Delta) + (1 - f) E_2(\mathbf{q}, \Delta) \\ &= f \left(4e^{-\frac{\alpha_{01}^2 D_1 \Delta}{a^2}} \frac{[h J_0(2\pi q a) - 2\pi q a J_1(2\pi q a)]^2}{[(2\pi q a)^2 - \alpha_{01}^2]^2} \right) \\ &\quad + (1 - f) \left(e^{-q^2 D_2 \Delta + \frac{\Delta}{\tau}} \right) \end{aligned} \quad (4.24)$$

with boundary condition

$$\frac{\alpha_{01} J_1(\alpha_{01})}{J_0(\alpha_{01})} = h \quad (4.25)$$

where

- J_n are the standard (cylindrical) Bessel functions and the eigenvalues α_{nm} are determined by the boundary condition Equation (4.15)
- the experimental parameters are:
 - The wavenumber $\mathbf{q} = \gamma \delta \mathbf{G}$, γ is the gyromagnetic ratio, δ is the pulse duration, and \mathbf{G} is the applied gradient
 - The time between pulses in MRI experiments is Δ
- The microstructural parameters are:
 - The axon radius, a
 - The volume fraction of the intra-axonal compartment, $f \in [0, 1]$
 - The free diffusion coefficients of the intra- and extra-axonal compartments respectively, D_1 and D_2
 - The permeability $h = \frac{M a}{D}$ in the intra-axonal compartment; M is the permeability coefficient
 - The exchange time in the extra-axonal compartments, τ

4.3 Datasets

In order to estimate the underlying microstructural parameters and validate our model, we performed several experiments using simulation data. The benefit of using simulation data is that the ground truth about the microstructural parameters is known and controllable.

Our diffusion MRI simulation data were derived from Monte Carlo simulation of the geometric model with rectangular arrangement of cylinders using CAMINO [45]. Our model was fitted to six constant-gradient experiments with the following microstructural parameters: various cylindrical radii: $a = [1, 1.9, 3, 5, 7] \mu m$; exchange rate $\tau = 0.6 (s)$; the free diffusion coefficients of the intra-axonal and extra-axonal water were assumed to be the same, $D = 2e^{-9} m^2/s$; and the intra-axonal volume fraction $f = 0.708$. We set our experimental parameters to be: $\delta = 2 (ms)$; diffusion time was chosen from 20 to 1060 (ms) with 14 linear increments; diffusion gradients were applied only perpendicular to the axon axis (i.e. across a diameter) and each simulation was repeated for six linear gradient amplitudes of 200 – 700 (mT/m) with $SNR = 16$.

4.4 Results

We used a Markov Chain Monte Carlo (MCMC) procedure (see Section 3.5.1 for details) to get samples of the posterior distribution of the model parameters given the data. We used broad uniform priors for all the scalar model parameters. Our proposed distributions were Gaussian with standard deviations chosen manually to give suitable acceptance rates. We initialized parameters to the true value to speed up convergence. The MCMC was run for 10,000 iterations, which yields approximately 100 independent samples from the marginal posterior distribution of model parameters.

Figures 4.2 and 4.3 show our main results. Each histogram combines a total number of 100 samples from MCMC runs. Figure 4.2 shows the histogram of the marginal posterior distribution on radii a for each of the various true $a = [1, 1.9, 3, 5, 7] \mu m$. As mentioned earlier, previous work [4] had much lower accuracy in recovery of smaller radii ($\approx 2 \mu m$) than larger radii. Our study was able to recover radii at about the same variance for both small and large radii ($a = 1e^{-7} - 7e^{-7} \mu m$). Figure 4.3 shows the histogram of the marginal posterior distribution of the other microstructural parameters f (volume fraction), D (free diffusion coefficient) and τ (exchange rate). In previous work [4], there was a downward bias in estimating the free diffusion coefficient D . We were able to recover the diffusion coefficient quite close to the true value. For comparison, the orange lines on the graph

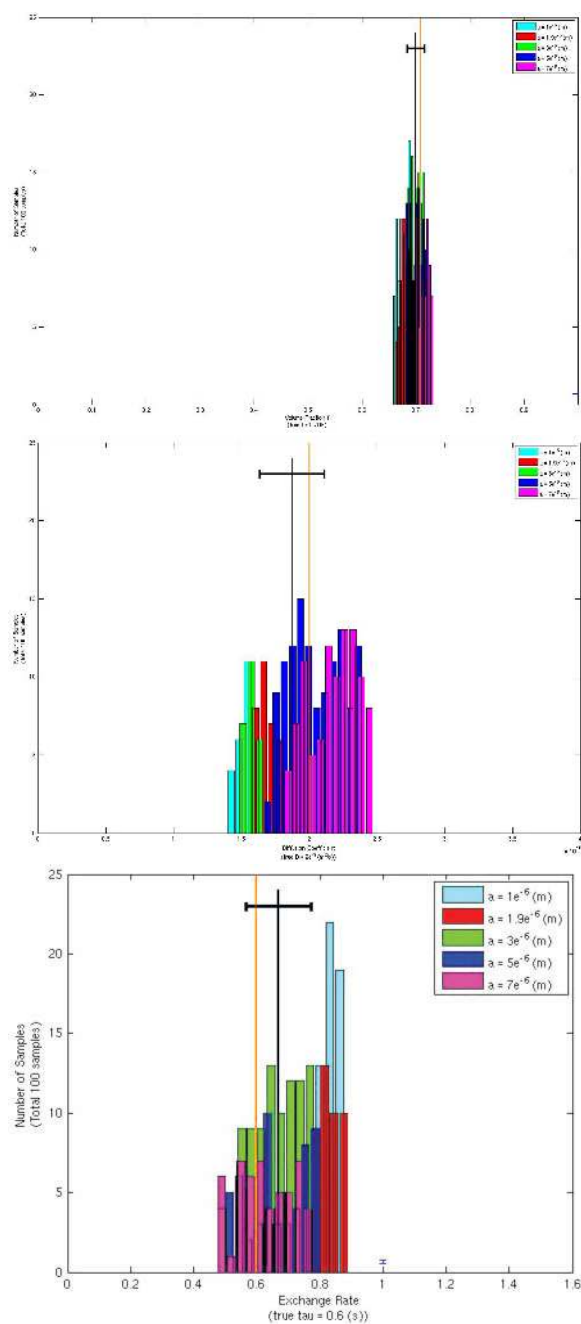


Figure 4.3: Histogram of 100 samples drawn from posterior distributions on volume fraction f , free diffusion coefficient D , and exchange rate τ at various radii: $a = [1, 1.9, 3, 5, 7] \mu\text{m}$ with color coding as in Figure 4.2. The orange lines indicate the true value of $f = 0.708$, $D = 2e^{-9} \text{ m}^2/\text{s}$ and $\tau = 0.6 \text{ (s)}$. The black lines indicate the mean value of each estimate with error bars showing standard deviation. Note that overlapping bars may not show on the figure.

indicate the true value of the corresponding parameters from simulation data. The black vertical lines indicate the mean value of each estimation and their error bar corresponds to standard deviation. Overall, the estimate of the microstructural parameters is accurate and demonstrates the feasibility of recovering underlying axon radii.

4.5 Discussion

We show here that we can recover axon radii and other microstructural features such as volume fraction and diffusion coefficient using our model through a MCMC procedure. This lets us measure anatomical and microstructural features of tissue noninvasively with a more realistic model that integrates water exchange. Direct measurement of axon radii could have a significant impact on our understanding of white matter architecture and connectivity and could improve detection of abnormal development and changes.

Our model is based on two assumptions: (1) water diffusion within axon is restricted, and (2) water molecules exhibit a slow exchange rate. The first assumption, while not proven, is supported by much experimental evidence. It is reasonable to model the intra-axonal compartment of axons as a pack of cylinders containing water. The second condition is also supported by studies that show the exchange rate may be as high as $700ms$ [65].

Currently, a single value per voxel for the axon radius has been assumed for simplicity. This can easily be extended to integrate over a model distribution of axon radii using Gamma distribution as in Section 3.4.3. Also, in the current model, we are assuming a single axon direction per voxel. Again, this could be extended to model the distribution for axon orientation using spherical harmonic decomposition to detect fiber crossing and fiber kissing.

4.6 Conclusion

We present a new composite analytical model of diffusion and exchange of water in white matter using data from diffusion MRI. Our work is a first attempt to estimate microstructural features through diffusion MRI model incorporating water exchange. Our results demonstrate the feasibility of recovering underlying axon radii and other microstructural features such as volume fraction and diffusion coefficient using the model through the MCMC procedure from Monte Carlo simulation data. We were able to achieve higher accuracy in recovering small axon radii ($\approx 2 \mu m$) and diffusion coefficient than in previous work.

Appendices

Appendix A

Solution of the Torrey-Bloch Equation for double-PFG

A.1 Torrey-Bloch Equation with Boundary Condition

Any sample placed under a magnetic field will be magnetized, its magnetization $\vec{M}(\vec{r}, t)$ is followed by decay due to relaxation. In 1956, H.C. Torrey mathematically showed how the Bloch equations for magnetization would change with the addition of diffusion terms and the application of a spatially varying gradient.

- The Torrey-Bloch equation neglecting relaxation is (To unify symbols used in mathematics background Section 2.2, let $\Psi(\vec{r}, t) \equiv M(\vec{r}, t)$):

$$\frac{\partial \Psi}{\partial t} = D \nabla^2 \Psi - i \gamma \vec{G} \cdot \vec{r} \Psi \quad (\text{A.1})$$

- The boundary condition is:

$$\frac{\partial \Psi}{\partial n} = 0 \quad (\text{A.2})$$

- The corresponding signal is

$$E = \int \Psi(\vec{r}, t) d\tau \quad (\text{A.3})$$

where D is the diffusion coefficient, γ is the gyromagnetic ratio, and $\vec{G}(t)$ is the linear magnetic field gradient waveform.

A.2 Solution of the Torrey-Bloch Equation using Green's Function

Since the term $i\gamma\vec{G}\vec{r}\Psi$ in equation (A.1) contains variable Ψ , we must use an iteration method to solve the Torrey-Bloch equation (A.1).

Let

$$\Psi(\vec{r}, t) = e^{\lambda t} \varphi(\vec{r}) \quad (\text{A.4})$$

where $\varphi_m(\vec{r})$ is the eigenfunctions of the eigenequation:

$$D\nabla^2 \varphi_m(\vec{r}) = -\lambda_m \varphi_m(\vec{r}) \quad (\text{A.5})$$

We can expand Ψ using eigenfunctions φ_m

$$\Psi(\vec{r}, t) = \sum_m A_m(t) \varphi_m(\vec{r}) \quad (\text{A.6})$$

Insert equation (A.6) above into equation (A.1), we get:

$$\sum_m \left(-\lambda_m A_m(t) - i\gamma\vec{G} \cdot \vec{r} A_m(t) - \frac{\partial A_m(t)}{\partial t} \right) \varphi_m(\vec{r}) = 0 \quad (\text{A.7})$$

and since

$$\frac{\partial A_m(t)}{\partial t} = -(\lambda_m + i\gamma\vec{G} \cdot \vec{r}) A_m(t) \quad (\text{A.8})$$

we derive:

$$A_m(t) = A_m(0) \exp\left(-(\lambda_m + i\gamma\vec{G} \cdot \vec{r})t\right) \quad (\text{A.9})$$

Insert equation (A.9) above into equation (A.6), we derive:

$$\Psi(\vec{r}, t) = \sum_m A_m(0) \exp\left(-(\lambda_m + i\gamma\vec{G} \cdot \vec{r})t\right) \varphi_m(\vec{r}) \quad (\text{A.10})$$

From equation (A.6) we can derive:

$$A_m(0) = \langle \varphi_m(\vec{r}) | \Psi(\vec{r}, 0) \rangle = \int \varphi_m^*(\vec{r}) \Psi(\vec{r}, 0) d\tau \quad (\text{A.11})$$

Finally, we insert equation (A.11) into equation (A.10), we obtain:

$$\Psi(\vec{r}, t) = \sum_m \int \Psi(\vec{r}t, 0) \varphi_m^*(\vec{r}t) \varphi_m(\vec{r}) \exp\left(-(\lambda_m + i\gamma \vec{G} \cdot \vec{r})t\right) d\tau t \quad (\text{A.12})$$

We define a Green's function:

$$\langle \vec{r}t | G(t) | \vec{r} \rangle = \sum_m \varphi_m^*(\vec{r}t) \varphi_m(\vec{r}) \exp\left(-(\lambda_m + i\gamma \vec{G} \cdot \vec{r})t\right) \quad (\text{A.13})$$

We can rewrite our magnetization equation (A.12) as:

$$\Psi(\vec{r}, t) = \int \langle \vec{r}t | G(t) | \vec{r} \rangle \Psi(\vec{r}t, 0) d\tau t \quad (\text{A.14})$$

Therefore, the signal attenuation from this magnetization is:

$$E = \int \Psi(\vec{r}, t) d\tau = \int \int \langle \vec{r}t | G(t) | \vec{r} \rangle \Psi(\vec{r}t, 0) d\tau t d\tau \quad (\text{A.15})$$

General Solution for double-PFG

According to equation (A.12), in order to solve the Torrey-Bloch equation under certain MRI sequence, we need to know two things:

1. The eigenfunction and eigenvalues of equation (A.5) in certain coordinate system. For example, the coordinate system used in axon analysis is cylindrical coordinate.
2. The magnetic field gradient The magnetic field gradient is the source of Torrey-Bloch equation. The pulse gradients are intermittent, not continuous. We could divide the time intervals into multiple sections, such as $0, t_1, t_2, \dots, t_{n-1}, t_n, \dots, t$. In time interval (t_{n-1}, t_n) , we can rewrite equation (A.9) as:

$$A_m(t_n) = A_m(t_{n-1}) \exp\left(-(\lambda_m + i\gamma \vec{G} \cdot \vec{r})(t_n - t_{n-1})\right) \quad (\text{A.16})$$

Let $t_{n-1} - t_n \equiv \delta_n$, the wave number $q_n = \frac{1}{2\pi} \gamma G \delta_n$, we have:

$$A_m(t_n) = \exp\left(-(\lambda_m \delta_n + i2\pi \vec{q}_n \cdot \vec{r})\right) A_m(t_{n-1}) \quad (\text{A.17})$$

Equation (A.17) is a recurrence equation, it can be rewritten as:

$$A_m(t) = A_m(0) \prod_{n=1}^N \exp\left(-(\lambda_m \delta_n + i2\pi \vec{q}_n \cdot \vec{r})\right) \quad (\text{A.18})$$

and

$$E = \langle 0 | \prod_{n=1}^N \exp\left(-(\lambda_m \delta_n + i2\pi \vec{q}_n \cdot \vec{r})\right) | 0 \rangle^* \quad (\text{A.19})$$

where $|0\rangle$ is basis state of equation (A.9). The magnetic pulse gradients in the double-PFG have seven intervals, with pulse duration δ , diffusion time Δ , mixing time t_m and gradient magnitude G , we derive:

$$E = \langle 0 | e^{-\lambda_m(2\delta+2\Delta+t_m)} e^{8\pi\vec{q}\cdot\vec{r}} | 0 \rangle^* \quad (\text{A.20})$$

Appendix B

Derivation of Boundary Condition

This derivation shows how we formulate the boundary condition, Eq. (15). Based on our general solution to $P_s^{(1)}(\mathbf{r}_0|\mathbf{r}, t)$ in Eq. (13):

$$P_s^{(1)}(\mathbf{r}_0|\mathbf{r}, t) = \sum_{n=0}^{\infty} C_n e^{-\lambda_n t} J_n(k_\rho \rho_0) J_n(k_\rho \rho) e^{in(\varphi - \varphi_0)}$$

we can derive:

$$D_1 \frac{\partial P_s^{(1)}}{\partial \rho} \Big|_{\rho=a} = \sum_{n=0}^{\infty} C_n D_1 e^{-\lambda_n t} J_n(k_\rho \rho_0) J'_n(k_\rho a) k_\rho e^{in(\varphi - \varphi_0)} \quad (\text{B.1})$$

$$M P_s^{(1)} \Big|_{\rho=a} = \sum_{n=0}^{\infty} C_n M e^{-\lambda_n t} J_n(k_\rho \rho_0) J_n(k_\rho a) e^{in(\varphi - \varphi_0)} \quad (\text{B.2})$$

Incorporating Eq. (B.1)-(B.2) into our initial boundary condition for the permeable membrane, Eq. (4):

$$D_1 \frac{\partial P_s^{(1)}}{\partial \rho} \Big|_{\rho=a} + M P_s^{(1)} \Big|_{\rho=a} = 0$$

gives us:

$$\sum_{n=0}^{\infty} C_n e^{-\lambda_n t} J_n(k_\rho \rho_0) [D_1 J'_n(k_\rho a) k_\rho + M J_n(k_\rho a)] e^{in(\varphi - \varphi_0)} = 0 \quad (\text{B.3})$$

which is equivalent to:

$$D_1 J'_n(k_\rho a) k_\rho + M J_n(k_\rho a) = 0 \quad (\text{B.4})$$

The parameters we defined earlier, $k_\rho = \frac{\alpha_{nm}}{a}$ and $h = \frac{aM}{D_1}$, have been integrated into Eq. (B.4). We derive our boundary condition in Eq. (15):

$$\alpha_{nm} J'_n(\alpha_{nm}) + h J_n(\alpha_{nm}) = 0$$

Appendix C

Derivation of Normalizing Constants

Here we demonstrate how we derive the normalizing constants A_{nm} in Eqs. (16)-(17). Based on the orthogonality of Bessel functions, we have:

$$\int_0^a \rho J_n(k_i \rho) J_n(k_j \rho) d\rho = 0 (i \neq j) \quad (\text{C.1})$$

$$= N_i (i = j)$$

where

$$N_i = \frac{a^2}{2} \left\{ [J'_n(k_i a)]^2 + \left(1 - \frac{n^2}{a^2 k_i^2}\right) J_n^2(k_i a) \right\} \quad (\text{C.2})$$

We define $k_i = \frac{\alpha_{nm}}{a}$ as before and can rewrite Eq. (C.2) as:

$$N_{nm} = \frac{a^2}{2} [J'_n(\alpha_{nm})]^2 + \left(1 - \frac{n^2}{\alpha_{nm}^2}\right) J_n^2(\alpha_{nm}) \quad (\text{C.3})$$

Given our boundary condition Eq. (15): $\alpha_{nm} J'_n(\alpha_{nm}) + h J_n(\alpha_{nm}) = 0$, we can derive:

$$N_{nm} = \frac{a^2}{2} \left(\frac{h^2 + \alpha_{nm}^2 - n^2}{\alpha_{nm}^2} \right) J_n^2(\alpha_{nm}) \quad (\text{C.4})$$

In order to derive our normalizing constant A_{nm} in Eqs. (16)-(17), we integrate Eq. (14), the propagator, on the cylindrical cross section at time $t = 0$, $\rho = \rho_0$, $\varphi = \varphi_0$ and $P_s^{(1)} = \delta(\mathbf{r} - \mathbf{r}_0)$:

$$\int \int P_s^{(1)} ds = 1 \quad (\text{C.5})$$

Therefore, we have:

$$A_{nm}^2 \int_{\rho=0}^{\rho=a} \int_{\varphi=0}^{\varphi=2\pi} \rho J_n^2\left(\frac{\alpha_{nm}}{a} \rho\right) \cos^2(n\varphi) d\rho d\varphi = 1 \quad (\text{C.6})$$

Given that:

$$\begin{aligned} \int_0^{2\pi} \cos^2(n\varphi) d(\varphi) &= \pi(n \neq 0) \\ &= 2\pi(n = 0) \end{aligned} \tag{C.7}$$

we can derive A_{nm}^2 based on Eq. (C.4) and Eq. (C.7),

$$\begin{aligned} A_{nm}^2 &= \frac{1}{2\pi} \frac{1}{N_n} (n = 0) \\ &= \frac{1}{\pi} \frac{1}{N_n} (n \neq 0) \end{aligned} \tag{C.8}$$

which is equivalent to the following in Eqs. (16)-(17):

$$A_{0m}^2 = \frac{1}{\pi a^2} \frac{\alpha_{0m}^2}{J_0^2(\alpha_{0m})(h^2 + \alpha_{0m}^2)} \tag{C.9}$$

$$A_{nm}^2 = \frac{2}{\pi a^2} \frac{\alpha_{nm}^2}{J_n^2(\alpha_{nm})(h^2 + \alpha_{nm}^2 - n^2)}, n \neq 0 \tag{C.10}$$

Part II

Brain White Matter Anatomical Analysis

Chapter 5

Brain White Matter Visualization: Spatial Relations

5.1 Introduction

Understanding white-matter structures within the human brain is crucial for studying various neurological disorders such as Alzheimer’s disease (AD) and HIV. Diffusion-Tensor Magnetic Resonance Imaging (DTI) estimates the Brownian motion of water in tissues enabling the *in-vivo* exploration of fibrous structures such as white matter in the brain. DTI tractography methods calculate a set of integral curves estimating neural fibers in the brain. These curves are generated by tracking the principal eigenvector of the underlying diffusion tensor field in both directions. They are often visualized with streamlines or variations of streamlines (streamtubes and hyperstreamlines) in 3D.

Densely sampled integral curves tend to be visually cluttered and hinder the exploration of the underlying structures. This limitation highlights the need for better data mining and visualization techniques. In the following chapter, we present two new methods for visualizing integral curves obtained from DTI volumes that encode spatial relations between curves with texture patterns.

5.2 Related Work

A vast amount of work has been done on visualization of DTI data (for a complete review see [101]). Here we only discuss examples of previous work incorporating the spatial relations of DTI integral curves into their visualization. The standard method used for coloring

streamtubes according to spatial relations is to map the normalized absolute values of the x , y , and z components of the vector defined by the end points of the streamtubes, to R, G, and B color values. This method obviously suffers from mirror symmetries [76]. More recently, Brun et al [21] apply the Laplacian eigenmaps algorithm, a spectral embedding method, to embed the end-point distances of integral curves in RGB space.

We build on the body of previous work and present two new visualization techniques: (1) Perceptual coloring - we used a spectral method [27] to embed “anatomically-motivated dissimilarities” between the curves into the $L^*a^*b^*$ color space, which is approximately perceptually uniform, such that each difference between the colors of the curves corresponds to the distance (or dissimilarity) between the curves. (2) Texture Patterns - using non-linear dimensionality reduction techniques, we encode the relations in the low-dimension (i.e., in the embedding plane) with a flexible coloring scheme and texture patterns.

5.3 Visualization Approach A: Perceptual Coloring

5.3.1 Method

We visualize distances between white-matter tracts using the metric in [108]. Our white-matter tract processing is illustrated in the flow chart in Figure 5.1: first, streamtubes that represent white-matter pathways are computed from DT-MRI data. Second, we compute an adjacency matrix of distances between every pair of streamtubes in the brain. Third, using a spectral embedding method, we assign colors to every streamtube such that differences in colors correspond to the distances in the matrix. Finally these colors are converted from a perceptually uniform color space to RGB for display. On a 2K streamtube dataset, the relative error of the embedding measured with the Frobenius norm of the tube embedded distance matrix and the original distance matrix is 13%. We suspect that using a more sophisticated method would yield embeddings with less error. After we’ve assigned a coloring of streamtubes we view them in BrainApp [88], an interactive tool for visualizing DT-MRI data.

5.3.2 Results

We performed two informal evaluations with an neuropsychologist visualizing a normal and an HIV-positive brain data-set shown in figure 5.2. Our expert reported high anatomic specificity, and he reported being able to easily pick out meaningful neural tract bundles even though the colors varied smoothly. He noted that the hemispheric color differences

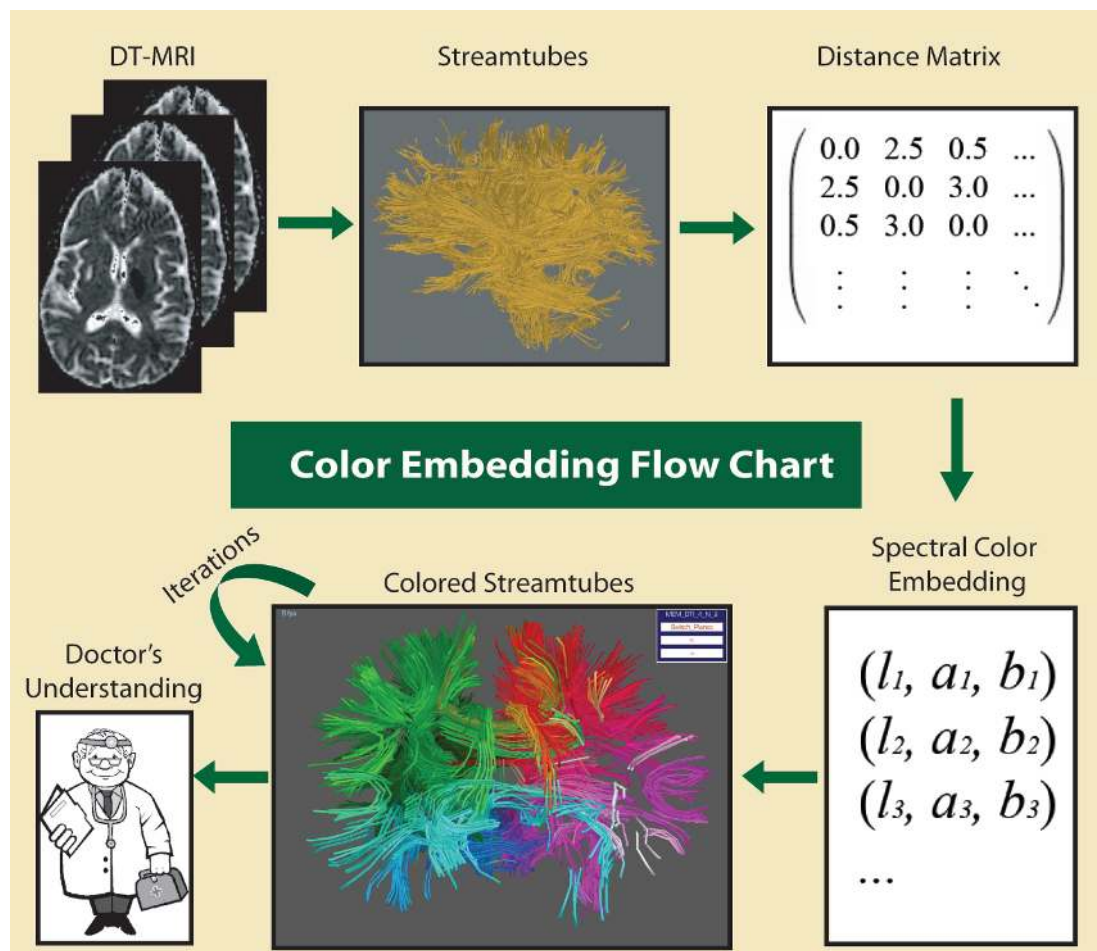


Figure 5.1: White-matter tract processing flow chart.

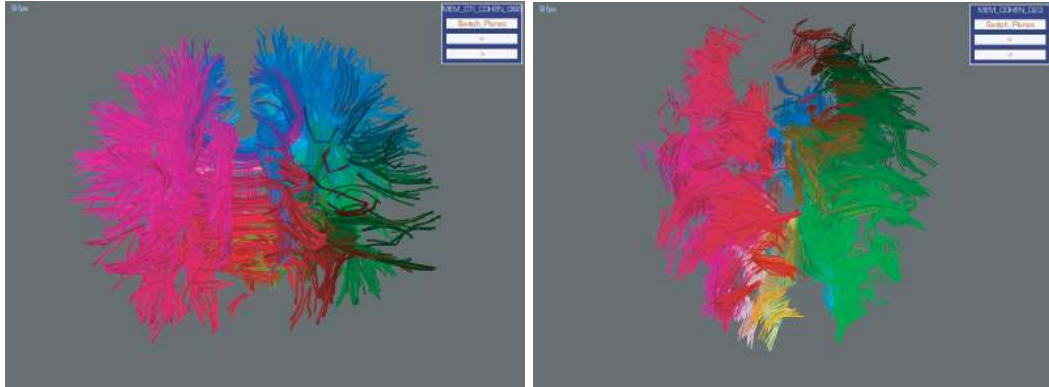


Figure 5.2: Visualizing a normal and an HIV-positive brain dataset using perceptually uniform color space.

easily gave context when navigating in 3D views. He found the subtle color variations were easier to process visually, and felt that he was the one making the model (instead of viewing a predefined cluster of tracts). We asked the expert how our approach of smooth color variation approach fared against displaying hard segmentation, in which whole bundles are colored with one color. The expert felt the smooth coloring was more compatible with the uncertainty of tractography.

5.3.3 Conclusion

Our evaluation suggests this is a promising approach. Our visualization method shows relevant anatomic structures without imposing a segmentation. The smooth subtle color variation between white-matter tracts in uniform perceptual color space helped the user visually identify meaningful anatomical structures.

5.4 Visualization Approach B: Texture Patterns

We present a new method for visually differentiating integral curves obtained from DTI volumes. The goal of our method is to reflect the spatial relations between visualized integral curves. This will enable the user to group similar curves together while differentiating dissimilar curves that may lie near one another. To this end, we first define a similarity measure and compute the similarities between the curves according to that measure. Then we encode this similarity information onto the streamtube representations of the curves as stripe texture patterns. We present examples of visualizations using four different pattern styles. We have evaluated our method with help of neuropsychologists; initial feedback

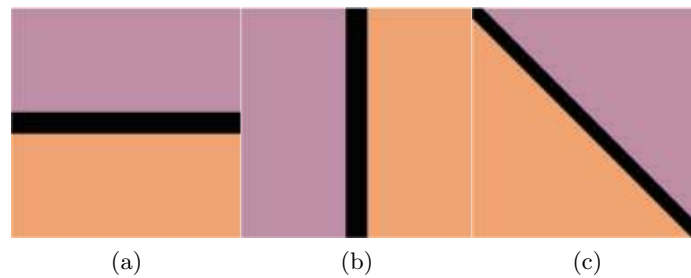


Figure 5.3: Textures: (a) horizontal, (b) vertical (c) diagonal; when applied on the tubes, in different positions, give four types of patterns(horizontal, vertical, diagonal and diamond).

suggests that our method can be useful in understanding the underlying connectivity of integral curves.

5.4.1 Method

We create our visualizations in three steps (Figure. 5.4): First, we generate integral curves from a DTI volume using a fiber-tracking algorithm [108]. Second, we adopt the flat-torus coloring scheme proposed by Demiralp et al. [35] to obtain pairs of colors for all the integral curves. We, however, modify the proposed method in two ways: In one, we initialize the “distance fitting” algorithm described by the authors with 2D points obtained by applying a spectral dimensionality reduction on the curves [27]. In the other, we get pairs of colors (instead of a single color) for each point by mapping the u, v and s, t components of the (u, v, s, t) flat-torus coordinates to two different isoluminant planes of the $L^*a^*b^*$ color space. Third, we apply the obtained color pairs, as textures with four different styles, onto streamtube representations of the curves. Using the obtained color pairs we generate three texture patterns: horizontal, vertical and diagonal. Figure. 5.3 shows the resulting textures if the color pair is orange and purple. In each texture, the two colors are separated by a dark line, as shown, intended to help the viewer distinguish the two colors when they are perceptually similar. Using different combinations of the texture and coordinate mapping, we apply four different styles: horizontal, vertical, diagonal and diamond, on the integral curves (see Figure. 5.5). Finally, we apply each of the four texture patterns to the integral curve model obtained from a volunteer’s brain DTI dataset.

5.4.2 Results

We apply our method to visualization of integral curves generated from a normal volunteer’s brain DTI dataset. Figure 5.6 shows the result of brain white-matter integral curve models

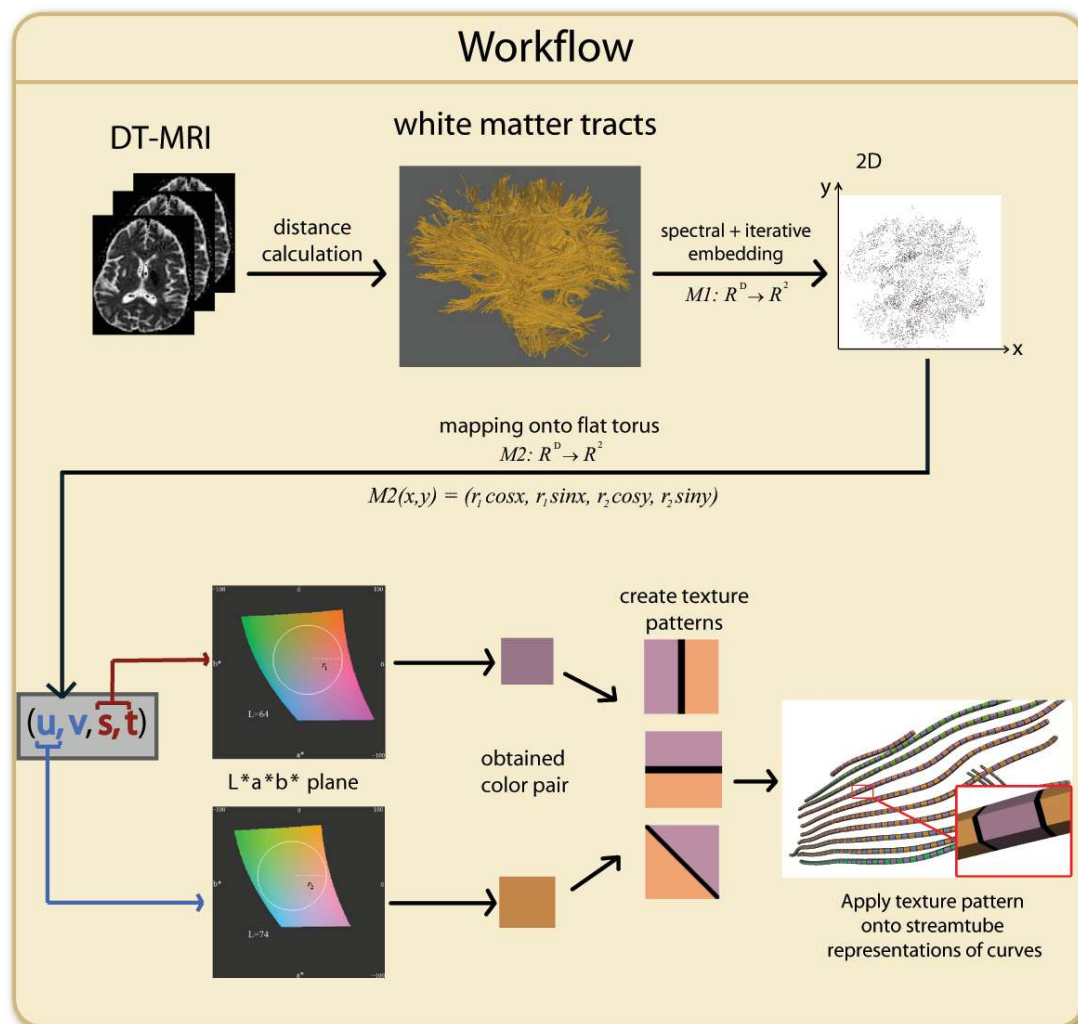


Figure 5.4: Workflow for visualizing white-matter tract using texture pattern.

by applying horizontal, vertical, diagonal and diamond texture pattern styles. In order to assess the utility of our visualization technique, we conducted a small anecdotal study with two neuropsychologists who routinely use visualizations of integral curves in their research. For comparison, we also generated a visualization of the same set of the integral using the RGB method. We asked our experts to evaluate both methods according to their effectiveness in understanding and exploration of the underlying neural tracts estimated. The experts' comments show that while the RGB method is good at capturing large structures, our visualization contains more information and has high sensitivity, allowing it to capture subtle differences within large structures.

Our experts noted that the ability to identify subtle changes within regions-of-interest is critical to diagnosing neurological abnormalities or disorders affecting the length and shape of neural tracts. They therefore pointed out that a useful application of our method would be to identify and compare ROIs across subjects. While one of the experts preferred the vertical texture pattern, the other preferred the diamond pattern. Both of the experts, however, gave a similar justification for their preferences, namely the ability to detect sharper boundaries between the curves and find the edges. This is not surprising because the overall perceived orientation of the dark bands in both texture patterns is orthogonal to the principal direction of the streamtubes, which helps to see boundaries of the streamtubes easily. The work presented here is preliminary and focuses on demonstrating the advantages of our method on DTI integral curves.

5.4.3 Conclusion

We present a new method for visualizing DTI integral curves. Our method applies texture patterns on streamtube representations of integral curves, encoding spatial relations between the curves. We demonstrate our method on integral curves obtained from a whole DTI brain dataset. Expert feedback shows that our visualization can complement existing standard methods by showing subtle differences within large structures of integral curves.

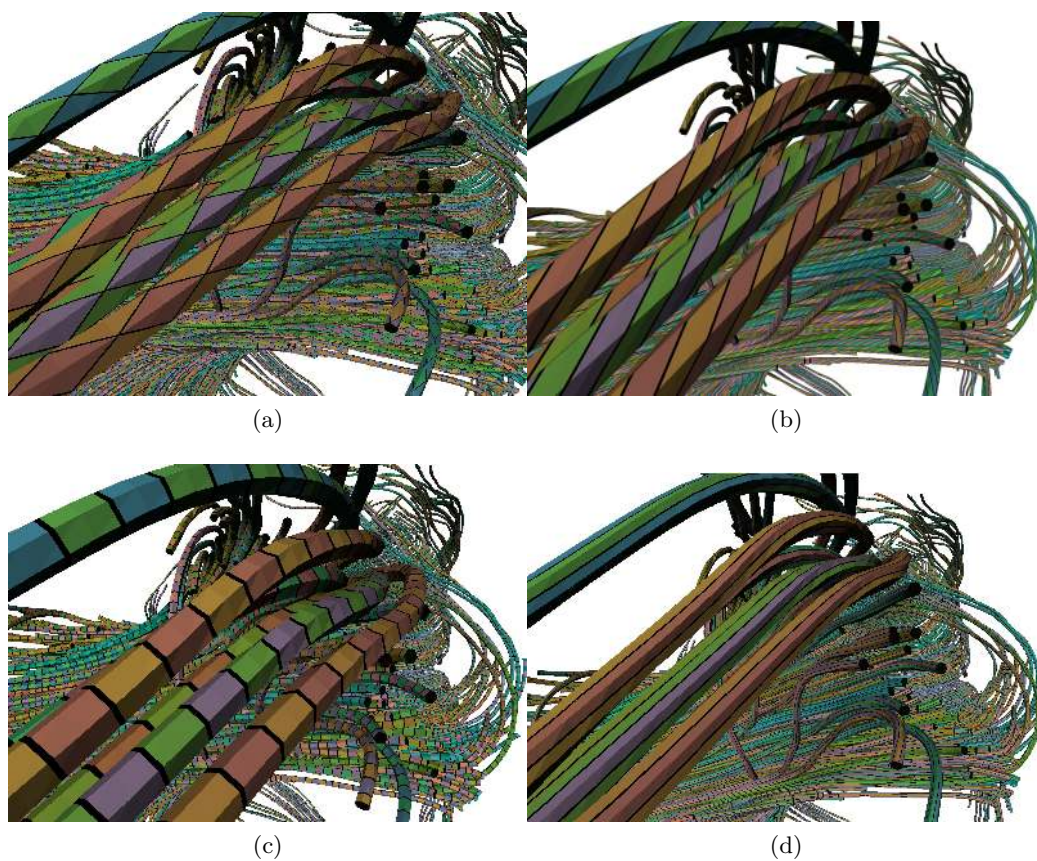


Figure 5.5: Four different patterns applied on corpus callosum streamtube model: (a) Diamond Pattern, (b) Diagonal Pattern (c) Vertical Pattern (d) Horizontal Pattern

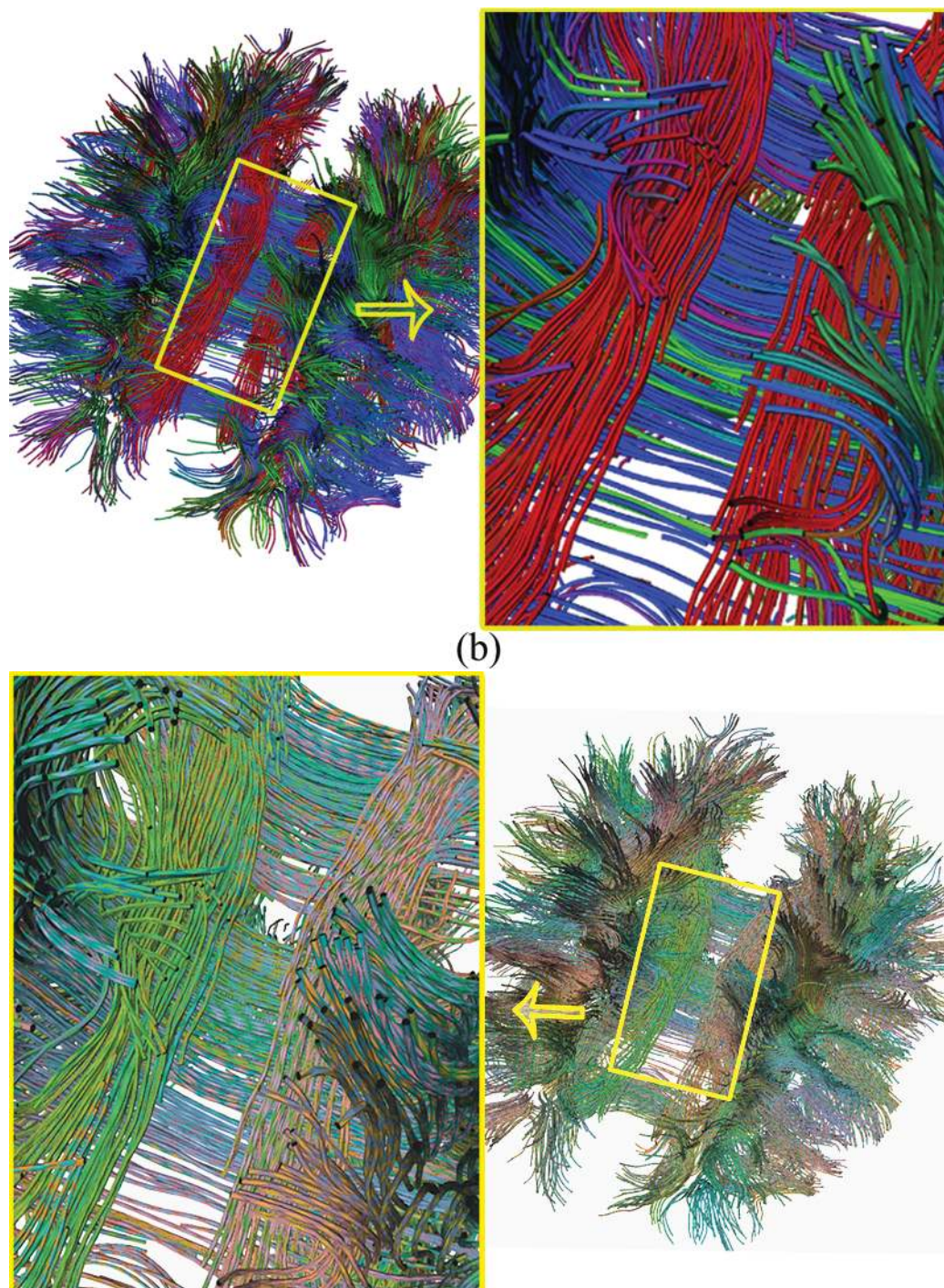


Figure 5.6: Applying RGB coloring vs. diamond pattern on whole brain model (a) RGB coloring applied. Notice that the two singular bundles in the middle are colored in red with nearly no noticeable subgroup color distinction. (b) Diamond pattern applied. Notice that smaller subgroups can be visually grouped within the bigger singular bundle

Chapter 6

Brain White Matter Tracts-of-Interest (TOI) Selection Tool

6.1 Introduction

Diffusion tensor imaging (DTI) makes possible the non-invasive exploration of fibrous white-matter structures within the human brain. Current DTI visualization and analysis has focused on rendering neural tracts and segmentation of white-matter trajectories into anatomically meaningful bundles [101]. The densely sampled neural tracts representing white-matter structures tend to be visually cluttered, making it difficult for brain scientists to understand the data. Automatic segmentation methods impose a rigid, possibly inaccurate, model of which white-matter pathways belong to which bundles. Instead, enabling brain scientists to interact with the visualization models and manually perform segmentation by selecting TOI is an important interaction which many published clinical research studies using DTI tractography [18] have relied on.

6.2 Related Work

Segmentation and clustering of white-matter pathways by interactive selection TOI has become a popular way for brain scientists to test their hypotheses of white-matter connectivity and functionality, and a number of tools have been developed for interactively assembling TOI into anatomically meaningful neural tract bundles. Sherbondy et al. [93]

defined volumes-of-interest to let users interactively group white-matter pathways going through these regions. Blaas, et al., [17] presented a real-time neural tract bundle selection system based on multiple convex selection objects. However, in these methods, the shape of the volume the user can define is rather limited, making selection cumbersome due to the curved and complex nature of white-matter pathways. CINCH, a 2D marking interface for selecting 3D TOI, has been developed recently [3] to alleviate the difficulties involved in selecting complex 3D structures using only commodity input devices, which offer only two degrees of freedom. However, CINCH users still find navigating and locating the desired white-matter structures undesirably time-consuming. It is also reported that selection using 2D plane intersection, as in CINCH, requires extensive neuroanatomical knowledge because the user loses the 3D context while working in the 2D space.

6.3 Taxonomy and Design Guidelines of TOI Selection

We present a set of findings from our user evaluation of state of the art TOI selection techniques. Tractography is a standard approach for visualizing the brain’s white-matter structure that is based on diffusion tensor imaging (DTI), and brain scientists need very efficient tools to select tracts-of-interest (TOI) for their research. We performed two evaluations aimed at better understanding these tools: a subjective study of three standard TOI selection tools looking at the utility, usability and user satisfaction with the design features, and a user performance evaluation to measure the speed and subjective reliability of two of the three standard TOI selection tools.

6.3.1 Introduction

The most popular approach to extracting the underlying neural tract structure from DTI data is tractography: reconstructing trajectories from DTI using streamtubes/streamlines. Selecting TOI for segmentation is the most frequent task in most clinical research studies using DTI tractography, such as [18]. Several TOI selection techniques have been proposed to let expert users obtain clustering interactively [93, 3, 17, 98]. Different TOI selection methods give users different levels of flexibility and efficiency in clustering the neural tracts. It is unclear which TOI selection method and combination of interaction techniques gives the expert user the best tools for the clustering task, and to the best of our knowledge, no studies have compared TOI selection techniques. We present the results from our user study evaluating the design features in three different TOI selection tools. We hope that

this study will improve the design of TOI selection tools and thus help brain scientists in brain diagnoses.

6.3.2 Methods for Evaluating TOI Selection Tools

We performed two user evaluations to gain insights into the nature of TOI selection tools for DTI. Four domain experts took part in both experiments. All TOI selection tools evaluated in the experiments ran on the same desktop hardware setup, and the dataset used was DTI scans from a normal subject.

6.3.2.1 TOI Selection Tools Studied

A number of tools have been developed for interactively selecting TOI for neural tracts; we look here at the TOI selection technique component of each interface. We evaluate and discuss three standard TOI selection tools: Brainapp, an interactive TOI selection application adapted from [93], CINCH [3], and MedINRIA [98]. Other tools such as DTI Studio [48] were not included in the study because their TOI selection techniques do not differ significantly from the three above.

6.3.2.2 Task

- **Experiment 1: Subjective User Evaluation**

Our goal here was a qualitative evaluation of the utility, usability and user satisfaction with different features of three TOI selection tools: Brainapp, CINCH, and MedINRIA. Participants were first trained on the techniques provided by each tool until they were reasonably proficient. They were then asked to select the corpus callosum, one of the most important white-matter structures in the brain. After the experiment, participants were asked to provide a subjective rating of the utility, usability and user satisfaction with its features; the ratings ranged from 1 to 7, 7 being the best. Our questionnaire considered the action space (features affecting how users interact with the model) and outside factors (features that assist in the selection process such as visual enhancement).

- **Experiment 2: User Performance Evaluation**

Our goal here was to obtain performance data on TOI selection techniques, using controlled tasks in a simplified environment. We compared user performance in selecting four different neural bundles defined in [102] using two standard tools: Brainapp and CINCH. (We

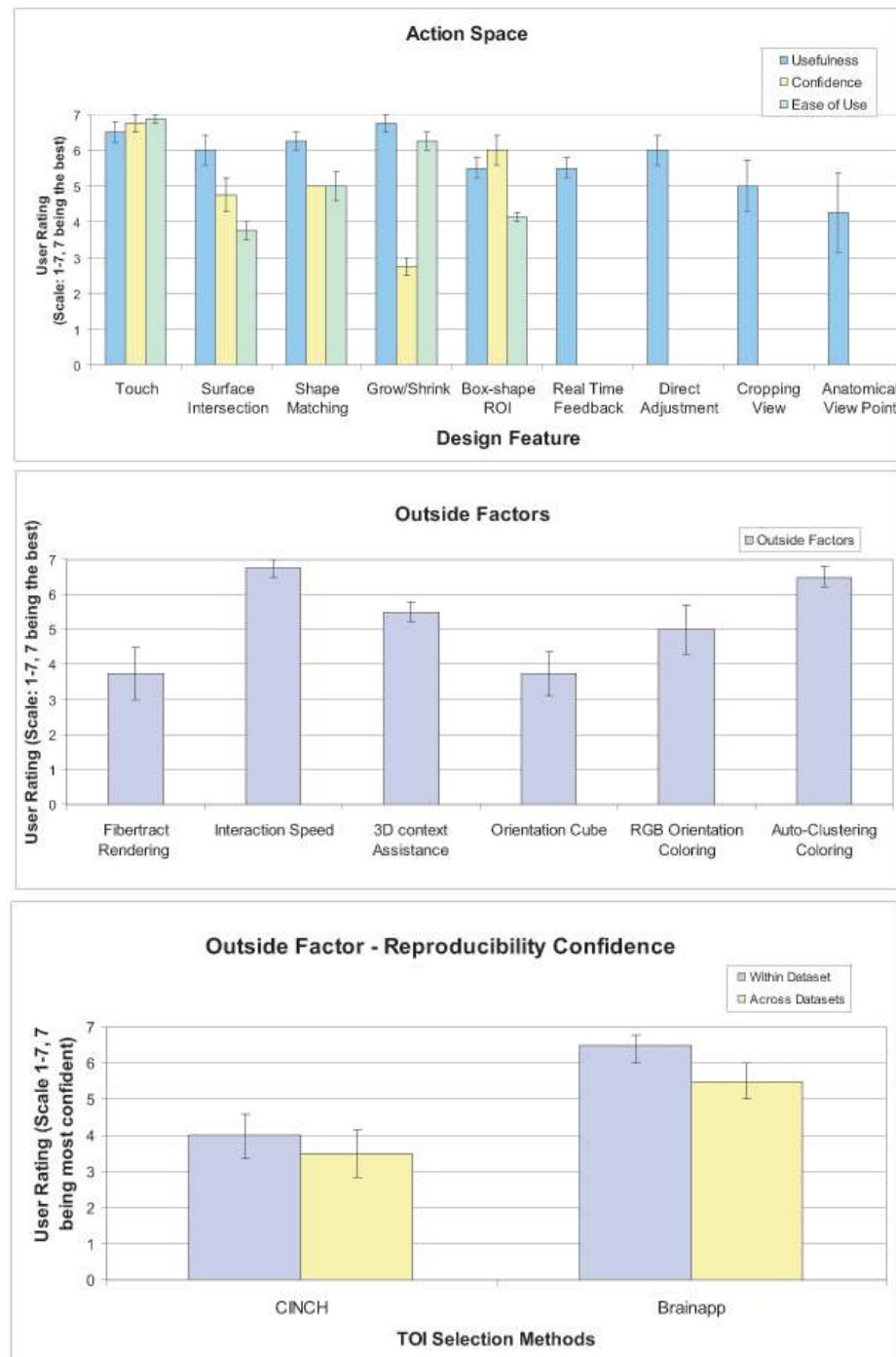


Figure 6.1: Subjective user evaluation results. Top: action space, bottom two: outside factors

omitted MedINRIA because its TOI selection interaction overlaps with those of Brainapp and CINCH.) The four white-matter structures – corpus callosum (CC), cingulum bundle, superior longitudinal fasciculus (SLF), and uncinate fasciculus (UF) – were chosen to represent the complexity and variation in neural bundles (Figure 6.2). The time participants took to make satisfactory selections of each assigned structure using each tool was recorded, and they were then asked to provide a confidence score for their final result on the basis of two criteria: correctness and completeness [69].

6.3.3 Results

6.3.3.1 Subjective User Evaluation Results

Figure 6.1 shows the result of our subjective user evaluation. Below we highlight some of the most interesting findings.

Action Space:

- **The *touch* tool was rated highest in all three rating categories**

Our analysis suggests two main reasons for its high performance. First, much of the selection process involves refining the selection results by removing outliers on the basis of anatomy; second, the marking operation is intuitively easy to understand, so that users gained confidence in using the tool. The disadvantage, however, is that some of those outliers may be the result of disease. Note that the *box-shape volume of interest (VOI)* method in Brainapp usually avoids this problem since regions of interest (ROI) are placed strictly on the basis of the standard starting and ending positions of the structure in the brain.

- **The *shape match* and *grow/shrink* had a high average score of 6 in terms of usefulness. However, the confidence score was rather low; in particular, *grow/shrink* had an average rating of only 2.7 out of 7.**

Outside Factors:

- **The scores for the usefulness of anatomical viewpoint control had the biggest variance range, 2-7.**

This suggests that the usefulness of this feature depends strongly on user preference. Providing brain scientists with an anatomical viewpoint could be an essential component of TOI selection tools that target those users who experience relatively higher difficulty in model navigation.

- **Users had high confidence in the reproducibility of their TOI selection result in Brainapp and MedINRIA, but much lower confidence in the reproducibility in CINCH.**

The box-shaped ROI method in Brainapp and MedINRIA has the advantage of systematically placing ROIs based on standard selection protocols [102]. Selection in CINCH depends strongly on drawing arbitrary marks, and brain scientists would find it hard to come up with a recipe for making their TOI selection reproducible.

6.3.3.2 User Performance Evaluation Results and Discussion

Figure 6.3 shows the time and confidence scores in picking out the four assigned white-matter structures. CINCH outperformed Brainapp in all three structures except the UF. This is an unexpected result, since the UF is a curving arc-shaped structure in the frontal lobe and we would expect the box-shaped regions to perform poorly in capturing this structure. We conjecture that this result occurred because: (1) The UF is at the outermost part of the frontal lobe of the brain, and a box can be placed at this location without too much occlusion, and (2) Most participants chose to use the *shape-match* operation in CINCH due to the special curving shape of the structure. Unfortunately, the algorithm performed very poorly in locating this shape, frustrating the users and delaying the whole selection process.

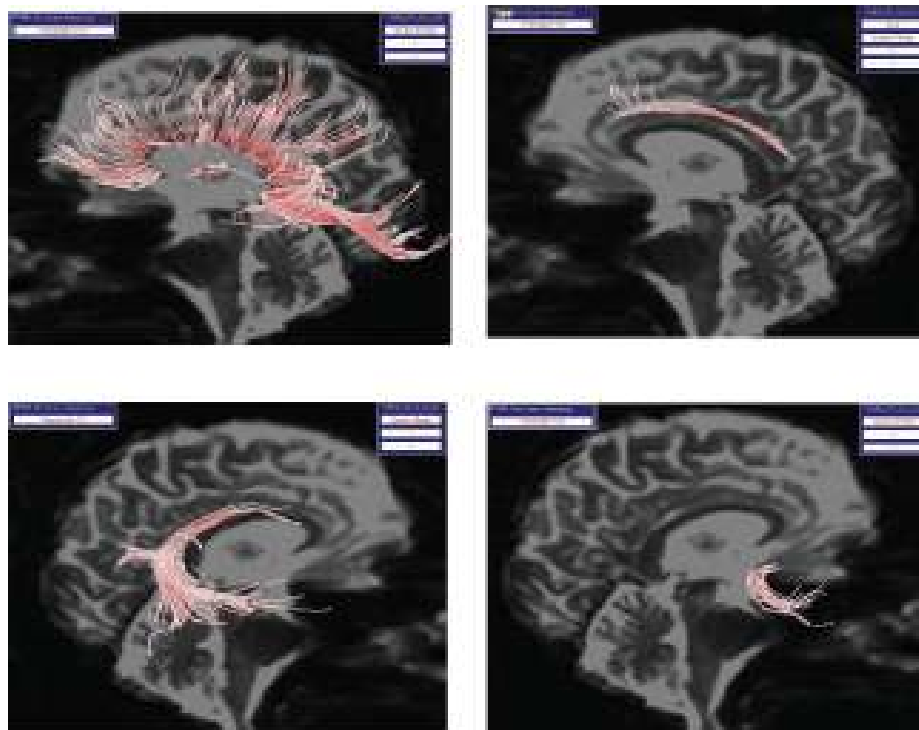
6.3.4 Conclusion

Evaluating and comparing the relative merits of different TOI selection methods for neural tract selection lead toward a formal understanding of the state of the art in TOI selection tools. Giving users relatively simple fixing/erasing mechanisms such as the *touch* mark in CINCH is very useful. The reproducibility of the selection methods should be carefully considered in the implementation so that users can reliably reproduce scientific analysis. Semi-automatic selection algorithms based on embedded data has a high potential to provide users with more efficient tools.

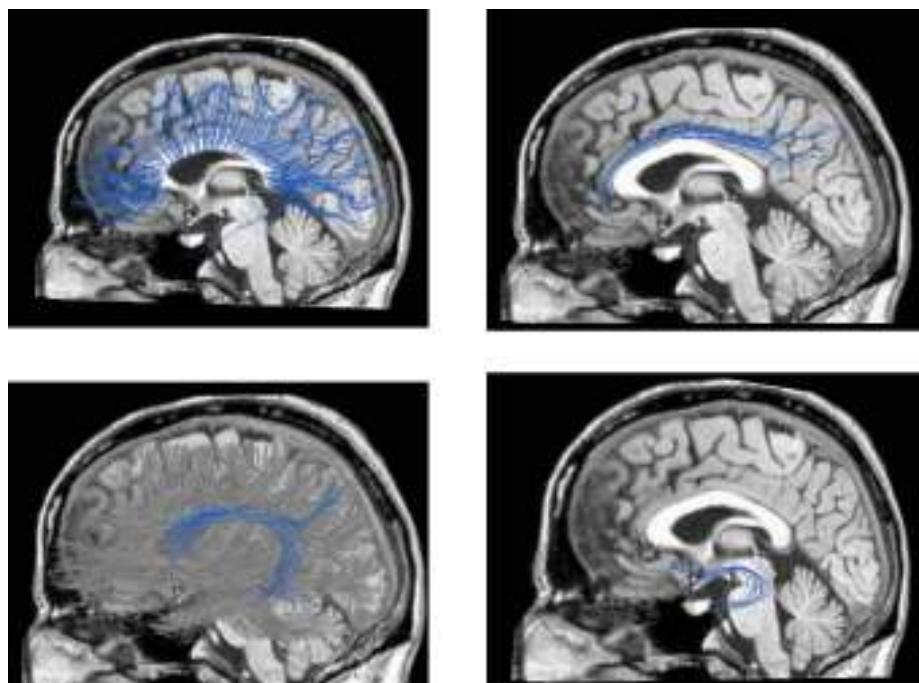
6.4 TOI Selection Approach A: 2D Sketching

6.4.1 Method

We provide the user with a flexible user interface to select TOI on the 2D cutting plane of the anatomical slices. We visualize distances between white-matter tracts using the metric



(a) Brainapp



(b) CINCH

Figure 6.2: Snapshot of a user's selection for the four assigned white-matter fiber bundles in experiment 2.

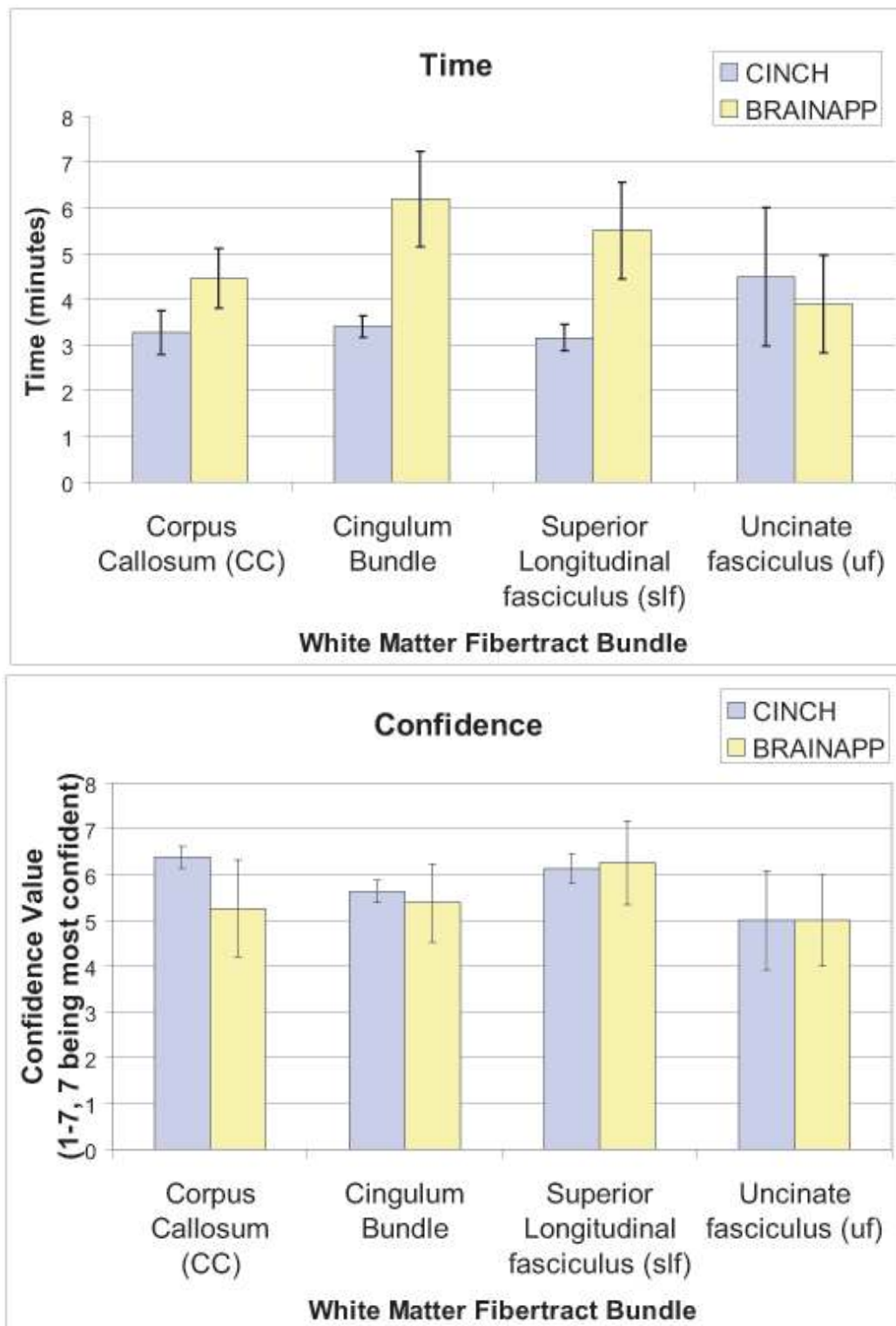


Figure 6.3: User performance evaluation results: time and confidence

in [108] and assign a coloring of streamtubes (see Section 5.3). We then view them in BrainApp [88] an interactive tool for visualizing DT-MRI data. We extended this software with a new selection interaction. The user selects axis-aligned planes in 3D (Figure 6.4b) and then views, as a 2D view (Figure 6.4c), the colors of streamtubes intersecting that slice. Next the user makes a free-form closed curve to select. The streamtubes that pass through the this region are selected (see Figure 6.4d). This axis-aligned view and selection method exploits the training neuro-scientists have received in viewing aligned 2D images (sectional anatomy) of the brain.

6.4.2 Results

We performed two informal evaluations with an expert visualizing a normal and an HIV-positive brain data-set. Our expert reported high anatomic specificity, and said he was easily able to pick out meaningful neural tract bundles even though colors varied smoothly. He noted that the 2D cutting plane view is friendly to use as it matches his training in neuroanatomy for identifying anatomical structures on 2D histology slices. He also commented that drawing a freeform lasso in the 2D image is straight forward to understand and easy to adopt as selection mechanism.

6.4.3 Conclusion

Our evaluation suggests this is a promising approach. Our visualization method shows relevant anatomic structures without imposing a segmentation. The tool provided a simpler 2D drawing TOI selection method, which is an important interaction in brain diagnosis for experts familiar with sectional anatomy.

6.5 TOI Selection Approach B: 3D Haptics-assisted Lasso Drawing

We present a new haptics-assisted 3D lasso drawing interface for selecting TOI in diffusion tensor imaging (DTI) in fishtank virtual reality (VR). This interface brings TOI selection tasks into 3D stereo VR with higher-input bandwidth devices. In the system, the 6D input Phantom device lets the user make selections by drawing a smooth 3D lasso with haptics constraint assistance directly in the 3D space. The hand tracker lets the user use hand gestures to rotate and zoom the model. Users also reported that making selections by drawing 3D lassos is easy, as it resembles pointing out structures to a collaborator with

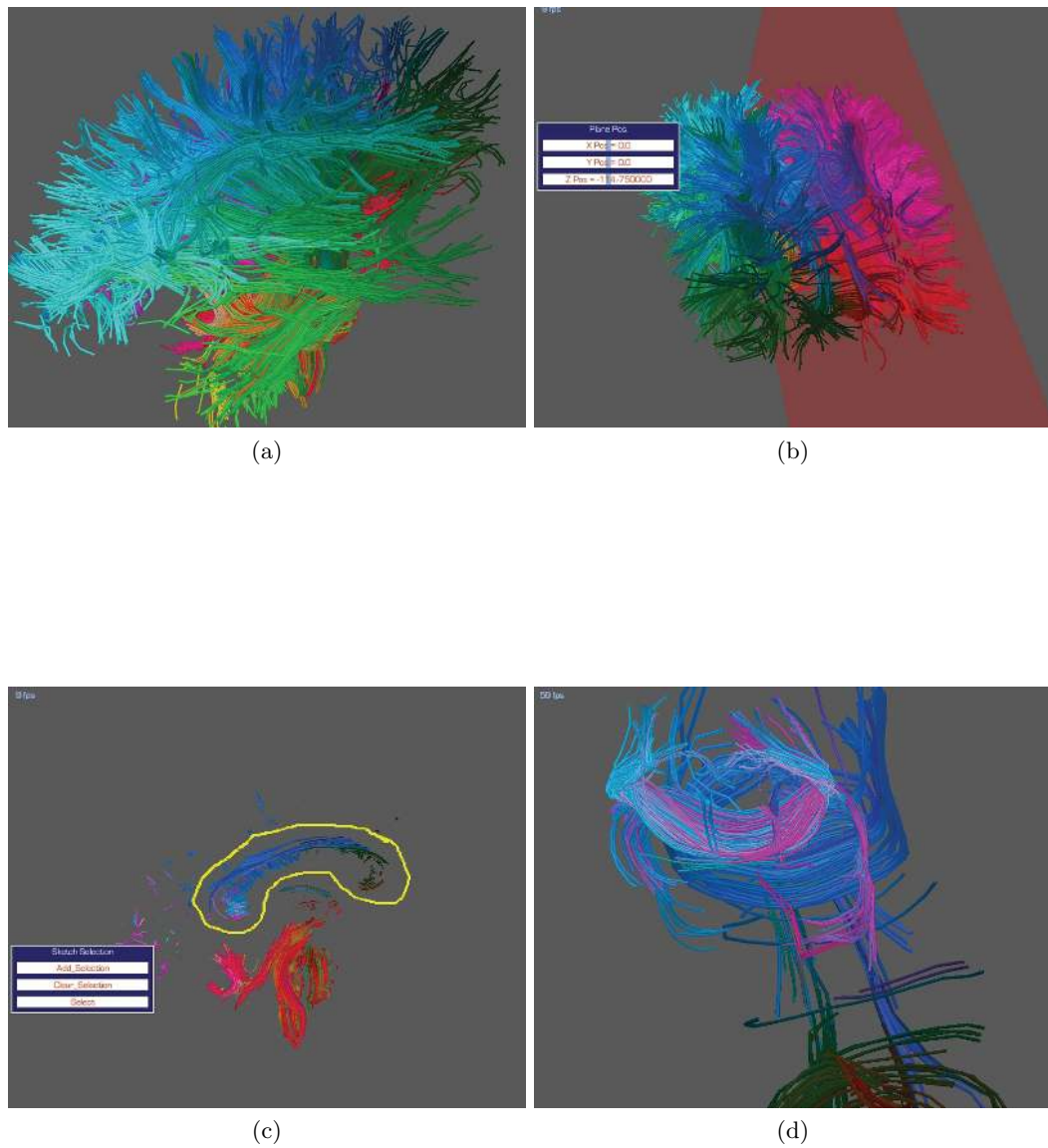


Figure 6.4: Our ROI selection application: sketching selection and interaction with data from the brain of a normal subject. (a) Color differences indicate differences between pathways shown with 4K tubes. (b) User selects an axis aligned plane corresponding to the midsagittal slice of the corpus callosum, displayed with a semi-transparent red plane. (c) Selected slice is shown as 2D image in which the user selects a freeform region (yellow curve). (d) All tracts passing through this region are displayed.

their fingers but has higher precision. Users also remarked that VR helped them appreciate the three-dimensional structure of the neural tracts more easily, and they gained more confidence in identifying the structures and the area they project in the brain. Working in the VR environment reduces the navigation time for the TOI selection task, a key challenge in TOI selection tools. Users were able to segment out tortuous structures that are often time-consuming to select using traditional rigidly shaped VOI neural pathway selection tools.

Most interfaces for selecting TOI interactively depend on devices such as mice and pens, which offer only two degrees of freedom for manipulation of 3D VOI, and they also use standard 2D monitor screens to display the 3D structure of the brain. Brain scientists have noted that they must constantly rotate the brain model in order to retain their mental picture of the 3D structure presented on the 2D screen. The extensive navigation time is also a key drawback in current TOI selection tools. Here we present a new haptics-assisted interface that uses a 3D lasso for selecting TOI in 3D stereo VR.

6.5.1 Method

To relieve some of the navigation challenges present in current TOI tools, we asked brain scientists to work in a nontraditional environment using a stereo VR environment with a head tracker to reduce visual clutter (Figure 6.5a) and a higher-degree-of-freedom input device (Figures 6.5b and 6.5c) to improve manipulation and selection.

The user wears head-tracked stereo glasses that support active stereo viewing. A 3D hand tracker is attached to the user’s finger so that rotation and zooming are controlled by hand gestures. The user draws 3D lassos for TOI using the Phantom force feedback device, which serves as a tangential guiding filter and makes it possible to draw a smooth lasso directly in the 3D space. We address the challenges involved in drawing the 3D lasso by integrating a dynamic dragging haptics constraint [52] [53] inspired by the dense and narrow nature of the neural tracts.

In our interface, selection is done using the Phantom device to draw a freeform 3D lasso around the neural tract bundle directly in the 3D space (Figure 6.5c). Figure 6.6 demonstrates making a TOI selection using the tool. First, the user selects a group of neural tracts by drawing a lasso in the space. This creates a 3D surface based on triangulation of the lasso and any neural tracts intersecting this surface are selected. The user can then perform multiple lasso operations with logical combinations of AND and OR, as illustrated in Figure 6.7, to obtain the desired neural tract bundle based on the characteristic trajectory.

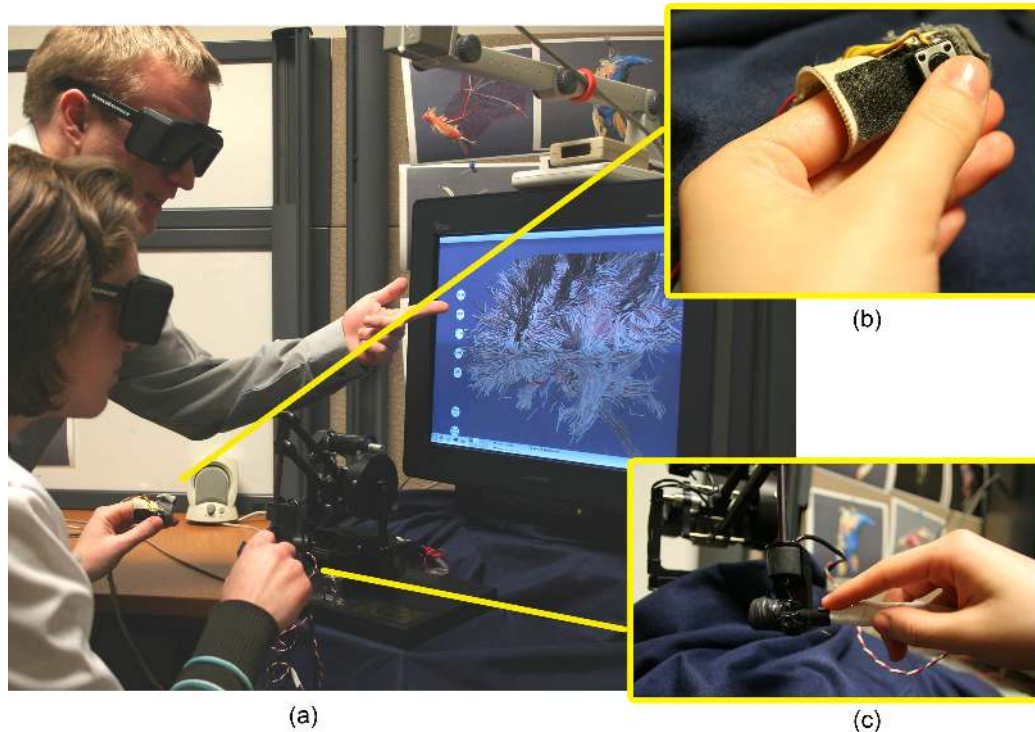


Figure 6.5: Users collaborating on hypotheses about white-matter connectivity using 3D lasso drawing selection interface in 3D stereo VR. (a) Fishtank VR setup. (b) 3D hand tracker. (c) Phantom force feedback device.

Figure 6.6 shows a user placing two lassos around the uncinete fasciculus (UF) and singling out the structure with an AND operation.

To evaluate our system, informal evaluations with 4 expert users visualizing two normal brain datasets were performed. The results are reported below.

6.5.2 Results

In our informal user evaluation with four expert users visualizing two normal brain datasets, users reported that:

- The 3D stereo environment let them identify 3D structures much more easily, since it avoids the visual flattening of the 3D white-matter structures found in traditional TOI selection tools.
- Navigation time was greatly reduced by the visual aid of 3D stereo combined with simple hand gestures for brain model manipulation. The users located and identified white-matter structures and the area they project in the brain quickly and with high confidence.

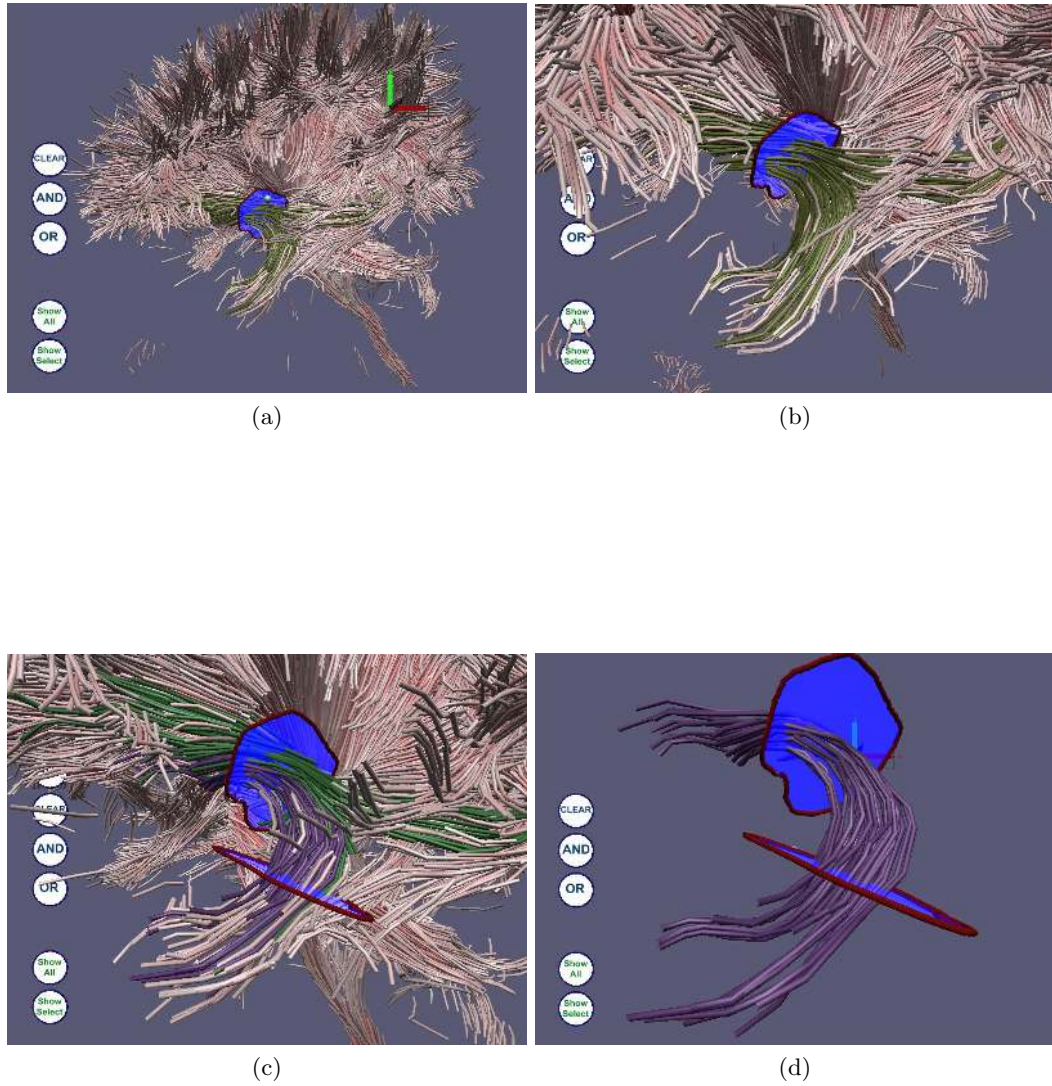


Figure 6.6: Our interface selecting the uncinatus fasciculus (UF) using the 3D lasso: the user places two lassos around the UF and singles out the structure with an AND operation. The final result is shown in purple.

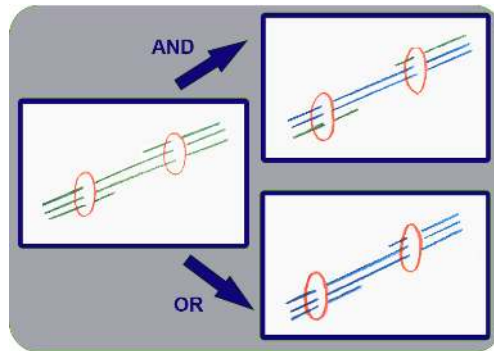


Figure 6.7: The two logical operations “AND” and “OR”. Two lassos delineate ROIs placed on anatomic landmarks. (1) AND operation: neural tracts that go through both ROIs are selected. (2) OR operation: neural tracts that go through either one of the ROIs are selected. The neural tracts resulting from the corresponding logical operations are shown in blue.

- Selection by lasso drawing is easy to learn. The users found that the ability to directly place the simple 3D lasso in 3D space let them easily segment tortuous brain structures, such as the uncinata fasciculus (UF), that with traditional VOI tools often require careful placement of multiple VOI with specific dimensions and locations.
- Users were often highly engaged in the process and noticed a reduction in the eye fatigue common in stereo interfaces.

The four brain scientists involved in this preliminary study expressed strong interest in adopting the system for their scientific analysis in the near future.

6.5.3 Conclusion

We have presented a new haptics-assisted 3D lasso-drawing interface for selecting TOI in DTI. Our system brings TOI selection tasks into 3D fishtank VR with higher-input-bandwidth devices. The brain scientists who worked with the 3D lasso tool in the stereo VR environment found that visual clutter was reduced and that they gained confidence in identifying the structures; they also noted that manipulating a brain model using a higher-order input device such as the hand tracker in the stereo environment greatly reduced navigation time. With white-matter structures vividly apparent, users could easily lasso out tortuous structures that are often time-consuming to specify using traditional rigid VOI selection tools.

Chapter 7

Conclusion

Although the application of diffusion MRI in brain imaging has been studied extensively over the past few decades, the computational solutions and the interactive visualization interfaces for localizing and extracting microstructural information at the axonal level in clinical settings have remained relatively unexplored. We have discussed in detail the benefits and sensitivity of reconstructing quantitative measurements of microstructural properties in brain-tissue regions of interest and improved qualitative interactive visualizations to enhance user performance in isolating those regions. This chapter concludes this dissertation work by summarizing our primary contributions and discussing future directions and applications.

7.1 Summary of Primary Contributions

We have addressed the creation of tools and methodologies for non-invasive microstructural and anatomical analysis of the brain white matter using diffusion MRI. Creating and refining these methodologies addresses important problems in neuroanatomy and in pathological studies of the brain.

The combination of visualizations, interactive interfaces, and computational techniques provides powerful tools for scientific data analysis and hypothesis testing. The visualizations developed here disentangle the complex white-matter structure from high-dimensional diffusion MRI data and provide additional visual cues such as tract spatial relationships. The interactive TOI selection interfaces using our 3D VR environment combined with anatomical landmarks let the user isolate specific regions of interest from their data for quantitative analysis within or across subjects more confidently and efficiently than current tools. The computational techniques accurately reveal important “hidden” microstructural information

in the specific regions extracted from the selection interfaces using clinically feasible acquisition in live human subjects. Together, these tools allow us to analyze data non-invasively and qualitatively on a global scale, as well as quantitatively in local brain regions.

7.2 Recommendations for Future Research and Practical Applications

The three main components presented in this dissertation, as outlined in Figure 7.1, demonstrate our computer science contributions by solving problems of immediate impact in brain science. These computational approaches can be generalized across different scientific disciplines. The first is the computational solutions for extracting “hidden” information and physical properties in medical imaging data in various scientific disciplines through mathematical modeling and analysis. The second area explores powerful visualization tools for combining multidimensional information obtained from various imaging modalities. The third area attacks the design of efficient interactive user interfaces for understanding and exploring scientific data at multiple scales. Below, we present recommendations for future research and practical applications of this dissertation work that combine these three research areas to expand our knowledge in computer science, neuroscience, and life sciences.

1. Disease state assessment and prediction

Histological studies have shown microstructural changes in a number of neurological disorders including multiple sclerosis, Alzheimer’s disease, and human immunodeficiency virus. However, the micorstructural changes over time in these diseases remain largely unstudied. It is crucial to evaluate computationally the progressive changes in the microstructure due to neurological disorders *in vivo*. These changes cannot be tracked using histological methods. We hypothesize that using our computational techniques to reveal the specific microstructural changes will: (1) enable earlier detection of neurological disorders, (2) provide direct assessment of the disorder’s severity, and (3) provide sensitive measurement to predict clinical disease progression.

2. Computational modeling and image analysis for information extraction

Computational information extraction problems similar to those brain-tissue problems discussed in this dissertation exist in many other areas of life sciences such as biology, DNA sequencing and cancer genomics. Numerous types of data and images are obtained by

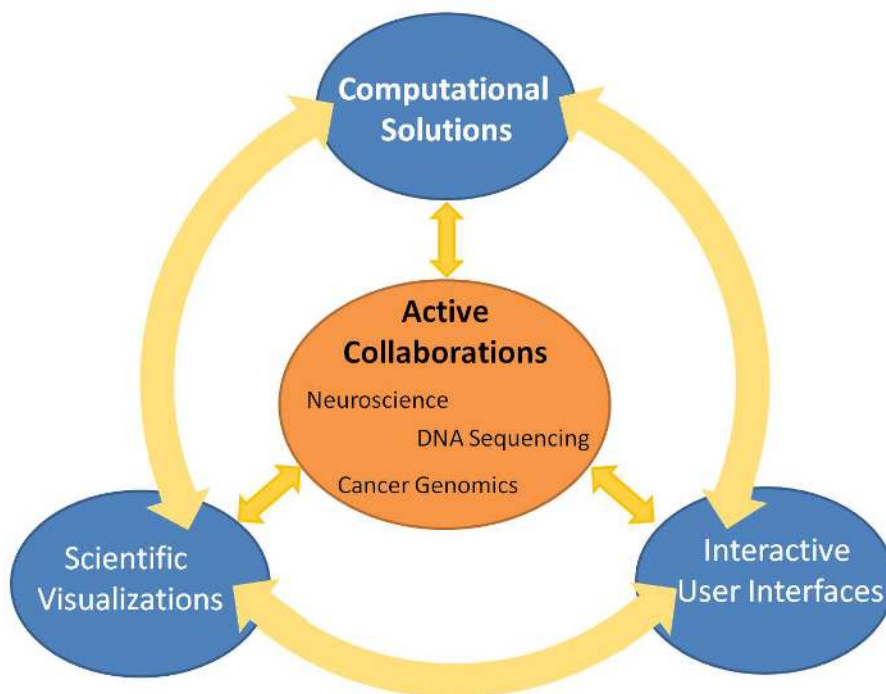


Figure 7.1: The general application of this dissertation’s three main components.

scientists in order to understand the exceedingly complex structure and functions of various biological tissues. Although the data we obtain in these domains encode important brain-structure information, they are only relative quantities measured in the physical environment of the imaging process. More direct measurements of the biological tissue properties remain “hidden” in those data. This information extraction process usually requires physical analysis of the underlying environment, mathematical modeling, and robust computational algorithms similar to what is described in Part I of this dissertation.

3. Powerful visualizations for combining multidimensional scientific information

The massive datasets obtained across all scientific disciplines present huge technological challenges. More information is being produced from various imaging modalities than the human eye and brain can begin to make sense of. Mapping these huge data sets into comprehensive visualizations that also make connections among different imaging modalities will greatly facilitate data integration. Powerful visualization tools can significantly enhance scientific understanding in brain function, molecular interactions, and protein networks. In brain science, for example, we obtain different kinds of information from various

imaging modalities such as diffusion MRI, spectral MRI, and microCT. Visualizations that integrate computationally extracted microstructural properties of white matter (e.g., axon radius and volume fraction) as well as diffusivity measures from diffusion MRI (e.g., fractional anisotropy and mean diffusivity) will greatly enhance the understanding of brain structure and its disease-introduced changes.

4. Interactive user interfaces for understanding and connecting data at multiple scales

Much scientific information and data are multidimensional and viewing them at different scales can drive significantly different discoveries. It is crucial to provide friendly user interfaces that can transition easily among different information scales embedded in the data. A promising approach is to provide a multi-touch tabletop interface for the multiscale analysis of brain connectivity. In brain data, the white-matter tracts constructed from diffusion MRI provide *macro-scale* information on brain connectivity. At the *micro-scale* level, we want to examine the properties of axons, estimated using computational techniques (Part I), that make up these white-matter tracts at the macro level (Part II). The changes observed over the course of brain diseases can differ significantly depending on the level of scale at which we work. A multi-touch interface will let users transition easily between micro and macro data scales, navigating at the touch of a fingertip from axons to tensors, to white-matter tracts, and to their terminations in the cortical gray matter. A tabletop implementation of the interface should encourage interdisciplinary and collaborative research – something that such data strongly demand.

7.3 Summary

Our work on computational techniques for enhancing the microstructural and anatomical analysis of brain white matter has demonstrated the accurate reconstruction of quantitative microstructural measurements and shown enhanced user performance in isolating tracts for pathological analysis. It also indicates many potential directions for future research and practical applications.

Appendix A

Neuroanatomy Terminology

- **Axon:** The core nerve fiber extending from a neuronal cell body. It conveys signal from one nerve cell to another nerve cell or to muscle or gland.
- **Central Nervous System (CNS):** The brain and the spinal cord. The part of the nervous system that functions to coordinate the activity of all parts of the bodies of multicellular organisms.
- **Corpus Callosum (CC):** A structure of the mammalian brain in the longitudinal fissure that connects the left and right cerebral hemispheres.
- **Demyelination:** The loss of myelin wrapped around axon that has previously formed.
- **Fractional Anisotropy (FA):** A scalar value between zero and one that describes the degree of anisotropy of a diffusion process.
- **Gray Matter (GM):** The part of the central nervous system, such as cerebral cortex, that contains nerve cell bodies and appears gray.
- **Myelin:** The coating around nerve fibers (axons) that acts to insulate the fibers and promote efficient electrical conduction.
- **White Matter:** The part of the central nervous system that contains myelinated nerve fibers and appears white.

Bibliography

- [1] F. Aboitiz, E. Rodriguez, R. Olivares, and E. Zaidel. Age-related changes in fibre composition of the human corpus callosum: sex differences. *Neuroreport*, 7(11):1761, 1996. [58]
- [2] F. Aboitiz, A.B. Scheibel, R.S. Fisher, and E. Zaidel. Fiber composition of the human corpus callosum. *Brain Research*, 598(1-2):143–153, 1992. [xv, xvi, 24, 28, 29, 44, 47, 48, 49, 56, 58, 59, 60, 61]
- [3] D. Akers. CINCH: A cooperatively designed marking interface for 3D pathway selection. In *Proceedings of the 19th annual ACM symposium on User interface software and technology*, page 42. ACM, 2006. [94, 95]
- [4] DC Alexander. A general framework for experiment design in diffusion MRI and its application in measuring direct tissue-microstructure features. *Magnetic Resonance in Medicine*, 60(2):439–48, 2008. [32, 33, 51, 72]
- [5] D.C. Alexander, P.L. Hubbard, M.G. Hall, E.A. Moore, M. Ptito, G.J.M. Parker, and T.B. Dyrby. Orientationally invariant indices of axon diameter and density from diffusion MRI. *NeuroImage*, 2010. [33, 47, 50, 56, 61, 62]
- [6] Y. Assaf and PJ Basser. Non parametric approach for axon diameter distribution estimation from diffusion measurements. *Proc Intl Soc Magn Reson Med*, 15:1536, 2007. [54]
- [7] Y. Assaf, T. Blumenfeld-Katzir, Y. Yovel, and P.J. Basser. AxCaliber: a method for measuring axon diameter distribution from diffusion MRI. *Magnetic Resonance in Medicine*, 59(6), 2008. [32]
- [8] Y. Assaf and Y. Cohen. Inferring Microstructural Information of White Matter from Diffusion MRI. *Diffusion MRI: From Quantitative Measurement to In-vivo Neuroanatomy*, page 127, 2009. [32, 40, 54]

- [9] Y. Assaf, R.Z. Freidlin, G.K. Rohde, and P.J. Basser. New modeling and experimental framework to characterize hindered and restricted water diffusion in brain white matter. *Magnetic Resonance in Medicine*, 52(5):965–978, 2004. [32, 35]
- [10] D. Barazany, D. Jones, and Y. Assaf. AxCaliber 3D. *Intl Soc Magn Reson Med*, 19:76, 2011. [32]
- [11] Daniel Barazany, Peter J. Basser, and Yaniv Assaf. In vivo measurement of axon diameter distribution in the corpus callosum of rat brain. *Brain*, 132:1210–1220, 2009. [xvi, 32, 54, 60, 61, 62]
- [12] P.J. Basser and D.K. Jones. Diffusion-tensor MRI: theory, experimental design and data analysis—a technical review. *NMR in Biomedicine*, 15(7-8):456–467, 2002. [12]
- [13] H.C. Berg. *Random walks in biology*. Princeton Univ Pr, 1993. [8]
- [14] C. Bjartmar, G. Kidd, S. Mork, R. Rudick, and B.D. Trapp. Neurological disability correlates with spinal cord axonal loss and reduced N-acetyl aspartate in chronic multiple sclerosis patients. *Annals of neurology*, 48(6):893–901, 2000. [28]
- [15] C. Bjartmar and B.D. Trapp. Axonal and neuronal degeneration in multiple sclerosis: mechanisms and functional consequences. *Current opinion in neurology*, 14(3):271, 2001. [27, 32]
- [16] C. Bjartmar, JR Wujek, and BD Trapp. Axonal loss in the pathology of MS: consequences for understanding the progressive phase of the disease. *Journal of the neurological sciences*, 206(2):165–171, 2003. [27, 64]
- [17] J. Blaas, C.P. Botha, B. Peters, F.M. Vos, and F.H. Post. Fast and reproducible fiber bundle selection in DTI visualization. *IEEE Visualization, 2005. VIS 05*, pages 59–64, 2005. [94]
- [18] D. Bonekamp, LM Nagae-Poetscher, M. Degaonkar, M. Matson, S. Mori, and A. Horska. Intra-rater and inter-rater reproducibility of FA and ADC: a clinical pediatric DTI study. *Intl Soc Magn Reson Med*, 13:648, 2011. [7, 93, 94]
- [19] KR Brownstein and CE Tarr. Importance of classical diffusion in NMR studies of water in biological cells. *Physical Review A*, 19(6):2446–2453, 1979. [67]
- [20] A. Brun and Englund. E. A white matter disorder in dementia of the Alzheimer type: a pathoanatomical study. *Ann Neurol.*, 19(3):253–262, 1986. [27, 64]

- [21] Anders Brun, Hae-Jeong Park, Hans Knutsson, and Carl-Fredrik Westin. Coloring of dt-mri fiber traces using laplceian eigenmaps. In *EUROCAST*, pages 564–572, 2003. [85]
- [22] Thomas Caceci. Nervous tissue, <http://education.vetmed.vt.edu/curriculum/vm8054/>. [xiv, 37]
- [23] PT Callaghan. Pulsed-gradient spin-echo NMR for planar, cylindrical, and spherical pores under conditions of wall relaxation. *Journal of Magnetic Resonance, Series A*, 113(1):53–59, 1995. [38, 68]
- [24] P.T. Callaghan. A simple matrix formalism for spin echo analysis of restricted diffusion under generalized gradient waveforms. *Journal of Magnetic Resonance*, 129(1):74–84, 1997. [38]
- [25] PT Callaghan, A. Coy, D. MacGowan, KJ Packer, and FO Zelaya. Diffraction-like effects in NMR diffusion studies of fluids in porous solids, 1991. [33]
- [26] A. Caprihan, LZ Wang, and E. Fukushima. A multiple-narrow-pulse approximation for restricted diffusion in a time-varying field gradient. *Journal of Magnetic Resonance, Series A*, 118(1):94–102, 1996. [36]
- [27] Ali Civril, Malik Magdon-Ismael, and Eli Bocek-Rivele. Sde: Graph drawing using spectral distance embedding. In *GD'05*, Limerick, Ireland, 2005. [85, 88]
- [28] J. Clayden, Z. Nagy, M. Hall, C. Clark, and D. Alexander. Active imaging with dual spin-echo diffusion MRI. *Information Processing in Medical Imaging*, pages 264–275, 2009. [33]
- [29] JD Clayden, Z. Nagy, DC Alexander, and CA Clark. Axon radius estimation using optimised Stejskal–Tanner and dual spin-echo sequences at modest SNR. *Proc Intl Soc Mag Reson Med*, 17:1397, 2009. [33, 54]
- [30] S. Cluskey and DB Ramsden. Mechanisms of neurodegeneration in amyotrophic lateral sclerosis. *Molecular Pathology*, 54(6):386, 2001. [28]
- [31] PA Cook, Y. Bai, S. Nedjati-Gilani, KK Seunarine, MG Hall, GJ Parker, and DC Alexander. Camino: open-source diffusion-MRI reconstruction and processing. *Intl Soc Magn Reson Med*, 14:2759, 2006. [43]

- [32] DG Cory, AN Garroway, and JB Miller. Applications of spin transport as a probe of local geometry. *Polym Preprints*, 31:149–150, 1990. [33, 34]
- [33] GC DeLuca, GC Ebers, and MM Esiri. Axonal loss in multiple sclerosis: a pathological survey of the corticospinal and sensory tracts. *Brain*, 127(5):1009, 2004. [28]
- [34] GC Deluca, GC Ebers, and MM Esiri. The extent of axonal loss in the long tracts in hereditary spastic paraplegia. *Neuropathology and Applied Neurobiology*, 30(6):576–584, 2004. [27, 28]
- [35] C. Demiralp, S Zhang, D. Tate, S. Correia, and D. H. Laidlaw. Connectivity-aware sectional visualization of 3DDTI volumes using perceptual flat-torus coloring and edge rendering. In *Proceedings of Eurographics*, 2006. [88]
- [36] I. Drobnjak, H. Zhang, M.G. Hall, and D.C. Alexander. The matrix formalism for generalised gradients with time-varying orientation in diffusion nmr. *Journal of Magnetic Resonance*, 210:151–157, 2011. [43]
- [37] P. DuChateau and D.W. Zachmann. *Schaum's outline of theory and problems of partial differential equations*. Schaum's Outline Series, 1986. [22]
- [38] J.M. Edgar and I.R. Griffiths. White Matter Structure: A Microscopists View. *Diffusion MRI: From Quantitative Measurement to In-vivo Neuroanatomy*, page 75, 2009. [33, 44]
- [39] N. Evangelou, D. Konz, MM Esiri, S. Smith, J. Palace, and PM Matthews. Regional axonal loss in the corpus callosum correlates with cerebral white matter lesion volume and distribution in multiple sclerosis. *Brain*, 123(9):1845, 2000. [32]
- [40] R.L. Friede and T. Samorajski. Axon caliber related to neurofilaments and microtubules in sciatic nerve fibers of rats and mice. *The Anatomical Record*, 167(4):379–387, 1970. [23, 35]
- [41] P. Ganter, C. Prince, and M.M. Esiri. Spinal cord axonal loss in multiple sclerosis: a post-mortem study. *Neuropathology and Applied Neurobiology*, 25(6):459–467, 1999. [27, 28, 32, 33, 51]
- [42] W.R. Gilks, W.R. Gilks, S. Richardson, and D.J. Spiegelhalter. *Markov chain Monte Carlo in practice*. Chapman & Hall/CRC, 1996. [42]

- [43] K.D. Graf and U. Schramm. Diameter of axons and thickness of myelin sheaths of the pyramidal tract fibres in the adult human medullary pyramid. *Anatomischer Anzeiger*, 157(2):97, 1984. [25]
- [44] M. Hall and D. Alexander. Convergence and Parameter Choice for Monte-Carlo Simulations for Diffusion MRI. *IEEE transactions on medical imaging*, 2009. [43]
- [45] MG Hall and DC Alexander. Finite pulse width improve fibre orientation estimates in diffusion tensor MRI. *Intl Soc Magn Reson Med*, page 1076, 2006. [72]
- [46] T. Heads, M. Pollock, A. Robertson, WHF Sutherland, and S. Allpress. Sensory nerve pathology in amyotrophic lateral sclerosis. *Acta neuropathologica*, 82(4):316–320, 1991. [28]
- [47] J.R. Hughes. Autism: The first firm finding= underconnectivity? *Epilepsy & Behavior*, 11(1):20–24, 2007. [28]
- [48] H. Jiang, P. Van Zijl, J. Kim, G.D. Pearlson, and S. Mori. Dtistudio: resource program for diffusion tensor computation and fiber bundle tracking. *Computer methods and programs in biomedicine*, 81(2):106–116, 2006. [95]
- [49] D. Jianu, W. Zhou, C. Demiralp, and DH Laidlaw. Visualizing spatial relations between 3D-DTI integral curves using texture patterns. *Proceedings of IEEE Visualization Poster Compendium*, 2007. [5]
- [50] R. Jianu, W. Zhou, R. Cabeen, D. Dickstein, and D.H. Laidlaw. Visualizing tractography metrics of cortical-connectivity integrity in diffusion imaging. *Intl Soc Magn Reson Med*, 19:3938, 2012. [5]
- [51] H. Johansen-Berg and T.E.J. Behrens. *Diffusion MRI: from quantitative measurement to in-vivo neuroanatomy*. Academic Press, 2009. [xiii, 12, 13, 23, 24, 25, 56]
- [52] D.F. Keefe, R.C. Zeleznik, and D.H. Laidlaw. Drawing on air: Input techniques for controlled 3D line illustration. *IEEE transactions on visualization and computer graphics*, 13(5):1067–1080, 2007. [103]
- [53] D.F. Keefe, R.C. Zeleznik, and D.H. Laidlaw. Tech-note: Dynamic dragging for input of 3D trajectories. In *Proceedings of the 2008 IEEE Symposium on 3D User Interfaces-Volume 00*, pages 51–54. IEEE Computer Society, 2008. [103]

- [54] M.A. Koch and J. Finsterbusch. Compartment size estimation with double wave vector diffusion-weighted imaging. *Magnetic Resonance in Medicine*, 60(1):90–101, 2008. [33, 45]
- [55] M.A. Koch and J. Finsterbusch. Numerical simulation of double-wave vector experiments investigating diffusion in randomly oriented ellipsoidal pores. *Magnetic Resonance in Medicine*, 62(1):247–254, 2009. [33, 45]
- [56] M.A. Koch and J. Finsterbusch. Towards compartment size estimation in vivo based on double wave vector diffusion weighting. *NMR in Biomedicine*, 2011, 2011. [34]
- [57] K. Kure, KM Weidenheim, WD Lyman, and DW Dickson. Morphology and distribution of HIV-1 gp41-positive microglia in subacute AIDS encephalitis. *Acta Neuropathologica*, 80(4):393–400, 1990. [27, 64]
- [58] T. Kuroiwa, I. Yamada, N. Katsumata, S. Endo, and K. Ohno. Ex vivo measurement of brain tissue viscoelasticity in postischemic brain edema. *Brain Edema XIII*, pages 254–257, 2006. [27, 64]
- [59] AS LaMantia and P. Rakic. Axon overproduction and elimination in the corpus callosum of the developing rhesus monkey. *Journal of Neuroscience*, 10(7):2156, 1990. [25]
- [60] A.S. LaMantia and P. Rakic. Cytological and quantitative characteristics of four cerebral commissures in the rhesus monkey. *The Journal of Comparative Neurology*, 291(4), 1990. [xiv, 24, 25, 26, 27, 37]
- [61] J. Lätt, M. Nilsson, D. van Westen, R. Wirestam, F. Ståhlberg, and S. Brockstedt. Diffusion-weighted MRI measurements on stroke patients reveal water-exchange mechanisms in sub-acute ischaemic lesions. *NMR in Biomedicine*, 22(6):619–628, 2009. [28, 64]
- [62] G. Lovas, N. Szilagy, K. Majtenyi, M. Palkovits, and S. Komoly. Axonal changes in chronic demyelinated cervical spinal cord plaques. *Brain*, 123(2):308, 2000. [xiii, xiv, 3, 27, 29, 32, 33, 51]
- [63] D. Lunn, D. Spiegelhalter, A. Thomas, and N. Best. The BUGS project: Evolution, critique and future directions. *Statistics in medicine*, 28(25):3049–3067, 2009. [42]

- [64] D.W. Marquardt. An algorithm for least-squares estimation of nonlinear parameters. *Journal of the Society for Industrial and Applied Mathematics*, 11(2):431–441, 1963. [42]
- [65] C. Meier, W. Dreher, and D. Leibfritz. Diffusion in compartmental systems. II. Diffusion-weighted measurements of rat brain tissue in vivo and postmortem at very large b-values. *Magnetic Resonance in Medicine*, 50(3):510–514, 2003. [74]
- [66] C. Meier, W. Dreher, and D. Leibfritz. Diffusion in compartmental systems. I. A comparison of an analytical model with simulations. *IEEE Trans Med Imag*, 26:1437–1447, 2007. [71]
- [67] P. Møllergaard, F. Bengtsson, M.L. Smith, V. Riesenfeld, and B.K. Siesjö. Time course of early brain edema following reversible forebrain ischemia in rats. *Stroke*, 20(11):1565, 1989. [27]
- [68] P.P. Mitra. Multiple wave-vector extensions of the NMR pulsed-field-gradient spin-echo diffusion measurement. *Physical Review B*, 51(21):15074–15078, 1995. [33, 45]
- [69] B. Mobergs, A. Vilanova, and J.J. van Wijk. Evaluation of fiber clustering methods for diffusion tensor imaging. In *Visualization, 2005. VIS 05. IEEE*, pages 65–72. Ieee, 2005. [97]
- [70] S. Mori, S. Wakana, LM Nagae-Poetscher, and PCM Van Zijl. MRI atlas of human white matter. *American Journal of Neuroradiology*, 27(6):1384, 2006. [8]
- [71] S. Mori and J. Zhang. Principles of diffusion tensor imaging and its applications to basic neuroscience research. *Neuron*, 51(5):527–539, 2006. [xiii, 13]
- [72] R.A. Nixon. Dynamic behavior and organization of cytoskeletal proteins in neurons: reconciling old and new findings. *Bioessays*, 20(10):798–807, 1998. [23]
- [73] M. O’Sullivan, PE Summers, DK Jones, JM Jarosz, SCR Williams, and HS Markus. Normal-appearing white matter in ischemic leukoaraiosis: A diffusion tensor MRI study, 2001. [7]
- [74] E. Özarslan and P.J. Basser. MR diffusion–diffraction phenomenon in multi-pulse-field-gradient experiments. *Journal of Magnetic Resonance*, 188(2):285–294, 2007. [33, 36]

- [75] E. Özarslan and P.J. Basser. Microscopic anisotropy revealed by NMR double pulsed field gradient experiments with arbitrary timing parameters. *The Journal of Chemical Physics*, 128:154511, 2008. [33, 34, 36]
- [76] S. Pajevic and C. Pierpaoli. Color schemes to represent the orientation of anisotropic tissues from diffusion tensor data: Application to white matter fiber tract mapping in the human brain. *Magnetic Resonance in Medicine*, 42(3):526–540, 1999. [85]
- [77] E. Panagiotaki, H. Fonteijn, B. Siow, M. Hall, A. Price, M. Lythgoe, and D. Alexander. Two-compartment models of the diffusion MR signal in brain white matter. *Medical Image Computing and Computer-Assisted Intervention–MICCAI*, pages 329–336, 2009. [32, 62]
- [78] D.N. Pandya and B. Seltzer. The topography of commissural fibers. *Two hemispheresone brain: functions of the corpus callosum (Lepore F, Ptito M, Jasper HH, eds)*, pages 47–73, 1986. [xiv, 25, 26]
- [79] C. Pierpaoli, A. Barnett, S. Pajevic, R. Chen, L.R. Penix, A. Virta, and P. Basser. Water Diffusion Changes in Wallerian Degeneration and Their Dependence on White Matter Architecture. *Neuroimage*, 13(6):1174–1185, 2001. [7]
- [80] C. Pierpaoli and P.J. Basser. Toward a quantitative assessment of diffusion anisotropy. *Magnetic Resonance in Medicine*, 36(6):893–906, 1996. [32]
- [81] J. Piven, J. Bailey, B.J. Ranson, and S. Arndt. An MRI study of the corpus callosum in autism. *American Journal of Psychiatry*, 154(8):1051, 1997. [28]
- [82] W.S. Price, A.V. Barzykin, K. Hayamizu, and M. Tachiya. A model for diffusive transport through a spherical interface probed by pulsed-field gradient NMR. *Biophysical Journal*, 74(5):2259–2271, 1998. [67, 69]
- [83] PL Randall. Schizophrenia, abnormal connection, and brain evolution. *Medical Hypotheses*, 10(3):247–280, 1983. [28]
- [84] TG Reese, O. Heid, RM Weisskoff, and VJ Wedeen. Reduction of eddy-current-induced distortion in diffusion MRI using a twice-refocused spin echo. *Magnetic Resonance in Medicine*, 49(1):177–182, 2003. [34]
- [85] D. Rice and S. Barone Jr. Critical periods of vulnerability for the developing nervous system: evidence from humans and animal models. *Environmental Health Perspectives*, 108(Suppl 3):511, 2000. [28]

- [86] JM Ritchie. On the relation between fibre diameter and conduction velocity in myelinated nerve fibres. *Proceedings of the Royal Society of London. Series B, Biological Sciences (1934-1990)*, 217(1206):29–35, 1982. [24]
- [87] A. Rosset, L. Spadola, and O. Ratib. Osirix: an open-source software for navigating in multidimensional dicom images. *Journal of Digital Imaging*, 17(3):205–216, 2004. [xvi, 55, 56]
- [88] Lee S., Correia S., Tate D., Paul R., Zhang S., Salloway S., Malloy P., and Laidlaw D.H. Quantitative Tract-of-Interest Metrics for White-Matter Integrity Based on Diffusion Tensor MRI Data. *Intl Soc Magn Reson Med*, 14:283, 2006. [85, 101]
- [89] E.D. Schwartz, E.T. Cooper, C.L. Chin, S. Wehrli, A. Tessler, and D.B. Hackney. Ex vivo evaluation of ADC values within spinal cord white matter tracts. *American Journal of Neuroradiology*, 26(2):390, 2005. [xiv, 25, 28]
- [90] N. Shemesh, E. Özarslan, P.J. Basser, and Y. Cohen. Measuring small compartmental dimensions with low-q angular double-PGSE NMR: The effect of experimental parameters on signal decay. *Journal of Magnetic Resonance*, 198(1):15–23, 2009. [34]
- [91] N. Shemesh, E. Özarslan, P.J. Basser, and Y. Cohen. Accurate noninvasive measurement of cell size and compartment shape anisotropy in yeast cells using double-pulsed field gradient MR. *NMR in Biomedicine*, 2011, 2011. [34]
- [92] Noam Shemesh, Evren Özarslan, Michal E. Komlosh, Peter J. Basser, and Yoram Cohen. From single-pulsed field gradient to double-pulsed field gradient MR: gleaning new microstructural information and developing new forms of contrast in MRI. *NMR in Biomedicine*, 23(7):757–780, Aug, 2010. [34]
- [93] A. Sherbondy, D. Akers, R. Mackenzie, R. Dougherty, and B. Wandell. Exploring connectivity of the brain’s white matter with dynamic queries. *IEEE transactions on visualization and computer graphics*, pages 419–430, 2005. [93, 94, 95]
- [94] G.J. Stanisz, G.A. Wright, R.M. Henkelman, and A. Szafer. An analytical model of restricted diffusion in bovine optic nerve. *Magnetic Resonance in Medicine*, 37(1), 1997. [62, 64]
- [95] K.G. Su, G. Banker, D. Bourdette, and M. Forte. Axonal degeneration in multiple sclerosis: the mitochondrial hypothesis. *Current Neurology and Neuroscience Reports*, 9(5):411–417, 2009. [32]

- [96] H.A. Swadlow, S.G. Waxman, and N. Geschwind. Small-diameter nonmyelinated axons in the primate corpus callosum. *Archives of neurology*, 37(2):114, 1980. [25]
- [97] D.F. Tate, J.D. Conley, R.H. Paul, K. Coop, S. Zhang, W. Zhou, D.H. Laidlaw, L.E. Taylor, T. Flanigan, B. Navia, R. Cohen, and K. Tashima. Quantitative diffusion tensor imaging tractography metrics are associated with cognitive performance among HIV-infected patients. *Brain Imaging and Behavior*, 4:68–79, 2010. [5]
- [98] N. Toussaint, J.C. Souplet, and P. Fillard. MedINRIA: Medical image navigation and research tool by INRIA, <http://www-sop.inria.fr/asclepios/software/medinria>. [94, 95]
- [99] D.S. Tuch. Diffusion mri of complex tissue structure. *Science*, (1996), 2002. [8]
- [100] J. Van Waesberghe, W. Kamphorst, CJA De Groot, MAA Van Walderveen, JA Castelijns, R. Ravid, GJ Lycklama a Nijeholt, P. Van Der Valk, CH Polman, AJ Thompson, et al. Axonal loss in multiple sclerosis lesions: magnetic resonance imaging insights into substrates of disability. *Annals of neurology*, 46(5):747–754, 1999. [27]
- [101] A. Vilanova, Song Zhang, G. Kindlmann, and David H. Laidlaw. An introduction to visualization of diffusion tensor imaging and its applications. In *Visualization and Image Processing of Tensor Fields*. Springer-Verlag, 2005. In Press. [84, 93]
- [102] S. Wakana, H. Jiang, L.M. Nagae-Poetscher, P. van Zijl, and S. Mori. Fiber Tract-based Atlas of Human White Matter Anatomy1. *Radiology*, 230(1):77, 2004. [95, 98]
- [103] J. Wang and N. Zabaras. Using Bayesian statistics in the estimation of heat source in radiation. *Int. J. Heat Mass Transfer*, 48(1):15–29, 2005. [42]
- [104] SG Waxman. Determinants of conduction velocity in myelinated nerve fibers. *Muscle Nerve*, 3(2):141–50, 1980. [24]
- [105] C.F. Westin, SE Maier, H. Mamata, A. Nabavi, FA Jolesz, and R. Kikinis. Processing and visualization for diffusion tensor MRI. *Medical Image Analysis*, 6(2):93–108, 2002. [32]
- [106] H. Zhang and D. Alexander. Axon diameter mapping in the presence of orientation dispersion with diffusion MRI. *Medical Image Computing and Computer-Assisted Intervention–MICCAI*, pages 640–647, 2010. [33, 56]

- [107] H. Zhang, P.L. Hubbard, G.J.M. Parker, and D.C. Alexander. Axon diameter mapping in the presence of orientation dispersion with diffusion mri. *NeuroImage*, 2011. [61]
- [108] S. Zhang, C. Demiralp, and D.H. Laidlaw. Visualizing Diffusion Tensor MR Images Using Streamtubes and Streamsurfaces. *IEEE TVCG*, 9(4):454–462, 2003. [85, 88, 101]
- [109] W. Zhou, S. Correia, and D.H. Laidlaw. Evaluation of Design Features in Interactive 3D Tracts-of-interest Selection Tools in DTI. *Proceedings of IEEE Visualization Poster Compendium*, 2008. [5]
- [110] W. Zhou, S. Correia, and D.H. Laidlaw. Haptics-Assisted 3D Lasso Drawing for Tracts-of-interest Selection in DTI Visualization. *Proceedings of IEEE Visualization Poster Compendium*, 2008. [5]
- [111] W. Zhou, M.G. Hall, and D.H. Laidlaw. Inferring microstructural properties using angular double pulsed gradient spin echo NMR in orientationally unknown tissue. In *Computational Diffusion MRI Workshop at Medical Image Computing and Computer-Assisted Intervention–MICCAI*, 2010. [5, 34]
- [112] W. Zhou and D.H. Laidlaw. An analytical model of diffusion and exchange of water in white matter from diffusion-MRI and its application in measuring axon radii. *Intl Soc Magn Reson Med*, 17:263, 2009. [5, 62]
- [113] W. Zhou and D.H. Laidlaw. Inferring axon properties with double-PGSE MRI using analytical water diffusion model. *Intl Soc Magn Reson Med*, 18:677, 2010. [5, 34]
- [114] W. Zhou and D.H. Laidlaw. Measurement of axon radii distribution in orientationally unknown tissue using angular double-pulsed gradient spin echo (double-PGSE) NMR. *Intl Soc Magn Reson Med*, 19:3938, 2011. [5, 34]
- [115] W. Zhou, P.G. Sibley, S. Zhang, D.F. Tate, and D.H. Laidlaw. Perceptual coloring and 2D sketching for segmentation of neural pathways. In *ACM SIGGRAPH 2006 Research posters*, page 172. ACM, 2006. [5]